



저작자표시-비영리-변경금지 2.0 대한민국

이용자는 아래의 조건을 따르는 경우에 한하여 자유롭게

- 이 저작물을 복제, 배포, 전송, 전시, 공연 및 방송할 수 있습니다.

다음과 같은 조건을 따라야 합니다:



저작자표시. 귀하는 원저작자를 표시하여야 합니다.



비영리. 귀하는 이 저작물을 영리 목적으로 이용할 수 없습니다.



변경금지. 귀하는 이 저작물을 개작, 변형 또는 가공할 수 없습니다.

- 귀하는, 이 저작물의 재이용이나 배포의 경우, 이 저작물에 적용된 이용허락조건을 명확하게 나타내어야 합니다.
- 저작권자로부터 별도의 허가를 받으면 이러한 조건들은 적용되지 않습니다.

저작권법에 따른 이용자의 권리는 위의 내용에 의하여 영향을 받지 않습니다.

이것은 [이용허락규약\(Legal Code\)](#)을 이해하기 쉽게 요약한 것입니다.

[Disclaimer](#)

**공학박사학위논문**

**액상 내 질량 측정을 위한**

**마이크로 유리모세관 공진기의 개발**

**Development of Glass Micro-capillary Resonators  
for Mass Sensing Applications in Liquid**

**2018년 8월**

**서울대학교 대학원**

**기계항공공학부**

**이 동 혁**

액상 내 질량 측정을 위한  
마이크로 유리모세관 공진기의 개발

Development of Glass Micro-capillary Resonators  
for Mass Sensing Applications in Liquid

지도교수 고 상 근

이 논문을 공학박사학위논문으로 제출함

2018년 4월

서울대학교 대학원

기계항공공학부

이 동 혁

이동혁의 공학박사학위논문을 인준함

2018년 6월

위 원 장 \_\_\_\_\_ (인)

부위원장 \_\_\_\_\_ (인)

위 원 \_\_\_\_\_ (인)

위 원 \_\_\_\_\_ (인)

위 원 \_\_\_\_\_ (인)

# **Abstract**

## **Development of Glass Micro-capillary Resonators for Mass Sensing Applications in Liquid**

Donghyuk Lee

School of Mechanical & Aerospace Engineering

The Graduate School

Seoul National University

Micro mechanical resonator sensors and transducer systems are widely used for precisely measuring a mass of target analytes. Those sensors usually have a resonant-shift based operation and readout systems, which shows a great mass responsivity, enabling it to be used as a microscale inertial sensor for weighing micro/nano particles.

Hollow microtube resonators have become one of the most promising platforms for inertial sensing of liquids and particle suspensions with the hollow core intrinsically serving as sample delivery and transport channel. . The embedded channel can guide the liquid samples and suspended particles toward the mass sensing region as needed. In addition, it significantly reduces the viscous damping effect to achieve high quality factor and low frequency noise by confining the fluid inside the device inner channel, thus enables the hollow microtube resonators have an unprecedented mass sensitivity in the fluid environment.

Its capability for mass measurement of cells, gold/plastic particles ranging from tens of micrometers to sub-microscale in size had been demonstrated. However, microfabrication process for the device has been costly and time-consuming, limiting widespread adaptation of the technology.

In this dissertation, a novel fabrication technique for hollow microtube resonator assembly using a glass micro-capillary tube is employed to replace MEMS (Micro Electro Mechanical System)-based device to provide more rapid and facile dimension tunability while providing comparable sensitivity. The micro-capillary resonators were fabricated by a simple conventional laser pulling process. Micro-capillary resonators with diameter ranging from 10 to 200  $\mu\text{m}$  were fabricated from 1-mm diameter glass capillary. The cross-sectional dimension tunability envisions its potential to optimize the weight of the resonator to target samples of interest to maximize its mass sensitivity more rapidly and cost-effectively.

An elliptical micro-capillary resonator was used to divide two orthogonal vibration modes (mode-split) along major and minor axes to provide an additional tool to spatially analyze the change of the inertial term during measurements.

In this dissertation, the fabricated resonators have been measured the nanoliter fluid density, micro oil droplet, soda lime glass microparticles, and unicellular organism of *paramecium Aurelia* for demonstrating mass sensing applications.

**Keywords : Resonator, Micro capillary, Micro particle, Mass sensor**

**Student Number : 2012-30925**

# TABLE OF CONTENTS

Table of Contents .....	i
List of Figures .....	vi
List of Tables.....	xvii
Chapter 1. Introduction .....	1
1.1. Background .....	1
1.2. Literature review .....	2
Fabrication of hollow microtube resonators and SMR.....	2
Operation techniques of SMR.....	4
Micro-capillary platform and its fabrication .....	6
Introducing miniature frequency readout instruments .....	9
1.3. Engineering issues for widespread application of the mass sensing resonators .....	10
1.4. Dissertation goals.....	11
Migration from a wafer-based MEMS resonator to a micro-capillary...	11
Manufacturing a portable mass sensing platform.....	12
Analyzing characteristics of micro-capillary resonance behavior.....	12
Demonstrating the mass sensing applications of micro-capillary resonator .....	13

1.5. Dissertation overview.....	13
Chapter 2. Modeling of Micro-capillary resonator .....	15
2.1. Resonance motion .....	15
Comparison of the resonator type .....	17
Driven harmonic oscillation of micro-capillary resonator .....	21
Resonance frequency and effective parameter .....	22
2.2. Tensile force applied to the string type resonator .....	24
2.3. Effect of boundary condition of the bridge type resonator.....	25
2.4. Mode-split of the elliptical cross-section resonator .....	27
2.5. Axis rotation.....	28
Chapter 3. Mass responsivity .....	31
3.1. Resonance frequency shift .....	31
Particle mass effect.....	32
Particle inertia effect .....	35
Fluid density change.....	38
3.2. Mass responsivity.....	39
3.3. Dimension tuning for increase mass responsivity .....	40
3.4. Noise and limit of detection .....	41
Quality factor .....	42

Allan deviation .....	44
Limit of detection .....	44
Chapter 4. Operation principles .....	46
4.1. Operation scheme of string type micro-capillary resonator .....	47
Piezoelectric readout .....	47
Self-oscillation scheme .....	52
4.2. Operation scheme of bridge type micro-capillary resonator .....	55
Astigmatic detection system.....	55
Digital phase locked loop (PLL) .....	63
Loop bandwidth and particle speed.....	64
Chapter 5. Fabrication and assembly of micro-capillary resonator.....	66
5.1. Micro-capillary fabrication techniques .....	66
5.2. Analytical modeling of taper shape of capillary .....	68
5.3. Custom-made capillary pulling machine.....	71
5.4. Fabrication results .....	77
Micro-capillary fabricated by commercial puller.....	77
Micro-capillary fabricated by custom-made puller .....	78
Wall thickness tuning.....	80
5.5. Resonator assembly.....	83

String type micro-capillary resonator with QTF .....	83
Bridge type micro-capillary resonator with OPU.....	85
Chapter 6. Experimental setup .....	89
6.1. Fluidic control system .....	89
6.2. Readout and oscillator system implementation.....	92
System 1: QTF and self-oscillation circuit.....	92
System 2: OPU and FPGA PLL device.....	96
6.3. Notice .....	102
Chapter 7. Device characterization .....	103
7.1. Piezoelectric readout validation .....	103
7.2. Mode-split resonance motion detection .....	108
7.3. Effects of fabrication parameters .....	112
Resonance frequencies and quality factors .....	112
Applied tension effect on string type resonator.....	114
Boundary clamping effect on bridge type resonator .....	115
Asymmetry factor of micro-capillary.....	117
7.4. Frequency stability .....	119
Chapter 8. Mass sensing applications .....	122
8.1. Liquid density measurement .....	122

8.2. Quality monitoring of production of micro oil droplets.....	125
8.3. Mass sensing of glass microparticles and unicellular organism.....	130
Chapter 9. Conclusion.....	140
REFERENCES.....	143
Appendix.....	152
A.1. Automatic power control and voice coil actuator.....	152
A.2. Particle frequency peak finding and fitting.....	154

# LIST OF FIGURES

Figure 2.1 (a) Resonance mode shape of a micro-capillary resonator and (b) nomenclature of the cross-section. ....	16
Figure 2.2 Schematics of the normalized bending motion of cantilever, bridge and string type at the first resonance. ....	18
Figure 2.3 Rotation of the resonator with azimuthal angle $\alpha$ with respect to y-axis. The external force $F(t)$ applied to the resonator is beneath the resonator. ....	29
Figure 3.1 The illustration of point mass of particles passing through the resonator. ....	32
Figure 3.2 The illustration of particle placed at the cross-section of resonator when particles center position has offset $(\mathbf{e}_x, \mathbf{e}_y)$ . ....	36
Figure 3.3 The mass responsivity variation by tuning the micro-capillary resonator dimension and liquid density. If particle placed inside the middle of the resonator, various frequency shifts of the resonator by adjusting (a) inner and outer cross-section diameter ratio, (b) outer diameter, (c) length, and (d) density of fluid is plotted. With assumption that the density of micro-capillary and the particle are 2.23 and 2.46 g/ml, respectively. ....	41
Figure 4.1 (a) A QTF before and after the package is removed. Scale bar is 1 mm. (b) The illustration of vertical force applied to the end of cantilever of QTF and the electric field generated inside the QTF material. ....	47

Figure 4.2 Comparison the electrical configurations of QTF and its resonance responses as a filter and an external force sensor.....	48
Figure 4.3 (a) Schematic of actuation and detection of vibration of the micro-capillary resonator and (b) its electrical transduction. ....	50
Figure 4.4 Block diagram of self-oscillation system.....	53
Figure 4.5 Astigmatic detection system of OPU. (a) Optical setup of OPU. (b) The relation of FES (focusing error signal) output and the object displacement. ....	57
Figure 4.6 Illustration of motion of mode-split in the elliptical cross-section resonator and incident laser spot position on the capillary surface. The two-resonance motion occurred along the major and minor axes, resulting that the vertical amplitudes of laser spot at the $\boldsymbol{x}l$ position of the two-resonance motion showed different.....	59
Figure 4.7 Frequency response simulation of the mode-split resonator by measuring the astigmatic detection system. The lateral position of the incident laser spot is set to zero, and assuming the minor and major resonances have the resonance frequency of 68 and 70 kHz, respectively. the quality factor of the two resonator has 100.....	61
Figure 4.8 Various frequency responses simulation of the mode-split resonator by adjusting (a) the azimuth angle $\boldsymbol{\alpha}$ and (b) the dimensionless parameter $\boldsymbol{\beta}$ . The assumption of micro-capillary resonator is same as that in Figure 4.7...	62

Figure 4.9 Frequency response simulation plots for 9 combinations of azimuth angle and dimensionless lateral position of laser spot. The assumption of micro-capillary resonator is same as that in Figure 4.7. .... 62

Figure 4.10 (a) Simulation of frequency shift when a single particle passes through the bridge and cantilever type resonator. Analyzing the modulated frequency by (b) FFT and (c) cumulative power spectral density. The mass of particle is set to 0.1 % of the resonator and the transit time of particle passing through the length of the resonator is set to 100 ms..... 65

Figure 5.1 Material properties of glass in function of the temperature. When the temperature of the glass is in glass-transition state which is between solid state and liquid state, the material properties of the glass turns into the viscoelastic property. .... 67

Figure 5.2 The structure of a fiber taper and nomenclature. .... 69

Figure 5.3 A custom-made capillary pulling machine. (a) Illustration of the fabrication process. (b) A cyclic power of CO<sub>2</sub> laser irradiates to the capillary surface while the capillary is in the rotation to form an un-uniform temperature distribution in the cross-section of the capillary. A detail view of (c) capillary setup and (d) photograph of manufactured device. (e) GUI software to control the overall fabrication process..... 72

Figure 5.4 Heat transfer modeling of glass capillary ..... 73

Figure 5.5 Simulation results of temperature of glass capillary as a function of heating time. With the assumption of that the laser beam diameter is 2.5 mm, radius of the capillary is 0.5 mm, heat zone length is 2 mm. .... 75

Figure 5.6 Simulation of cooling time estimation of heated glass capillary. The capillary in the tapered region (a) shows different cooling times (b) depending on the size of the diameter..... 76

Figure 5.7 A picture of borosilicate glass capillary (i). Schematic showing the capillary pulling to decrease the inner and outer diameters around the middle section of the capillary (ii). A pulled capillary (iii). Scanning electron microscope images of cross-section areas of pulled capillaries with various inner and outer diameters. Scale bars are 100, 10, 10, and 10  $\mu\text{m}$ , respectively (iv)..... 78

Figure 5.8(a) Photographs of pulled micro-capillary and (b) plot of their outer diameter at the middle. (c) Laser power variation with respect to the rotational angle. (d) Several photographs of elliptical cross-section of pulled micro-capillary ((i) Perfectly symmetric, asymmetric ratio ( **$D_{\text{minor}}/D_{\text{major}}$** ) of (ii) 0.97 and (iii) 0.93). Scale bars are 100  $\mu\text{m}$ . (e) Asymmetric ratios of pulled micro-capillaries as a function of rotational laser power ratio of low power of P2 divided by high power P1. .... 79

Figure 5.9 (a) Selective etching process of the micro-capillary. (b) Scanning electron micrographs of micro-capillaries before and after the selective etching. All scale bars are 50  $\mu\text{m}$ ..... 81

Figure 5.10 (a) Scanning electron micrographs of micro-capillaries with various inner pressure applied during the pulling process, and (b) the plot of the inner and outer diameter of the fabricated micro-capillaries..... 82

Figure 5.11 (a) Assembly process of string type micro-capillary resonator with piezoelectric readout system. (b) Photographs of an assembled resonator system. .... 84

Figure 5.12 Fabrication process of bridge type micro-capillary resonator block. (a) Laser heating and pulling process to form a microscale capillary (1 and 2). A razor blade cuts the micro-capillary section to make micro-pipette capillary (3). A 4-mm trench of aluminum block is bonded to the micro-pipette capillary and the pair of aluminum block is covering on it (4). Gold is coated on the capillary surface by general sputter machine (5). A thin (0.1 mm) glass is covered the resonator to prevent external scratch and air perturbation to the resonator (6). (b) Photographs of the actual products at the manufacturing process 3 and 6. .... 86

Figure 5.13 (a) Assembly view of bridge type micro-capillary resonator with OPU readout system and (b) its assembled picture. .... 87

Figure 5.14 Beveling micro-capillary tip. (i) A sharp edge at the tip of the micro-capillary is beveled by rotating sandpaper with 30 seconds with 600 rpm. After beveling, (ii) glass chips stick to the capillary surface and (iii) the tip is cleaned after ultrasonication. .... 88

Figure 6.1 Photographs of fitting of a FEP tube to the capillary by using (a) commercial tubing connector and (b) silicon tube. .... 90

Figure 6.2 Two types of fluidic setup to deliver liquid sample into the resonator by using (a) the pressurizable vial with pressure controller and (b) syringe controller. .... 90

Figure 6.3 Photograph of custom-made syringe controller using step motor and microcontroller. And the GUI software to control the syringe. ....	91
Figure 6.4 Open and closed loop drive circuits for the micro-capillary resonator system.....	93
Figure 6.5 (a) Printed circuit board of transimpedance amplifier and (b) its electrical schematic. ....	93
Figure 6.6 (a) Diagram of driver unit of micro-capillary resonator and frequency measurement system and (b) its printed circuit board.....	95
Figure 6.7 Electrical circuit of signal processing unit of OPU system. ....	97
Figure 6.8 Voice coil actuators built in OPU to move the astigmatic lens along the vertical $z$ and lateral $x$ directions. And picture of integrated OPU controller. ....	97
Figure 6.9 PLL functionalized FPGA board. ....	99
Figure 6.10 Experimental setup of micro-capillary resonator with OPU readout system.....	100
Figure 6.11 (a) Schematic of OPU-resonator system with inverted microscope and (b) its picture. ....	101
Figure 7.1 Signal transfers in the micro-capillary resonator with QTF readout system and its resonance spectra by optical-lever and piezoelectric readouts. (a) Experimental schematic for optical-lever readout of resonator with partial gold coating. (b) Block diagram for the resonator. (c) Amplitude and phase spectra	

of individual components and combined resonator system obtained by optical-lever and piezoelectric readouts. ....	104
Figure 7.2 Amplitude and phase spectra of a water-filled micro-capillary resonator measured by optical-lever and piezoelectric readouts. While the resonance peak for the micro-capillary resonator around 24.5 kHz is universally detected, the QTF resonance around 33 kHz is exclusively measured by the piezoelectric readout. ....	105
Figure 7.3 Amplitude measurement of the micro-capillary resonator. (a) Schematic for atomic force microscope cantilever-based measurement of local vibration amplitude of the micro-capillary. (b) Amplitude spectra acquired at the mid-point ( $x = 3$ mm) of the micro-capillary. (c) Current versus amplitude and noise floor of the piezoelectric readout. (d) Local amplitudes of the micro-capillary measured at several lateral positions and their sinusoidal fits with various actuation voltages. (e) Amplitudes at the piezo actuation node ( $x = 0$ mm) and the mid-point ( $x = 3$ mm) of the micro-capillary and their ratios as a function of the actuation voltage. ....	107
Figure 7.4 (a) Measurement of the S-curve on a surface of micro-capillary. (b) Acquiring the contour of micro-capillary by hopping scanning mode using voice coil actuators in OPU. ....	109
Figure 7.5 (a) Examine the resonance amplitude using astigmatic detection system along the surface of micro-capillary and (b) frequency sweep results exhibit the distinguished major and minor axes resonance motion of micro-capillary resonator. ....	110

Figure 7.6 The frequency response of the mode-split micro-capillary resonator when anti-resonance peak occurred. .... 111

Figure 7.7 (a) Scanning electron micrograph of cross-section area of micro-capillary used for a string type resonator. (b) Resonance frequency as a function of length of the micro-capillary resonator filled with water. Resonant characteristic of fabricated micro-capillary resonator about (c) amplitude spectra and (d) quality factors of which lengths range from 4 to 10 mm. .... 113

Figure 7.8 (a) Resonant characteristics of fabricated bridge type micro-capillary resonators about resonance frequency and quality factor. (b) resonance frequencies of fabricated bridge and string type micro-capillary resonators plotted together..... 114

Figure 7.9 Effect of the applied tension on the amplitude and resonance frequency signal coupling. (a) Schematic showing how to apply the axial tension before the permanent fixation with epoxy bond. (b) Frequency response plot and (c) resonance frequency and amplitude at resonance as a function of the axial tension..... 115

Figure 7.10 (a) Illustration of three-types of boundary fixation of bridge type resonator. (b) Resonance frequencies plot of the bridge type resonator with different boundary conditions. The dashed lines represent theoretically estimated resonance frequency with respect to the resonator length and its color corresponds the boundary configuration of experimental data. .... 116

Figure 7.11 Three experimental results of frequency spectra of micro-capillary resonators. Each resonator has different asymmetric factor..... 118

Figure 7.12 Frequency stability of the string and bridge type resonators and their Allan deviation plot. The bridged type resonator has mode-split resonance; thus the two resonance frequencies are plotted together..... 121

Figure 8.1 Resonant spectra of the (a) string and (b) bridge type micro-capillary resonators filled with various liquid samples. Resonance frequency shift of the (c) string and (d) bridge type resonators measured while water, ethanol-water mixtures, and glycerol-water mixtures are sequentially introduced. The bridge type resonator has mode-split, thus the shift plot of the two resonances are plotted together..... 123

Figure 8.2 Normalized density responsivity of the string and bridge type micro-capillary resonators in comparison with those of other micro fabricated density sensors found from literatures plotted as a function of area ratio (density of wall,  $\rho_{wall}$ , is set to be 2.25 g/cm<sup>3</sup>). The dashed line shows the theoretically estimated responsivity..... 124

Figure 8.3 A micro droplet generator configured at the inlet of the micro-capillary resonator for real-time monitoring of droplet mass. The inset figures 1, 2, 3, and 4 show snapshots at each section..... 126

Figure 8.4 (a) Resonance frequency shifts fitting upon a transit of mineral oil plugs of which equivalent radii are 25.4, 28.5 and 31.5  $\mu\text{m}$ , respectively. (b) Histogram for the equivalent radius of oil droplets (cumulative counts are 310). ..... 127

Figure 8.5 (a) The illustration of oil droplet shows the 31 nm radius resolution of the micro-capillary resonator when the radius of droplet is set to 28.47  $\mu\text{m}$ .

(b) Detection resolution of the difference in mineral oil droplet radius as a function of the equivalent oil droplet radius (calculated from frequency stabilities, 1 and 3  $\sigma_A$  of string type resonator showed in the Figure 7.12). The limit of detection (LOD) for the smallest droplet radius is 4.25  $\mu\text{m}$ . ..... 129

Figure 8.6 Sample particles and unicellular organism. Microscope image of (a) soda-lime glass microparticles of four different diameters and (b) *Paramecium Aurelia*. All scale bars are 100  $\mu\text{m}$ . (c) Target particles placed on the slide glass for experiment preparation. .... 131

Figure 8.7 Two frequency shift cases of 76.39  $\mu\text{m}$  diameter soda-lime glass microparticle passes through the mode-split micro-capillary resonator. In the case 1, the normalized two resonant shifts along the major and minor axes resonance almost have a similar response. On the other hand, in the case 2, the error of normalized resonant shifts is evidently observed which is estimated by the perturbation of the particle in the resonator. In case 2, maximum buoyant mass error calculated from the two-resonance motions of the resonator showed 80 ng (the total buoyant mass of particle is estimated to 368 ng) where the normalized particle position range from 0.3 to 0.7 in the resonator..... 132

Figure 8.8 Histogram plot of buoyant mass of different four diameters of soda-lime glass microparticles measured by (a) minor and (b) major axes resonances of mode-split micro-capillary resonator. Each colored area represents the buoyant mass of the particles calculated from the diameter range provided by the manufacturer. Cumulative counts of each monodisperse particles are 277, 311, 309, and 324 from the smallest diameter to the largest diameter, respectively. .... 134

Figure 8.9 Center position offset of particles when passing through the resonator cross-section. (a) Measured particles image. (b) Illustration of particle positioning in the resonator's inner channel. The red dash circles represent the area where the particle center can pose. (c) Relative position offset of measured particle samples of particles. Blue dash dot lines represent the maximum distance that particle offset can be located. (d) Histograms of relative position offset of measured particles..... 136

Figure 8.10 Histogram plot of buoyant mass of *Paramecium Aurelia* measured by the major and minor axes resonances of mode-split micro-capillary resonator. Cumulative counts are 199..... 137

# LIST OF TABLES

Table 2.1 Normalized mode shape functions and the boundary conditions of the three cases of the resonator type. ....	19
Table 2.2 Comparison of the resonator types.....	20
Table 2.3 Boundary conditions of bridge type resonator and its resonance frequencies .....	26
Table 4.1 The analogy of electrical and mechanical model of Butterworth Van-Dyke circuit.....	49
Table 6.1 Specifications of the OPU controller .....	98
Table 8.1 Summarized the mean and deviation results of weighed glass microparticles and unicellular organism. ....	139

# CHAPTER 1.

## INTRODUCTION

### 1.1. Background

Microscale mechanical resonator has been used as a physical transducer to understand the micro/nano environment. The micromechanical sensors have been developing since 1990s [1], measuring various physical characteristics in microscale such as weak force [2], temperature [3], interaction of molecule [4], [5], etc.

The mass, one of the fundamental physical properties of the material, can be measured by analyzing the output response of the resonator. For example, when a target of interest is attached to a resonator, the resonant frequency shifts proportional to the target mass and can be quantitatively analyzed using a frequency modulation readout technique. Owing to advances in microfabrication technology and frequency-based operation technique, the micromechanical resonator can achieve a superior mass sensitivity reaching down to zeptogram [6] to yoctogram [7] range. A number of microfabricated mechanical resonators have demonstrated their mass sensitivity in microscale applications [8]–[11].

Such microscale mass sensors have got much attention, especially in the field of biology since most of biomolecules to be measured are in micro to nanoscale range [8], [12]. However, real-time monitoring of living biomolecular mass through the resonator immersed in fluid is limited since the increasing viscous

drag by surrounding liquid degrades the resonance quality, consequentially yielding the low mass resolution [13], [14].

Suspended microchannel resonator (SMR) is introduced in the 2000s to solve the low grade of resonance quality of the resonator in the fluid [14]–[16]. SMR is designed to have an inner fluidic channel which allows biomolecules and fluid to flow inside, while the exterior of the resonator is exposed *in vacuo*. Using this configuration, SMR vibrates in a low viscous environment that preserves the energy dissipation during its resonance motion, thereby enhancing frequency stability, which enables the mass resolution of SMR to elevate significantly even with fluid analytes inside the resonator. Therefore, SMR has proven to be the best device in terms of high-resolution mass sensing in liquid, demonstrating its measurement capability for living cells [14], [17]–[21], density [18], [22], [23], volume [19], surface charge [24], and deformability of cell [25], [26], label-free biomarker [27], [28] measurements. Several hollow microtube resonators of which their topology is similar to that of SMR also exhibits their capability of high-resolution mass sensing [29]–[31], showing higher quality factor than other micromechanical resonators immersed in liquid.

## **1.2. Literature review**

### **Fabrication of hollow microtube resonators and SMR**

Although the specific fabrication processes of each hollow microtube resonators are different, there are common requirement steps to form an inner

fluidic channel. Though typical silicon microfabrication for realizing a general cantilever resonators consists of three steps; wafer preparation, cantilever shape patterning, and release the cantilever [1], however, for fabricating the inner channel of the resonator to make a fluidic resonator an additional process is required. For example, Enoksson *et al.* [32] proposed the pair of resonator patterning at the two silicon wafer surfaces and fusion bonding of the two wafers to form interior tube channel. After wafer bonding, the wafer pair is etched through the both top and bottom side forming the exterior of the resonator. Khan *et al.* [30], [33] fabricated SMR by depositing two structure layer on the Si wafer, with the sacrificial layer inserted in the middle of them. Then the sacrificial layer is removed by wet etching and the structure layer released from the substrate to make hollow microtube cantilever. A plate shape bulk resonator which has inner fluidic channel is introduced by Agache [13]. The two SOI (silicon on insulator) wafers are bonded after photolithographic process and RIE (reactive ion etching) to make the embedded channel. The top wafer is grinded until the plate resonator is exposed, and the capping pyrex wafer is bonded upper side of the resonator. Besides, embedded nanochannel resonator fabricated by CMOS (Complementary metal–oxide–semiconductor) technology [34] and polymeric resonator [35] are also exhibited.

The fabrication process of SMR [14], [15] is similar to the wafer bonding of silicon to silicon and silicon to pyrex described in Enoksson *et al.*[32]. However, the SMR fabrication process is more complicated since the process includes depositing silicon nitride on the polysilicon sacrificial layer to make embedded channel [15].

All the aforementioned wafer-based hollow microtube resonators are fabricated by 2D surface micromachining, therefore the additional wafer bonding or sacrificial etching to form an inner hollow structure is inevitable. Furthermore, a fluidic access hole should be additionally fabricated to interconnect the inner channel of the resonator to outside fluidic tubing. Those of added fabrication requirements compared than the conventional fabrication process of Micro ElectroMechanical System (MEMS) resonators make the hollow microtube resonator manufacturing complex and difficult to follow, which hinders widespread usage. A novel approach by atomic migration of silicon recently reported has significantly simplified and expedited the overall fabrication of hollow resonators [36], Nevertheless, researchers who have no or limited access to standard microfabrication facilities housed in a cleanroom hardly take advantage of the simple process.

### **Operation techniques of SMR**

Operation techniques for oscillating the SMR and measuring its resonance frequency in real-time have been developed by Manalis group. For oscillating the SMR device, there is at least four components is necessary; physical actuator, frequency readout instrument, oscillator, and frequency recording system. A physical actuator for vibrating the resonator is mainly a piezocrystal actuator [37] or electrostatic force driver [14]. Both actuator components convert an electrical signal to physical force, and if the driving force is insufficient, a current buffer amplifier can be employed for supplying the auxiliary power. An optical-lever system is commonly used for frequency

readout instrument of the SMR, which incidents the laser beam to the resonator surface and reads the reflected laser that is corresponding the resonator motion via 2-cell photodiode. A transimpedance amplifier convert the electrical current signal originated from the 2-cell photodiode to the electrical voltage and transferred it to the oscillator system.

A simple implementation of oscillator system which is the analog circuit consist of the gain amplifier and phase shifter is employed at the early of SMR development [14]–[16]. The resonance frequency recording system is implemented by a frequency heterodyne down-mixer at 1 kHz and the mix-downed resonant signal is counted by a digital frequency counter and recorded in PC (personal computer), those are the basic working principles for SMR experiment [38].

For minimizing the uncertainty of mass of analytes passing through the SMR, a second flexural vibration mode of the SMR is operated, resulting the improvement of particle mass resolution in some experiment cases [39]. Adopting the advance of digital signal processing technology, a digital phase locked loop (PLL) by the field programmable gate array (FPGA) hardware logic device have developed to replace the analog oscillator circuit, and to achieve attogram mass resolution using suspended nanochannel resonator (SNR) [40].

In recent years, the driving of SMR using digital PLL has been further developed in view of the multiple mode [41]. Thanks to the flexible ability to adjust oscillation parameters and the number of oscillators using the digital system, the SMR is operated in four eigenmodes simultaneously to resolve the

nanoscale mass distribution in the resonator. Recently, the multiple-mode oscillating capability of FPGA-PLL is applied to driving twelve SMRs simultaneously for monitoring single-cell growth [42]. Such multiple mode operation techniques expected to be continuously studied since it provides increasing throughput for weighing a particle and it is useful in multimode resonance researches.

### **Micro-capillary platform and its fabrication**

Micro-capillary refers to a glass fiber, the material of which is borosilicate has an inner vacant hole. Micro-capillaries can be classified as hollow fibers and are classified as micro structured capillaries depending on the number and the shape of internal holes. Micro-capillary is usually formed to micro-pipette shapes for cell handling tool [43] that shapes provide an ease accessibility to the intracellular or extracellular of cells. Development of Lab On Fiber (LOF) technologies enables the micro-capillary to be not only a handling tool but also optical sensor [44]–[46], electrophoresis platform [47]–[49], and a biological sensing platform [50] *in vivo* and *in vitro*.

The advantage of easily longitudinal stretching the micro-capillary as long as desired makes multi-site sensing region and it allows to facilitate an integrated sensor platform for multifunctional device in a single capillary [50]. Micro-capillary requires small analyte volume compared than several quartz crystal microbalance [51] which the whole device immersed in the sample fluid and provides an easier access to microfluid via inner channel. Many potentialities

are feasible in micro-capillary platform using its inner channel for containing fluid analyte.

Lab on Fiber sensors are categorized in three, depending on sensing region; Lab On Tip (LOT), Lab Around Fiber (LAF), and Lab In Fiber (LIF). Among them, the fluidic topology of LIF is exactly equal to that of SMR. Therefore, it is natural to implement SMR's operating principle to the micro-capillary platform if the micro-capillary is configured to be a bridge or string type mechanical resonant structure. Additionally, the SMR-functionalized micro-capillary also can provide a LOT application, for example, a patch clamp for cell voltage activity recorder [52]–[54] or cell sorter [55]–[58], if one end is cut to form a tip.

This potential versatile micro-capillary platform is extremely easy to manufacture compared than conventional hollow microtube resonator or SMR fabrication processes. The fabrication process of micro-capillary simply consists of two steps; heating and pulling. Heating a certain length of millimeter size of glass capillary by a heater and pulling the heated capillary on both sides make a micro-capillary with an inner channel. This low-cost fabrication does not require any microfabrication facilities nor a toxic chemical process, thus it is a fascinating candidate to replace the conventional MEMS process.

Understanding the glass micro-capillary manufacturing method can be possible by adopting the manufacturing method of a glass optical fiber, which has without an inner hole. Fabrication analysis about the glass optical fiber is well established in the optics research field because their main purpose is to

downsize the fiber to micron size for making the light wave transmitted in the fiber more sensitive to the interest physical changes.

The analytical approach to achieve the shape of pulled fiber is conducted since in the 1990s [59]. Timothy [60] predicted fiber shape using only the mass conservation principle during the process, excluding the fluid mechanic principles that is affected by material property related to the heat temperature. Timothy model is only applicable to the assumption that the ideal adiabatic condition during the entire pulling process and that the temperature is uniformly distributed in the fiber, although it allows us to envision a practical rough approximation of fiber shape.

A mathematical model of the shape of micro-capillary is proposed by Xue [61], [62] with considering a fluid mechanics. Xue model developed the capillary shape of generalized Newtonian material and applying the effect of surface tension during the process. However, a complete theory that explains the pulling process of micro-capillary or optical fiber is yet developed [61], most studies are based on experimental data [63]–[66] and numerical analysis [65], [67]–[71].

A number of pulling devices and fabrication technologies are presented [72]–[77]. Among them, heating the glass fiber using a carbon dioxide laser and constant speed pulling strategy facilitate theoretical modeling and feasible practical setup.

## **Introducing miniature frequency readout instruments**

An optical-lever instrument for measuring resonance motion of the SMR or other resonators is bulky so that the portable application like biopsy, *in vitro* experiment with microscope is hard to apply. To avoid bulky optical instrument setup, placing a piezoresistive layer inside the SMR to perform a frequency readout sensor is introduced [38]. However, the implementation of a piezoresistive sensor to SMR requires additional MEMS fabrication process and affects a thermal drift to the resonance motion due to its electrical resistance. For this reason, a realization of it is still challenging and has not yet been standardized.

A piezoelectric force transducer of quartz tuning fork (QTF) and a commercial optical pickup unit (OPU) seem possible candidate to replace a conventional optical readout system. Both sensors have a miniature size and already be an industrial mass product which provides a reliable sensitivity and a low cost. Adopting QTF and OPU sensors to SMR platform is beneficial to miniaturization of overall resonator platform.

The QTF, the shape of which shows two pair of cantilever connected at one end for configuring a tuning fork has an excellent quality factor, thus it has become a stable and precise clock source to use a frequency oscillator [78]. The cantilever length is typically ~5 mm, due to its small dimension it is even used clock source in wrist watch. The QTF can also be used as a nanoscale force detector, as the piezoelectric properties of QTF can convert physical perturbation of cantilever to electrical charge. The force detecting ability of QTF makes it to the atomic force microscopy (AFM) and scanning force

microscopy as a sensing probe [79]–[83] and shows a number of force sensor applications [84]–[88]. As the mechanical characteristic of QTF cantilever is regarded to second order mass-spring system, it is possible to use vibration sensor if the frequency to be measured is below the resonance frequency of the QTF. To further, if the cantilever of QTF contacts to the resonator without interfering with resonant motion and once the force transfer relationship between the resonator and the QTF is established, finally the QTF can act as a frequency readout sensor of the resonators.

OPU is used in commercial digital versatile disk (DVD) player as a displacement sensor measuring a pit height on the disk to read the recorded digital information. Despite the small size and low cost of the OPU, it exhibits a displacement resolution of up to nanometer, which is suitable for detecting deflection of microcantilevers. A number of researchers tried to implement the OPU to the applications of AFM [89]–[93] and resonance detecting sensors [94]–[97], have verified that it is valuable as a precise displacement sensor in a scientific instrument. The displacement measurement scheme of OPU is a non-contact strategy, therefore, the OPU can directly replace the conventional optical-lever setup to measure the resonance motion of resonators.

### **1.3. Engineering issues for widespread application of the mass sensing resonators**

The hollow microtube resonators or SMR have shown unprecedented inertial sensing performance of liquids and particles, however, slow and complicated

cleanroom fabrication process retards device development and hampers spreading to other research groups. Besides, bulky instrument setup of resonator platform hinders portable applications, limiting its usage to be confined to a few research groups. Practical engineering solution is necessary for widespread usage of the resonator in the field of bioengineering, oil industry, pharmaceutical, agriculture, point-of-care, and gaseous detection, etc.

#### **1.4. Dissertation goals**

The operation and mass sensing principle of a conventional silicon-based MEMS mechanical resonator can be replicated using the micro-capillary resonator platform. In this dissertation, Migration of the MEMS-based resonator platform to that of micro-capillary is studied to replace slow and complex process of MEMS fabrication technique, thus providing a more facile and rapidly producible microscale mass sensor with comparable mass sensitivity. Four main topics covered in this dissertation are as follows.

##### **Migration from a wafer-based MEMS resonator to a micro-capillary**

For multiscale, simple, and rapid fabrication of hollow microtube resonators, an alternative fabrication process by micro-capillary formation is suggested. This simple two-step technique (laser heating and pulling) to form a micro-capillary offers flexible dimensional tunability, reduced manufacturing time (<5 seconds) with an entire process conducted without cleanroom facilities, these advantages excel the conventional slow and complex process of wafer-

based microfabrication, making it a promising candidate to produce hollow microtube resonators. This dissertation describes a laser pulling fabrication process to form a micro-capillary and the assembly process of the micro-capillary, boundary clamp, support structure to integrate them to a resonator platform. The resonance frequency change of the resonator during the assembly process are also analyzed.

### **Manufacturing a portable mass sensing platform**

To employ a mass sensing resonator platform to the portable application, it is necessary to replace the bulky instrument. In general, the bulkiest equipment of the MEMS resonator platform is the optical-lever readout setup. In this dissertation, a portable mass sensing platform was realized through the two instruments, the one is a micro-capillary resonator integrated with the compact size of the piezoelectric force transducer, and the other is a commercial handheld optical readout instrument. The two readout schemes for detecting the vibrational motion of the micro-capillary are tested and validated.

### **Analyzing characteristics of micro-capillary resonance behavior**

Unlike MEMS-based resonators similar to a diving board shape, a micro-capillary has a circular cross-section with same width and thickness. If the micro-capillary's cross-section is formed to be slightly oval, its resonance behavior breaks down to two orthogonal resonance motions, called mode-split [98]. The geometrical shape difference along the major and minor axes at the

cross-section of the resonator changes effective stiffness; therefore, the resonance frequency of the resonator is divided into two separate frequencies. For an asymmetric cross-sectional micro-capillary, resonant frequency separation due to mode-splitting has a significant impact on frequency-based mass measurement applications. In this dissertation, this mode-split micro-capillary resonance phenomena is analyzed and demonstrated.

### **Demonstrating the mass sensing applications of micro-capillary resonator**

Using the proposed micro-capillary mass sensing resonator, several mass-sensing applications are demonstrated. Density measurement of fluid and buoyant mass of particles is presented as for mass spectroscopy application of the micro-capillary resonator platform. Size calibration of oil droplets based on mass measurement principle is also presented. Effect of dimension tunability on resonator performance is also examined for improvement of mass sensing performance of the resonator.

## **1.5. Dissertation overview**

This dissertation consists of three main categories. The first category includes a theoretical analysis of micro-capillary resonator behavior. In Chapter 2, a general formula for mass spectrometer of a MEMS resonator is applied to a micro-capillary resonator and mathematical modeling for mode-split phenomena of the elliptical-shaped resonators is presented. In Chapter 3, mass responsivity of the micro-capillary resonator is derived by its volumetric size

and further improvement for the responsivity is sought through dimension tunability. Source of frequency noise and limit of detection of the resonator are also presented.

The second category is about manufacturing of the micro-capillary resonator and its operating principles. Chapter 4 presents two operation schemes; one based on analog circuit feedback loop with piezoelectric contact vibration transducer and the other based on digital phase locked loop with astigmatic laser motion detector are presented. Chapter 5 discusses fabrication of the micro-capillary by laser heating and pulling of the original glass capillary, and assembly process of the micro-capillary resonator platform.

The third category relates to the characterization and demonstration of the fabricated micro-capillary resonator devices. Chapter 6 describes an experimental setup for fluidic and electronic circuit configuration. Verification of the readout scheme and the characterization of the fabricated resonators are carried out in Chapter 7. Finally, chapter 8 demonstrates the several applications of micro-capillary resonators as a microfluidic densitometer, a production quality monitoring device for micro oil droplets, and a mass spectroscopy for several microparticles.

# **CHAPTER 2.**

## **MODELING OF MICRO-CAPILLARY RESONATOR**

To understand the mechanical resonance of the resonator systems is to define the energy exchange between the potential and kinetic energy while the resonator system is in motion. Classical Euler-Bernoulli beam theory of the linear elastic material has been adopted to analyze the relative frequency shift due to added mass or inertial perturbation as a theoretical background.

In this chapter, a beam modeling to analyze the hollow micro-capillary resonators which have fluidic channel inside is studied. The characteristics including geometrical shape, boundary effect, resonant shift, mode-split phenomenon, and the derived formula when the resonance axis rotated with respect to the global coordinate are thoroughly studied.

### **2.1. Resonance motion**

To understand the resonance motion of the micro-capillary resonator, linear elastic small deflection of Euler- Bernoulli beam theory is adopted. According to the beam theory, when the beam is slender, neglecting rotational inertia and shear stress, the equation of motion is given by [99]

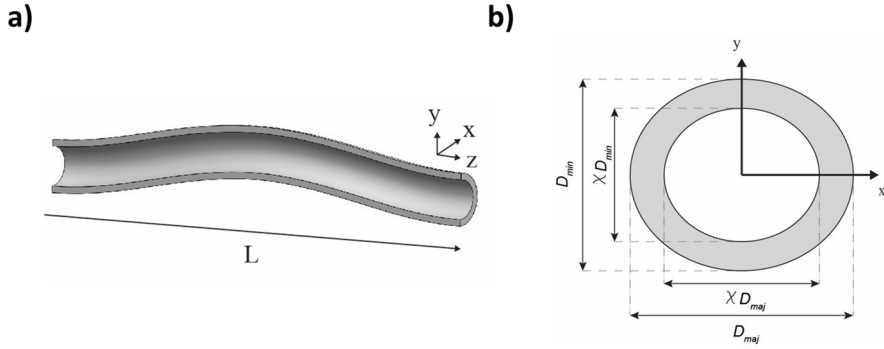


**Figure 2.1 (a) Resonance mode shape of a micro-capillary resonator and (b) nomenclature of the cross-section.**

$$\rho A \frac{\partial^2 u(z, t)}{\partial t^2} + EI_x \frac{\partial^4 u(z, t)}{\partial z^4} = 0 \quad (2.1)$$

where  $\rho$  is the mass density of the beam,  $A$  is the cross-sectional area,  $u$  is the deflection amplitude along the vertical direction (See Figure 2.1(a) of  $y$ -axis),  $z$  is the lateral location along the longitudinal direction of the beam,  $t$  is time,  $E$  is Young's modulus of the beam material and  $I_x$  is the area moment of inertia along the  $x$ -axis. This differential equation is resolved by a separation of variables form of time dependent function of  $f(t)$  and position dependent function of  $U(z)$

$$u(z, t) = \sum_{n=1}^{\infty} U_n(z) \cos(\omega_n t) \quad (2.2)$$

where  $n$  is the modal number and  $\omega$  is the frequency of the beam motion. Applying the equation (2.2) into (2.1) and solving the differential equation, the function  $U_n(z)$  can be written in the form

$$U_n(z) = U_{0,n}\phi_n(z) \quad (2.3)$$

$$\phi_n(z) = a_n \cos(\beta_n z) + b_n \sin(\beta_n z) + c_n \cosh(\beta_n z) + d_n \sinh(\beta_n z) \quad (2.4)$$

where the  $U_o$  is the amplitude of motion,  $\phi$  is the normalized mode shape function and  $\beta$  is the wavenumber of the beam motion. In the normalized mode shape function, the two trigonometric terms represent the mode shape of the beam and the following two hyperbolic terms represent the effect of the boundary condition.

The micro-capillary resonator can be fabricated into three resonator types; the cantilever, the bride and the string. In next subject, discussions about the characteristics of these three candidates is examined.

### **Comparison of the resonator type**

Categorization of the resonator type for the micro-capillary is important because it affects the resonance amplitude, the overall mass, the fabrication method and the transport strategy of the sample particles to the resonator. To choose a proper resonator type of micro-capillary, the three types of resonator shape are discussed.

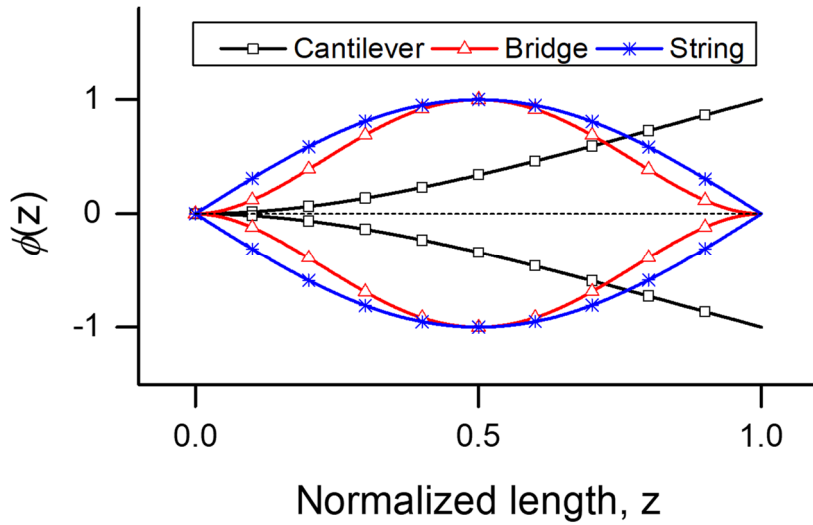


**Figure 2.2 Schematics of the normalized bending motion of cantilever, bridge and string type at the first resonance.**

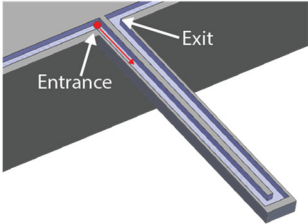
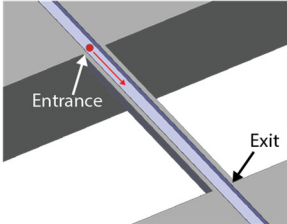
When the resonator length  $L$  is given, the mode shape function when the resonator vibrates of first resonance mode and boundary conditions of three resonator type are summarized to the Table 2.1. Figure 2.2 show the schematics of the three types of resonator bending motion. The *pros and cons* of those three types of resonator about the resonator performance is summarized to Table 2.2.

In Table 2.2, the larger the amplified motion of the resonator, the better the signal to noise ratio (SNR) is acquired, which reduces the overall system noise of the resonator system. Cantilever type has one free end of boundary whilst the bridge and string type have a clamped at both ends. If the equal external

**Table 2.1** Normalized mode shape functions and the boundary conditions of the three cases of the resonator type.

Type	Mode shape function ( $\phi_0(z)$ )	Normalization factor (A)	Wavenumber ( $\beta$ )	Boundary condition
Cantilever	$A[\cos(\beta z) - \cosh(\beta z) - B(\sin(\beta z) - \sinh(\beta z))]$ $\left( B = \frac{\cos(\beta L) + \cosh(\beta L)}{\sin(\beta L) + \sinh(\beta L)} \right)$	0.5000	$\frac{1.8751}{L}$	$\begin{aligned} \phi(0) &= 0 \\ \frac{\partial \phi(0)}{\partial z} &= 0 \\ \frac{\partial^2 \phi(0)}{\partial z^2} &= 0 \\ \frac{\partial^3 \phi(0)}{\partial z^3} &= 0 \end{aligned}$
Bridge	$A[\cos(\beta z) - \cosh(\beta z) - B(\sin(\beta z) - \sinh(\beta z))]$ $\left( B = \frac{\cos(\beta L) - \cosh(\beta L)}{\sin(\beta L) - \sinh(\beta L)} \right)$	0.6297	$\frac{4.7300}{L}$	$\begin{aligned} \phi(0) &= 0 \\ \phi(L) &= 0 \\ \frac{\partial \phi(0)}{\partial z} &= 0 \\ \frac{\partial \phi(L)}{\partial z} &= 0 \end{aligned}$
String	$A \sin(\beta z)$	1.0000	$\frac{\pi}{L}$	$\begin{aligned} \phi(0) &= 0 \\ \phi(L) &= 0 \\ \frac{\partial^2 \phi(0)}{\partial z^2} &= 0 \\ \frac{\partial^2 \phi(L)}{\partial z^2} &= 0 \end{aligned}$

**Table 2.2 Comparison of the resonator types**

	<b>Cantilever</b>	<b>Bridge or string</b>
		
<b>Particle clogging probability</b>	High	Low (Better)
<b>Motion of amplitude</b>	High (Better)	Low
<b>Systems dynamic bandwidth cost</b>	High	Low (Better)
<b>Fabrication difficulty</b>	High	Low (Better)

force applied those of resonator, the cantilever type gains the best SNR, string type is second and bridge type has the lowest SNR ratio according to their boundary conditions which restraints resonance amplitude.

The aspect of the control of resonator system, a passing velocity of individual particles is limited by the system's dynamic bandwidth. The case of cantilever type resonator, when a particle in transit the direction is switched at the apex, frequency fluctuation is steeper than the other types. As a result, the cantilever

type resonator requires higher dynamic bandwidth than bridge or string type resonators. More detailed discussion of dynamic bandwidth is given later in Chapter 4.

To make micro-capillary to a mechanical resonance structure, choosing a bridge or string shape rather than cantilever shape is a straightforward since fabricating a cantilever shape by bending the stretched micro-capillary seems complicated. Also, the cantilever type resonator has shortcoming at the bent fluidic corner which increases clogging the particles, the resonator usability is lowered than bridge and string type (See Table 2.2). In conclusion, the bridge and string type resonator structure is determined to make micro-capillary to mechanical resonator platform.

### **Driven harmonic oscillation of micro-capillary resonator**

The resonance model of micro-capillary resonator can be regarded as a driven harmonic oscillator. The general driven harmonic oscillator model is applied to micro-capillary resonator.

The resonance motion of the continuum mechanical system of the resonator can be simplified into a harmonic oscillator model which is composed of single mass, spring, and damper with one degree of freedom of vibration. When the external periodic force  $F(t) = F_0 \cos(\omega t)$  is applied to the micro-capillary resonator, the simplified model can be regarded as a lumped-element driven harmonic oscillator with the differential equation as below

$$m \frac{d^2 z}{dt^2} + c \frac{dz}{dt} + kz = F(t) \quad (2.5)$$

where  $m$  is the mass,  $c$  is the damping coefficient, and  $k$  is the spring constant.

The solution of (2.5) is obtained by applying the specific steady solution  $z(t) = z_0 e^{i\omega t}$  with the amplitude constant of  $z_0$

$$z_0 = \frac{F_0}{m} \frac{1}{(\omega_0^2 - \omega^2) + \frac{i\omega\omega_0}{Q}} \quad (2.6)$$

where  $Q = m\omega_0/c$  is the Quality factor,  $\omega_0$  is the first resonance frequency of the oscillator under the slight damping condition. The absolute amplitude of  $z_0$  is derived as

$$|z_0| = \frac{F_0}{m} \frac{1}{\sqrt{(\omega_0^2 - \omega^2)^2 + \left(\frac{\omega\omega_0}{Q}\right)^2}} \quad (2.7)$$

and the phase as

$$\arg(z_0) = \arctan\left(\frac{\frac{\omega\omega_0}{Q}}{\omega_0^2 - \omega^2}\right) \quad (2.8)$$

### **Resonance frequency and effective parameter**

The eigenfrequency of equation (2.1) can be expressed as

$$\omega_n = \beta_n^2 \sqrt{\frac{EI_x}{\rho A}} \quad (2.9)$$

With the slight damping condition, the eigenfrequency is close to resonance frequency of the resonator.

To simplify the equation of resonance motion to the driven harmonic oscillation, the representative physical parameters of mass and stiffness of the resonator can be converted to effective parameter, which is calculated from the multiplying the mode shape  $\phi(z)$  to the equation (2.1) and integrated it over the entire resonator length  $L$  under first resonance mode

$$\int_0^L \rho A \frac{\partial^2 u(z, t)}{\partial t^2} dz + \int_0^L EI_x \frac{\partial^4 u(z, t)}{\partial z^4} dz = 0 \quad (2.10)$$

The equation (2.10) can be reformed as

$$\rho A \ddot{u}(t) \int_0^L \phi^2(z) dz + EI_x u(t) \int_0^L \phi''^2(z) dz = 0 \quad (2.11)$$

From the driven harmonic equation (2.5), the effective parameters are expressed as

$$m_{eff} = \rho A \int_0^L \phi^2(z) dz \quad (2.12)$$

$$k_{eff} = EI_x \int_0^L \phi''^2(z) dz$$

Then the first resonance frequency is denoted as

$$\omega_0 = \sqrt{\frac{k_{eff}}{m_{eff}}} \quad (2.13)$$

## 2.2. Tensile force applied to the string type resonator

A string type micro-capillary resonator tends to have a tensile stress ( $\sigma$ ). With the consideration of a tensile force  $N = \sigma A$  on the micro-capillary, the equation of motion (2.4) can be described by

$$\rho A \frac{\partial^2 u(z, t)}{\partial t^2} + EI_x \frac{\partial^4 u(z, t)}{\partial z^4} - N \frac{\partial^2 u(z, t)}{\partial z^2} = 0 \quad (2.14)$$

Assuming the mode shape function has exponential term of  $U(z) = C e^{sz}$  and solve the differential equation of (2.14) can be expressed as,

$$s_{1,2}^2 = \frac{N}{2EI_x} \left( 1 \pm \sqrt{1 + \frac{4\rho A \omega^2 EI_x}{N^2}} \right) \quad (2.15)$$

String type configurations have the boundary at both ends are assumed to be simply supported doubly clamped beam with the conditions

$$U(0) = U(L) = \frac{\partial^2 U(0)}{\partial z^2} = \frac{\partial^2 U(L)}{\partial z^2} = 0 \quad (2.16)$$

Applying the boundary conditions (2.16) and eigenvalue (2.15) with mode shape function (2.4) into (2.14), which yields the Eigen frequency  $\omega$  can be derived as

$$\omega = \left(\frac{\pi}{L}\right) \sqrt{\frac{N}{\rho A} + \left(\frac{\pi}{L}\right)^2 \frac{EI_x}{\rho A}} \quad (2.17)$$

In equation (2.17), the eigenfrequency is the sum of stress (the first term in the square root) and unstressed beam (second term). If the string type resonators have a large tensile force and length compared than the short length of flexural rigidity of beam, the Eigen frequency of the resonator shows simply string motion ( $\omega = \pi/L\sqrt{N/(\rho A)}$ ) while the resonator of the opposite case behaves like simply supported beam.

### **2.3. Effect of boundary condition of the bridge type resonator**

In the MEMS process for resonator systems, the resonator and boundary support are fabricated together in a silicon wafer. Both the resonator itself (suspended structure of the resonator) and the clamp side are made of the same material, which can be regarded as monolithic structures in which strongly bonded together. It makes the boundary condition of the MEMS resonator to a moment constraint.

However, unlike the MEMS resonator, a micro-capillary resonator could not have a monolithic boundary clamp, an assembly technique to form a resonator structure is required. The confinement properties at the boundary region can be varied depending on the mechanical contact, bonding strength, and Young's modulus of the bonding material while the construction of assembly process.

**Table 2.3 Boundary conditions of bridge type resonator and its resonance frequencies**

Boundary condition	Resonance frequency
<p><b>Pinned-pinned</b></p> 	$\omega = \left( \frac{9.8696}{L^2} \right) \sqrt{\frac{EI_x}{\rho A}}$
<p><b>fixed-pinned</b></p> 	$\omega = \left( \frac{15.418}{L^2} \right) \sqrt{\frac{EI_x}{\rho A}}$
<p><b>Fixed-fixed</b></p> 	$\omega = \left( \frac{22.373}{L^2} \right) \sqrt{\frac{EI_x}{\rho A}}$

This variation of boundary condition results the various wavenumber of the mode shape (See the equation (2.4)) of the micro-capillary resonator.

A total of three resonator boundary conditions are possible by using the three constraints; pinned-pinned, pinned-fixed and fixed-fixed at both ends. Applying the boundary conditions to the differential equation (2.1), the resonance frequency of the resonator can be obtained (See Table 2.3).

## 2.4. Mode-split of the elliptical cross-section resonator

If the cross-section of the micro-capillary has a perfectly symmetrical circle, it would display out-of-plane motion vibration with the identical frequency along all directions. However, when the cross-section has an elliptical shape with different diameters along the major and minor axes (Figure 2.1 (b)), the resonance motion is divided into the two-orthogonal vibrations due to change in area moment of inertia.

Assuming that the elliptical cross-section has the major and minor axis diameter  $D_{maj}$  and  $D_{min}$ , respectively with longitudinal length of  $L$  and fixed-fixed boundary configuration. And the inner diameter has an identical shape of the outer ellipse with multiplied by ratio  $\chi (= \frac{D_{inner}}{D_{outer}})$ . The resonance frequencies along the major and minor axes are obtained as

$$\omega_{maj} = \left(\frac{\lambda}{L}\right)^2 \sqrt{\frac{EI_{maj}}{\rho A}}, I_{maj} = \frac{\pi}{64} D_{maj}^3 D_{min} (1 - \chi^4) \quad (2.18)$$

$$\omega_{min} = \left(\frac{\lambda}{L}\right)^2 \sqrt{\frac{EI_{min}}{\rho A}}, I_{min} = \frac{\pi}{64} D_{min}^3 D_{maj} (1 - \chi^4) \quad (2.19)$$

where  $\lambda (= \beta L)$  is the mode number and  $I_{maj}$ ,  $I_{min}$  represents the inertia at the major and minor axes, respectively. Note that the micro-capillary's resonance mode shape, Young's modulus and mass ( $m = \rho AL$ ) are invariant even if the cross-section is elliptic, thus only the area moment of inertia of the resonator yields the different resonance frequency of mode-split resonances.

The asymmetry factor  $\Omega \equiv (D_{maj} - D_{min})/D_{maj}$  is defined to indicate the asymmetry ratio of micro-capillary resonator, and this can be represented as another expression.  $\Omega \equiv (\omega_{maj} - \omega_{min})/\omega_{maj}$ , which can be derived from the equation (2.18) and (2.19).

## 2.5. Axis rotation

Figure 2.3 illustrates the elliptical cross-section micro-capillary laid on the resonator jig with rotation angle  $\alpha$  with respect to y-axis.  $x', y'$  are the major and minor axes in the local coordinate respectively, where  $x, y$  are represents the global coordinate. If the external periodic force  $\vec{F}(t)$  generated beneath in direction of y-axis, the amplitude of applied force which induces resonance corresponds the projection amplitude of  $\vec{F}(t)$  along its own axis.

Regarding the resonance motion of each axis as the model of external force driven harmonic oscillation, the amplitude of the resonance motion of the resonator becomes

$$|z_{0,maj}| = \frac{|F_0|}{m_{eff}} \frac{1}{\sqrt{(\omega_{0,maj}^2 - \omega^2)^2 + \left(\frac{\omega\omega_{0,maj}}{Q_{maj}}\right)^2}} \sin(\alpha) \quad (2.20)$$

$$|z_{0,min}| = \frac{|F_0|}{m_{eff}} \frac{1}{\sqrt{(\omega_{0,min}^2 - \omega^2)^2 + \left(\frac{\omega\omega_{0,min}}{Q_{min}}\right)^2}} \cos(\alpha) \quad (2.21)$$

where the subscripts maj and min are referred to the major and minor axes, respectively. The maximum amplitude occurs the driving frequency matches to the resonance frequency of the resonator. The maximum amplitude becomes

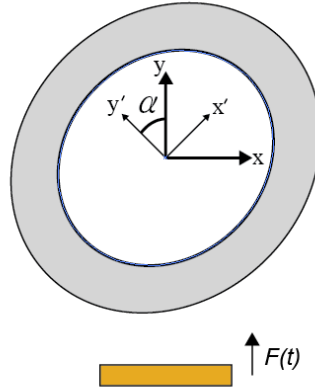


**Figure 2.3 Rotation of the resonator with azimuthal angle  $\alpha$  with respect to y-axis. The external force  $F(t)$  applied to the resonator is beneath the resonator.**

$$\max(|z_{0,min}|) = \frac{|F_0|}{k_{eff,min}} Q_{min} \cos(\alpha) \quad (2.22)$$

$$\max(|z_{0,max}|) = \frac{|F_0|}{k_{eff,maj}} Q_{maj} \sin(\alpha) \quad (2.23)$$

The motion of the ellipse center  $(x'_c, y'_c)$  in the local coordinate can be derived from the superposition of major and minor axes resonance motion

$$(x'_c, y'_c) = (z_{0,maj} \cos(\omega t + \varphi_{maj}), z_{0,min} \cos(\omega t + \varphi_{min})) \quad (2.24)$$

Translate the ellipse center position  $(x_c, y_c)$  at the global coordinate can be obtained by applying the standard rotation matrix

$$\begin{pmatrix} x_c \\ y_c \end{pmatrix} = \begin{pmatrix} \cos\theta & -\sin\theta \\ \sin\theta & \cos\theta \end{pmatrix} \begin{pmatrix} x'_c \\ y'_c \end{pmatrix} \quad (2.25)$$

# **CHAPTER 3.**

## **MASS RESPONSIVITY**

In chapter 2, resonance motion of micro-capillary resonator was described in detail, and Eigenfrequencies of resonators in two different types (bridge and string) were calculated. In this chapter, relative shift of resonance frequency occurred when liquid or particle is introduced into the resonator is theoretically calculated using each resonator's resonance motion. In addition, tuning of resonator's dimension to enhance mass detection sensitivity is covered. Finally, noise of resonance frequency and limitation of mass detection according to the resonator system noise are analyzed.

### **3.1. Resonance frequency shift**

When mass of the microparticle or density of fluid containing particle loaded inside the micro-capillary resonator is shifted in change of its buoyant mass or density, resonance frequency of resonator undergoes downshift due to entire mass change by additional mass loading effect. Relation variation of resonance frequency shift to mass change depends on two parameters; size of the mass and position of the mass inside the resonator. Resonance frequency shift can be derived from Rayleigh-Ritz energy method [100].

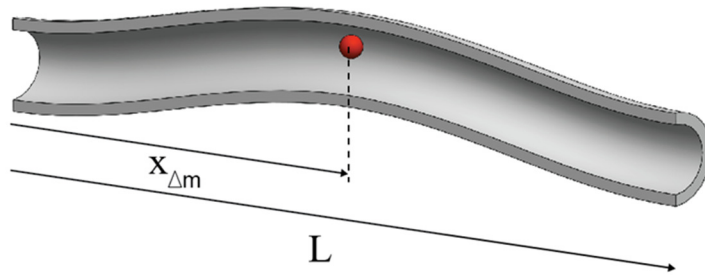


**Figure 3.1** The illustration of point mass of particles passing through the resonator.

### **Particle mass effect**

Figure 3.1 shows a particle with mass of  $\Delta m$  is loaded inside the resonator channel, where  $L$  is length of the resonator and  $x_{\Delta m}$  is position of the particle. When fluid having density of  $\rho_f$  is loaded into channel resonator, time averaged kinetic energy occurs throughout the resonator length can be expressed as

$$\begin{aligned}
E_{kinetic} &= \int_V \frac{1}{2} \rho(x) \omega_{\Delta m}^2 a^2 \phi^2(x) dV & (3.1) \\
&= \frac{1}{2} \omega_{\Delta m}^2 a^2 \int_V \rho(x) \phi^2(x) dV \\
&= \frac{1}{2} \omega_{\Delta m}^2 a^2 \int_V (\rho_r + L_{\Delta m} \delta(x_{\Delta m})) (\rho_{\Delta m} - \rho_f) \phi^2(x) dV \\
&= \frac{1}{2} \omega_{\Delta m}^2 a^2 \left[ (A_w \rho_w + A_f \rho_f) \int_0^L \phi^2(x) dx \right. \\
&\quad \left. + L_{\Delta m} A_{\Delta m} (\rho_{\Delta m} - \rho_f) \phi^2(x_{\Delta m}) \right] \\
&= \frac{1}{2} \omega_{\Delta m}^2 a^2 [m_{eff} + \Delta m_b \phi^2(x_{\Delta m})]
\end{aligned}$$

where  $\omega_{\Delta m}$  represents the resonance frequency when the particle  $\Delta m$  loaded,  $a$  is the amplitude of the mode shape,  $\phi$  is the normalized mode shape function along the resonator length,  $L_{\Delta m}$  is the length of the loaded particle,  $\delta$  is the Dirac delta function,  $A$  is the cross-sectional area, and  $m_{eff}$  is the effective mass of the resonator. The denoted parameters  $w, f, \Delta m, b$  represents the wall of the resonator, fluid, particle, and buoyant-mass, respectively. Note that according the normalized mode shape function (in Table 2.1), the square integration of  $\int_0^L \phi^2(x) dx$  becomes  $0.3965L$  when the resonator is beam and  $0.5L$  when the resonator is defined to string.

The strain energy can be obtained in similar method

$$E_{strain} = \int_V \frac{1}{2} E_r I_r a^2 \phi''^2(x) dV \quad (3.2)$$

$$= \frac{1}{2} k_{eff} a^2$$

$$= \frac{1}{2} m_{eff} \omega_0^2 a^2$$

where the  $\omega_0$  is the resonance frequency of the resonator without particle, denote  $r$  represents resonator. The strain energy during the resonance motion is stored to the resonator and assumed that the loaded mass  $\Delta m$  is small ( $m_{eff} \gg \Delta m$ ), therefore the mode shape function  $\phi(x)$  would not be changed significantly.

According to the Rayleigh-Ritz energy theorem [100], the time averaged in kinetic energy of the resonator during resonance motion is equal to that of the strain energy. The shifted resonance frequency  $\omega_{\Delta m}$  of the loaded resonator is obtained from the equation (3.1) and (3.2),

$$E_{strain} = E_{kinetic} \quad (3.3)$$

$$\frac{1}{2} m_{eff} \omega_0^2 a^2 = \frac{1}{2} \omega_{\Delta m}^2 a^2 [m_{eff} + \Delta m_b \phi^2(x_{\Delta m})]$$

$$\therefore \omega_{\Delta m}^2 = \omega_0^2 \frac{1}{1 + \frac{\Delta m_b}{m_{eff}} \phi^2(x_{\Delta m})}$$

When a particle is floated in the fluid, buoyant mass of the loaded mass is calculated by subtracting the fluid density to multiplying its volume ( $\Delta m_b = (\rho_{\Delta m} - \rho_f)V_{\Delta m}$ ).

Especially, the maximum frequency shift occurs when the particle passes through the center position of the resonator's suspended region, the equation (3.3) is simplified as below

$$\therefore \omega_{\Delta m} = \frac{\omega_0}{\sqrt{1 + \frac{\Delta m_b}{m_{eff}}}} \quad (3.4)$$

### **Particle inertia effect**

When a particle passing through the resonator's inner channel it is usually assumed that the position of particle is at the center of resonator cross-section area. With this assumption, the inertia variation of particle can be neglected, thus overall resonator inertia is invariant, only the mass loading affects the resonance frequency of resonator. However, if the particle position is located off the center of the resonator cross-section, particle's area moment of inertia becomes large, which could influence the resonance frequency of resonator.

Figure 3.2 illustrates the particle placed at the inner channel of resonator with offset ( $e_x, e_y$ ). To simplify, the shape of particle is modeled to cylinder which longitudinal direction arranged to that of resonator. The area moment of inertia of resonator can be calculated

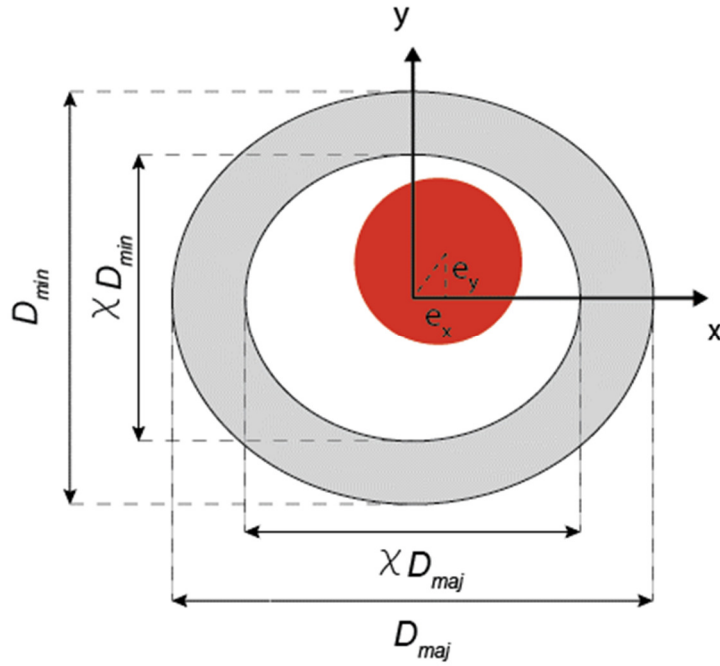


**Figure 3.2** The illustration of particle placed at the cross-section of resonator when particles center position has offset  $(e_x, e_y)$ .

$$I'_y = I_y + Ad_x^2 \quad (3.5)$$

$$I'_x = I_x + Ad_y^2$$

where  $I'_x, I'_y$  are the area moment of inertia of resonator with respect to the  $x, y$  axes, respectively.  $I_x, I_y$  are the resonator's area moment of inertia with respect to its centroidal axis.  $A$  is the cross-sectional area of resonator. when the particle located at the  $(e_x, e_y)$  position at the cross-section of resonator, the centroid of resonator is moved with eccentricity  $(d_x, d_y)$ , which can be calculated as

$$d^2 = \left( \frac{m_p}{m_r + m_p} \right)^2 e^2 \quad (3.6)$$

where  $m_p$  and  $m_r$  represent the mass of particle and resonator, respectively.

The area moment of inertia of particle  $I_p$  and resonator  $I_r$  are as below,

$$I_p = \frac{\pi}{64} D_p^4 \quad (3.7)$$

$$I_r = \frac{\pi}{64} (D_o^4 - D_i^4) = \frac{\pi}{64} D_o^4 (1 - \chi^4)$$

where  $D_p$  is the diameter of particle.

Now, the time averaged strain energy of the resonator can be calculated

$$E_{strain} = \int_0^L \frac{1}{2} EI a^2 \phi''^2(x) dx \quad (3.8)$$

$$= \frac{1}{2} a^2 \int_0^L \left( E_r \phi''^2(x) (I_r + \delta(x_{\Delta m}) L_p I_p) \right) dx$$

$$= \frac{1}{2} a^2 k_{eff} \left( 1 + \frac{L_p U''(x_{\Delta m})^2 I_p}{\int_0^L U''(x)^2 dx I_r} \right)$$

$$= \frac{1}{2} a^2 m_{eff} \omega_0^2 \left( 1 + \frac{L_p U''(x_{\Delta m})^2 A_r d^2}{\int_0^L U''(x)^2 dx I_r} \right)$$

where  $L_p$  is the length of the particle. Denotes r and p represent the resonator and particle, respectively. With equation (3.9) applying Rayleigh-Ritz energy theorem, repeat the calculation (3.3) then,

$$E_{strain} = E_{kinetic} \quad (3.9)$$

$$\begin{aligned} \frac{1}{2} a^2 m_{eff} \omega_0^2 \left( 1 + \frac{L_p U''(x_{\Delta m})^2 A_r d^2}{\int_0^L U''(x)^2 dx I_r} \right) \\ = \frac{1}{2} \omega_{\Delta m}^2 a^2 [m_{eff} + \Delta m_b \phi^2(x_{\Delta m})] \\ \therefore \omega_{\Delta m}^2 = \omega_0^2 \frac{1 + \frac{L_p U''(x_{\Delta m})^2 A_r d^2}{\int_0^L U''(x)^2 dx I_r}}{1 + \frac{\Delta m_b}{m_{eff}} \phi^2(x_{\Delta m})} \end{aligned}$$

### Fluid density change

Change in density of fluid filled in the micro-capillary resonator channel occurs the entire resonator channel. The equation (3.3) can be modified regarding fluid changes from  $f_1$  to  $f_2$  as below

$$\begin{aligned} \therefore \omega_{f_2} &= \frac{\omega_{f_1}}{\sqrt{\frac{m_{eff,f_2}}{m_{eff,f_1}}}} = \omega_{f_1} \sqrt{\frac{A_w \rho_w + A_{f_1} \rho_{f_1}}{A_w \rho_w + A_{f_2} \rho_{f_2}}} \\ &= \omega_{f_1} \sqrt{\frac{1 + \frac{A_f \rho_{f_1}}{A_w \rho_w}}{1 + \frac{A_f \rho_{f_2}}{A_w \rho_w}}} \end{aligned} \quad (3.10)$$

The area of fluid  $f_1$  and  $f_2$  in the micro-capillary resonator channel are equal ( $A_f = A_{f_1} = A_{f_2}$ ), thus resonant frequency ratio ( $\omega_{f_2}/\omega_{f_1}$ ) is only a function of density difference of the fluid (See equation (3.10)).

### 3.2. Mass responsivity

For mass sensing application of micro-capillary resonator, it is important to define the output signal ratio of the resonator as a function of the measured input variable which works as a specific parameter. In case of micro-capillary resonator, the analyte's specific parameter is mass and the output signal of the resonator is resonance frequency shift.

The mass responsivity at a certain mass  $m_{eff}$  is given by [101]

$$\mathfrak{R} = \frac{\partial\omega}{\partial m_{eff}} \quad (3.11)$$

The equation (3.11) is valid where the relation of the mass variation and resonance frequency change remains in linear regime.

In terms of the resonance frequency obtained from a certain mass of resonator and slight damp resonance mode condition, the mass responsivity of the micro-capillary resonator is obtained from the equation (2.13) of Eigenfrequency as a function of the effective parameters

$$\begin{aligned} \partial\omega &= -\frac{\sqrt{k_{eff}}}{2\sqrt{m_{eff}^3}}\partial m_{eff} = -\frac{1}{2}\frac{1}{m_{eff}}\sqrt{\frac{k_{eff}}{m_{eff}}}\partial m_{eff} \\ \frac{\partial\omega}{\partial m_{eff}} &= -\frac{1}{2}\frac{1}{m_{eff}}\omega_0 \end{aligned} \quad (3.12)$$

From a point of view where the fluid density change matters, the equation (3.12) is represented by another expression as

$$\mathfrak{R} = -\frac{1}{2} \frac{1}{\rho_f + \frac{A_w}{A_f} \rho_w} \omega_0 \quad (3.13)$$

### 3.3. Dimension tuning for increase mass responsivity

As seen in equation (3.11), mass responsivity of the micro-capillary resonator is inversely proportional to total mass of the resonator. Therefore, mass responsivity increases by reducing mass of resonator, which induces large shift of resonance frequency when a same mass of particle loaded. This is one of the methods for increasing output signal to frequency noise of resonator system. The mass of the micro-capillary resonator can be expressed as function of outer diameter  $D_{outer}$ , inner and outer diameter ratio at the cross-section  $\chi$ , overall length  $L$ , and the liquid density  $\rho_f$  (See Figure 2.1 (b)). Sensitivity of mass responsivity can be controlled by tuning these parameters.

Figure 3.3 shows various resonance frequency shifts of the micro-capillary resonator if a particle with specific mass is loaded and dimension parameters of micro-capillary change.

If resonator's mass responsivity to target particle is too low than frequency noise, it is impossible to distinguish the resonator's output signal due to particle from system noise. Replacing the micro-capillary resonator which has more lightweight can improve mass responsivity even if the resonator system has a same frequency noise.

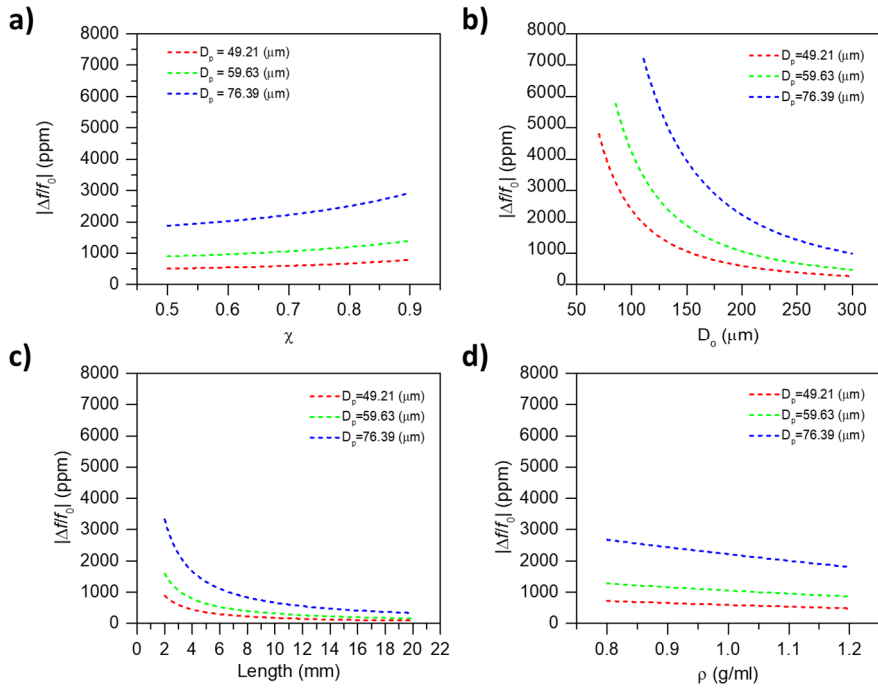


**Figure 3.3** The mass responsivity variation by tuning the micro-capillary resonator dimension and liquid density. If particle placed inside the middle of the resonator, various frequency shifts of the resonator by adjusting (a) inner and outer cross-section diameter ratio, (b) outer diameter, (c) length, and (d) density of fluid is plotted. With assumption that the density of micro-capillary and the particle are 2.23 and 2.46 g/ml, respectively.

### 3.4. Noise and limit of detection

When the micro-capillary resonator is used as a mass sensor, obtaining the limit of the mass sensitivity should be considered. Identifying the limit of detection can be obtained by the calculation of the mass responsivity of the resonator and system noise which is induced from the oscillation system and the resonator. If

the output signal of micro-capillary resonator is set to its resonance frequency, the system noise of the resonator is defined as the resonance frequency jitter which is the combination of the mechanical disturbance of the resonator and the refinements of the rest of the resonator system components including oscillator, frequency recorder, power supply, etc.

The resonance frequency noise from the resonator can be reduced by minimizing the mechanical surrounding noise that includes the temperature, undesired external vibration or pressure, purity of the liquid flowing inside of resonator, and the other factors. On the system components, precise clock comparator with stable reference clock and low harmonic distortion electric circuit can provide sufficient low frequency jitter.

### **Quality factor**

The Quality factor is defined as the available oscillation cycles once the maximum potential energy is released while the resonance motion of resonator. In another expression, Quality factor is the ratio of stored energy in the maximum strain energy in oscillation motion to the energy dissipation per a single resonance cycle. The dissipated energy during resonance cycle is the key parameter to evaluate that how the resonator behaves close to the ideal oscillator.

Low energy loss during the mechanical motion, which means the resonator has the high-quality factor, is desirable to most applications of mechanical resonators. The mathematical expression of the Quality factor is as below

$$Q \equiv 2\pi \frac{\text{energy stored}}{\text{Energy dissipated per cycle}} = \frac{f_0}{\Delta f} \quad (3.14)$$

where  $\Delta f$  is the full width at half maximum (FWHM) of the resonator.

The Quality factor of resonator consists of various mechanical dissipation factors. The total Quality factor of resonator is calculated as

$$\frac{1}{Q} = \frac{1}{Q_{damping}} + \frac{1}{Q_{clamping}} + \frac{1}{Q_{internal}} + \dots \quad (3.15)$$

where  $Q_{damping}$  is the viscous damping effect by interaction with surrounding medium,  $Q_{clamping}$  is the energy transfer rate to support material at the clamp site, and  $Q_{internal}$  is bulk energy dissipation mechanism occurred in the structure material.

The most energy loss mechanism during the resonance motion of the resonator surrounded in moderate air condition is viscous damping. Under the moderate air condition, many of resonators reported that they show a quality factor of approximately 100 [102]–[104] and usually it rises to 1,000 or more in the vacuum condition [15], [98].

The frequency response of the amplitude motion of resonator shows a simple harmonic oscillator peak. The Quality factor parameter can be extracted using the nonlinear curve fitting of simple harmonic oscillation formula (equation (2.7)) by applying to the frequency response peak of the resonator.

## Allan deviation

Allan deviation, or the Allan variance which is the square of the Allan deviation, is the stability characteristic indicator for the frequency-based resonator system. If the frequency measuring system for the resonator measures the resonance frequency with the fixed time interval  $\tau$ , the Allan variance is defined by

$$\sigma^2(\tau) = \frac{1}{2} \langle (\Delta f)^2 \rangle = \frac{1}{2(N+1)} \sum_{i=1}^N \frac{(f_{i+1,\tau} - f_{i,\tau})^2}{f_0^2} \quad (3.16)$$

where  $f$  is measured frequency and  $N$  is number of sample.

In the region where the short time period  $\tau$ , the Allen deviation tends to be larger because of white noise become dominant on the resonator. The white noise decreases when  $\tau$  increases, however, the factor of long-term drift of the resonator governs the frequency stability of the system which leads the Allan deviation to be increased. Most of the resonators in nature, the Allan variances of them follow the V-shape curve with respect to the  $\tau$ , that provides the determination of optimal period of frequency measurement for given resonator-monitoring system where the curve is the lowest [99].

## Limit of detection

Limit of detectable mass ( $m_{LOD}$ ) of the resonator can be calculated from the inverse responsivity of the resonator multiplied to frequency noise at the given measured period  $\tau$  as below

$$m_{\text{LOD}} = \frac{\sigma(\tau)}{\mathfrak{R}} \quad (3.17)$$

Equation (3.11) implies the limit of detectable mass is equal to effective mass converted from the average frequency noise level. Practical measurable limit of detectable mass can be obtained by multiplying three times of the theoretical  $m_{\text{LOD}}$  in equation (3.17) ( $m_{\text{LOD},\text{practical}} = 3m_{\text{LOD}}$ ).

# **CHAPTER 4.**

## **OPERATION PRINCIPLES**

This chapter explains a working principle and its implementation on how micro-capillary resonator is actuated and its resonance frequencies are monitored.

To setup a frequency readout instrument for micro-capillary resonator, a mechanical contact measurement instrument and a non-contact laser-based measurement instrument were employed. A contact readout instruments has a piezoelectric transduction principle, and a non-contact instrument has an optical out-of-plane displacement measuring principle using astigmatic lens.

For micro-capillary resonator without mode-split motion, a simple self-oscillating circuit was used for actuation in Eigenmode frequency and digital phase locked loop (PLL) was employed to operate the mode-split two adjacent resonance frequencies along major and minor axes of the resonator using digital system's high performance of the decoupling signal processor.

In summary, two combinations of the readout-oscillation systems for driving micro-capillary resonator were used; one is a contact piezoelectric readout with self-oscillation circuit and the other is a non-contact method of astigmatic detection readout with digital phase locked loop system.

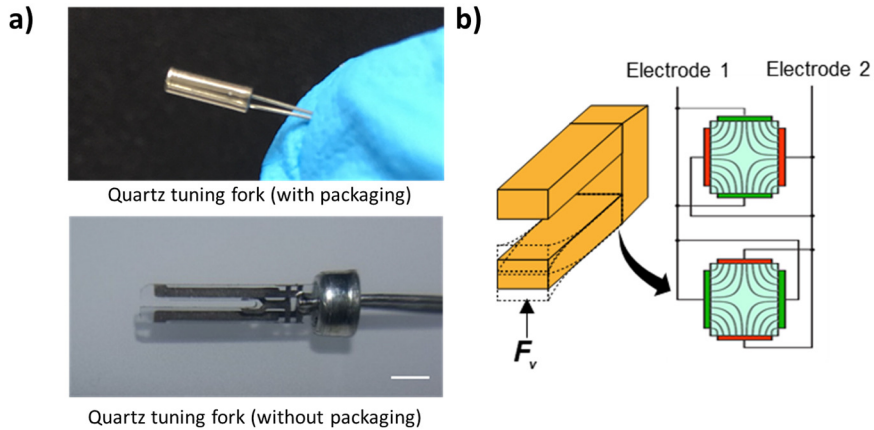


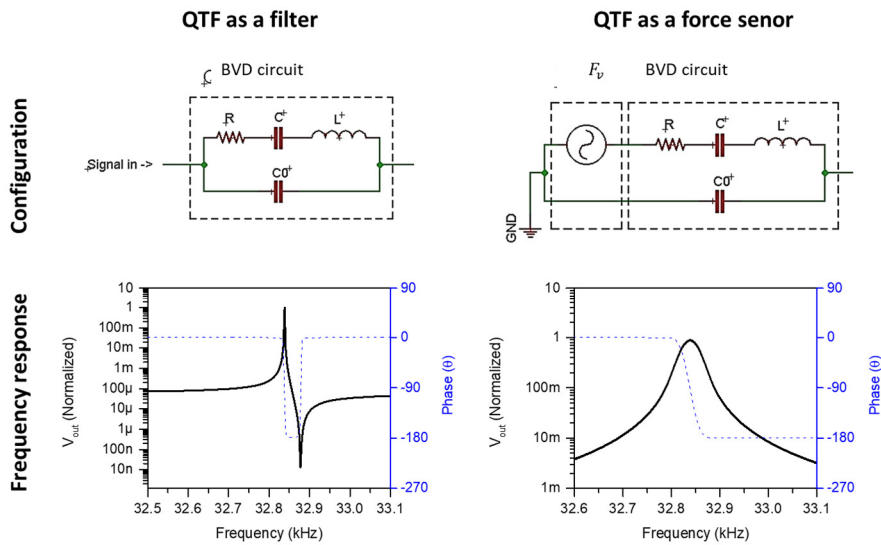
**Figure 4.1 (a) A QTF before and after the package is removed. Scale bar is 1 mm. (b) The illustration of vertical force applied to the end of cantilever of QTF and the electric field generated inside the QTF material.**

## **4.1. Operation scheme of string type micro-capillary resonator**

### **Piezoelectric readout**

Piezoelectric effect refers to accumulation of electrical charge by converting internal stresses applied to certain solid materials into electrical charge [105]. The electrical charge inside the piezoelectric transducer generates a current flow through readout system, and transimpedance amplifier (TIA) converts a current induced by a mechanical stress into a voltage, thus enhancing usability for signal detection.

Figure 4.1 (a) shows an industrial product of a quartz tuning fork (QTF) with resonance frequency of 32.768 kHz. QTF transducer can be easily produced by

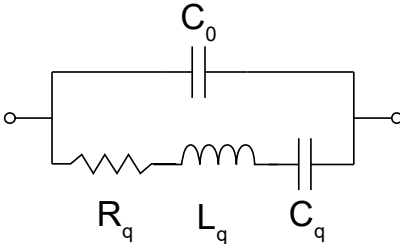
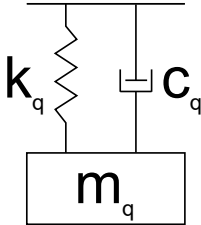


**Figure 4.2 Comparison the electrical configurations of QTF and its resonance responses as a filter and an external force sensor.**

removing hermetic seal package of an industrial quartz crystal oscillator which has QTF inside. When QTF posed vertically (Figure 4.1 (b)) and vertical force ( $F_v$ ) is applied to the end of the cantilever in an out-of-plane direction, an internal stress on the cantilever of quartz material is generated, accumulating corresponding electrical charge at the electrode coated on the outer surface of the QTF. It can be used as a force sensing probe when two electrodes are connected to external readout system.

Equivalent electric circuit of piezoelectric effect of QTF is modeled as a Butterworth Van-Dyke (VBD) circuit, and a physical mechanical signal is

**Table 4.1 The analogy of electrical and mechanical model of Butterworth Van-Dyke circuit.**

Relation	Electrical model	Mechanical model
		
Applied Voltage	$\alpha V$	$F$
Inductance	$L$	$m/2\alpha^2$
Capacitance	$C$	$2\alpha^2/k$
Resistance	$R$	$mc/(2\alpha^2\sqrt{km})$
Resonance frequency	$\frac{1}{2\pi\sqrt{LC}}$	$1/2\pi\sqrt{k/m}$

converted to electrical signal and vice versa according to piezoelectric coefficient  $\alpha$  (Table 4.1).

Figure 4.2 shows a modeling of QTF force sensor upon application of external force  $F_v$ . When QTF is used as a filter configuration on electrical circuit, anti-resonance peak is generated along with 32.768 kHz resonance frequency due to parasitic capacitance of QTF in VBD circuit. On the other hand, Lorentzian peak that doesn't include anti-resonance peak is shown when the current

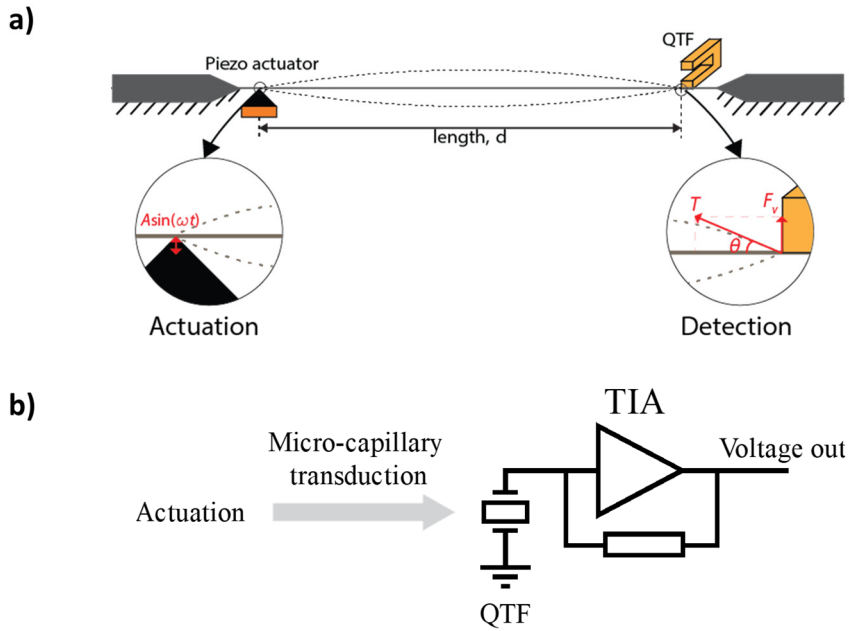


**Figure 4.3 (a) Schematic of actuation and detection of vibration of the micro-capillary resonator and (b) its electrical transduction.**

generated by external force  $F_v$  passes through equivalent RLC circuit of the VBD model (Note that one side of QTF electrode should be grounded). The VBD circuit is the simplified model to describe the electrical behavior of the piezoelectric material, however, it is possible that QTF transducer has a general complex electrical model and has a non-linear stress-strain mechanical relation that shows mixed behavior of the filter and force sensor configuration models during transducing in reality.

Out-of-plane vibration can be measured by contacting an end of QTF cantilever to the micro-capillary resonator (Figure 4.3 (a)). Similar to Melde's experiment [106], the response of micro-capillary resonator was measured from the

opposite side of QTF when it was actuated from left actuation node located at distance  $d$  apart from the QTF side (see Figure 4.3 (a)).

Mechanical contact of QTF plays a role of the boundary node to the micro-capillary resonator and a sensor node as a force sensing probe. If the effective stiffness of QTF cantilever at its end is larger than that of micro-capillary resonator, vibration amplitude of the QTF's cantilever diminishes and that of the micro-capillary motion dominates on the two-coupled mechanical deflection system.

When the operation of the actuating node induces out-of-plane vibration of the micro-capillary, the vertical force  $F_v$ , which is the vertical component of the applied axial tension  $T$ , is felt by the QTF and is given by

$$\begin{aligned}
 F_v &= T \sin(\theta) \cong T \theta = T \frac{d}{dz} u(z, t) = T \frac{d}{dz} \phi(x) \sin(\omega t + \varphi) & (4.1) \\
 &\cong T A^* \sqrt{\frac{T}{2EI} \left( \sqrt{1 + \frac{4m\omega^2 EI}{T^2}} - 1 \right)} \cos(\beta d) \sin(\omega t + \varphi) \\
 &\cong G \sin(\omega t + \varphi)
 \end{aligned}$$

where  $\theta$  is the tangent angle of the micro-capillary at the QTF node,  $\omega$  is the excitation frequency,  $t$  is time,  $A^*$  is the amplitude constant,  $d$  is the length of the micro-capillary and the rest of the other symbols are already mentioned in Chapter 2.

The vertical reflection  $f_v$ , of which magnitude is proportional to the vibration amplitude of the micro-capillary is transmitted to the QTF, then, induce a force vibration at one of two cantilevers with the excitation frequency  $\omega$ . Dynamic

amplitude of the equivalent second order mechanical system for the QTF with an external input of  $F_v$  is transduced to dynamic current generation at the RLC components in a Butterworth Van-Dyke circuit.

A transimpedance amplifier can be configured with a gain resistor and connected to one electrode of the QTF for current-to-voltage conversion with a gain while the other electrode of the QTF was grounded (Figure 4.3 (b)).

### **Self-oscillation scheme**

For mass measurement of fluids and microparticle suspension inside the resonator, the oscillator system is required to actuate the resonator in its resonance frequency. For monitoring the resonance frequency of the resonator, the respond signal of QTF attached on the micro-capillary can be analyzed to measure a vibration amplitude and phase delay of the resonance motion. The resonance frequency shifts occur when the mass perturbation of the resonator is introduced by either change of internal fluid density or flow of added particle through the channel.

If resonance frequency shift is slow and real-time monitoring of the its response is not required, it is sufficient to monitor the resonance frequency with lock-in amplifier and precise clock source using frequency sweep method. However, if fast dynamic response is expected, oscillator and measurement system should be built to have a corresponding dynamic response. If particle transit time inside the embedded channel of the resonator is  $\sim 100$  ms, measurement system should

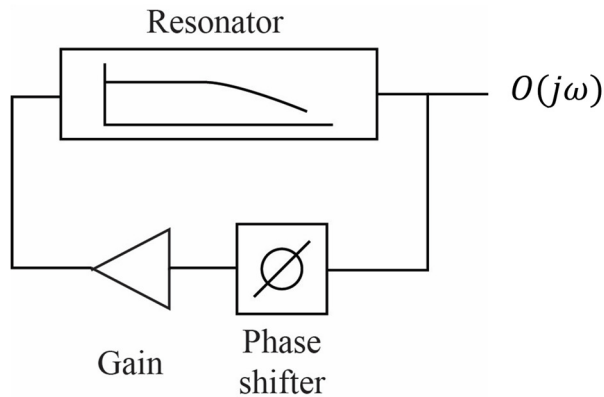


**Figure 4.4 Block diagram of self-oscillation system.**

be able to resolve 1 ms, requiring 1 kHz of dynamic bandwidth for the entire system.

The easiest way to realize high dynamic bandwidth oscillator is to employ phase shifter and gain amplifier within a feedback loop (Figure 4.4). This self-oscillation system in which output signal gets phase shifted, amplified, and fed back to oscillate the resonator is can be easily realized without any precision clock source or other expensive components, reducing unwanted noise of the system. For ideal resonator system, output signal gets lagged by  $\pi/2$ , being advanced by phase shifter to compensate for the delay, and the resonator can be kept oscillating if gain is tuned to be larger than 1.

For analyzing the integrated of the resonator and self-oscillation circuit system, calculation the transfer function of it in the frequency domain is required. In the frequency domain, resonator as a simple harmonic oscillator model within a linear amplitude response has a transfer function below

$$TF(j\omega) = \frac{1}{k} \left( \frac{\omega_0^2}{\omega_0^2 - \omega^2 + \frac{j\omega_0\omega}{Q}} \right) \quad (4.2)$$

When the driver system has a gain and phase delay control unit ( $K(j\omega)$  and  $e^{j\phi}$ ), the output of the closed loop system  $O(j\omega)$  is given

$$\begin{aligned} O(j\omega) &= \frac{TF(j\omega)}{1 - K(j\omega)e^{j\phi}TF(j\omega)} \quad (4.3) \\ &= \frac{1}{k} \left( \frac{\omega_0^2}{\omega_0^2 \left( 1 - \frac{K(j\omega)}{k} \cos(\phi) \right) - \omega^2 + j\omega\omega_0 \left( \frac{1}{Q} - \frac{K(j\omega)}{k} \frac{\omega_0}{\omega} \sin(\phi) \right)} \right) \end{aligned}$$

where the  $1/k$  represents static deflection of the resonator, and the rest term represents the system's admittance of the frequency input. According to the admittance in the equation (4.3), the closed loop system's resonance frequency differs from the resonator as  $\omega_0^2 \left( 1 - \frac{K(j\omega)}{k} \cos(\phi) \right)$ , also the quality factor  $\left( \frac{1}{Q} - \frac{K(j\omega)}{k} \frac{\omega_0}{\omega} \sin(\phi) \right)^{-1}$ .

If the gain controller has flat response for the frequency, the output of the system including resonance frequency and the quality factor is only adjusted by the phase controller. To match the characteristics of the entire system to the resonator, the phase delay can be settled to  $\pi/2$ .

## **4.2. Operation scheme of bridge type micro-capillary resonator**

To operate a bridge type micro-capillary resonator, this dissertation introduces an optical astigmatic detection system as the out-of-plane displacement measurement sensor and digital PLL system to oscillating the resonator.

Optical measurement technique radiates laser to a surface of the resonator to detect displacement amplitude. Optical-lever detection technique is the one of the representative optical measurement technology, which can amplify the small reflected angle change of the resonator to achieve large output responsivity via objective lens. This amplification of the resonance motion signal enhances signal-to-noise ratio and is primarily used for ultrasensitive measurement technique for applications including atomic force microscopy, MEMS deflection sensor, and resonators, etc.

This dissertation employed astigmatic detection method, one of the optical measurement techniques which senses change of laser beam shape that depends on relative position between the objective lens and the target surface as the beam gets focused or out of focused. Out-of-plane resonance amplitude of the resonator is directly inferred by analyzing the shape of the laser beam incident on the detector to measure distance between lens and the target objective.

### **Astigmatic detection system**

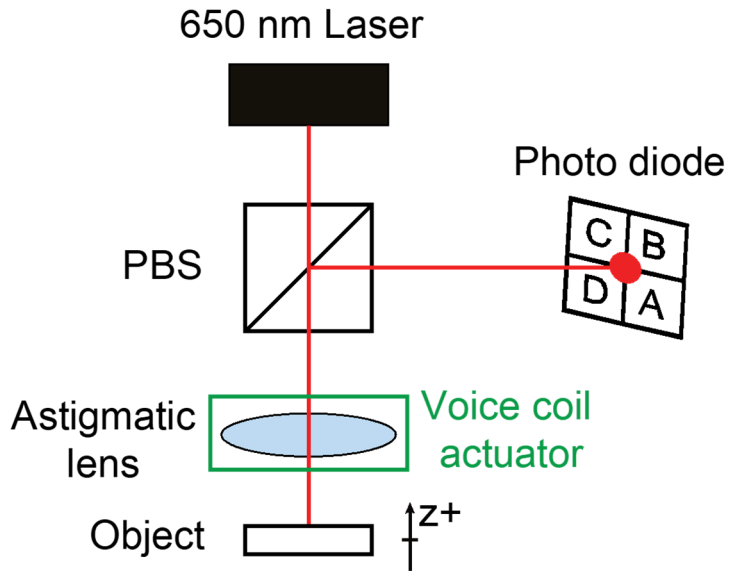
Commercial optical pickup unit (OPU) can be utilized for astigmatic detection sensor for the micro-capillary resonator. The optical configuration of the OPU

is described in Figure 4.5 (a). 650-nm laser beam from the laser diode is focused to the target surface and reflected back to the OPU through the astigmatic lens. The reflected beam pass through the beam splitter to be incident on the 4-cell photo diode. The 4cell photo diode generates currents signals and built-in transimpedance amplifier IC converts it to voltage of  $V_A$ ,  $V_B$ ,  $V_C$  and  $V_D$ , respectively. The focusing error signal (FES) is defined as  $(V_A + V_C) - (V_B + V_D)$ , and the relation of FES and the displacement follows the S-curve as showed in Figure 4.5 (b). When the laser is focused on the target object, the laser spot shape forms to be circular at the photodiode, resulting in zero FES signal. If the target object moves off the focusing plane, the beam incident on the photo diode becomes elliptical, generating either positive or negative FES signal. The sign of the FES depends on the orientation of 4-cell photodiode. The system was set up such that the FES is always within the linear regime in the S-curve for accurate measurement of amplitude resonance motion; and the FES becomes zero as the distance between the lens and the target object either gets too close or far away from their sensing region.

This OPU-based S-curve displacement detection principle can be utilized for measuring the motion of micro-capillary resonator by measuring the out-of-plane amplitude of the resonator as it oscillates in mode-split motion with rotated a certain azimuth angle (Figure 4.6).

In order to understand the resonance behavior of mode-split micro-capillary by OPU, relationship between the position of center of capillary  $(x_c, y_c)$  and the

a)



b)

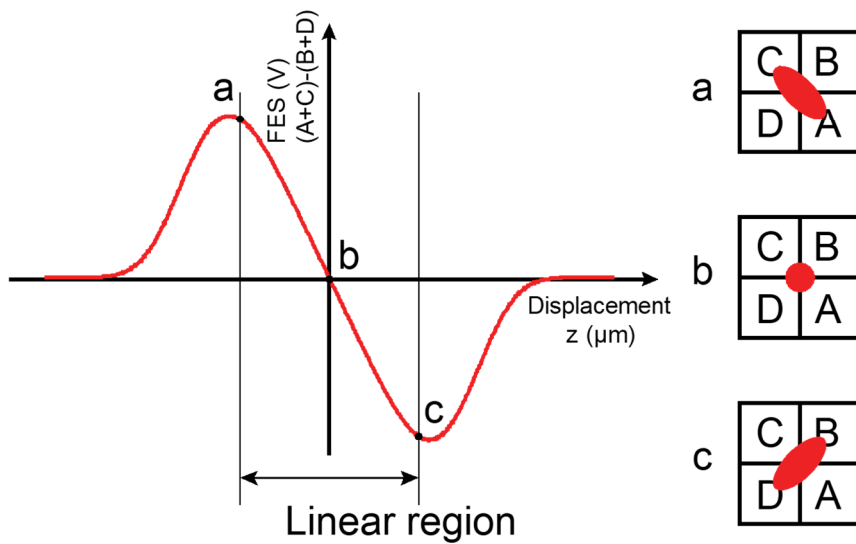


**Figure 4.5 Astigmatic detection system of OPU. (a) Optical setup of OPU. (b) The relation of FES (focusing error signal) output and the object displacement.**

position of laser spot  $(x_l, y_l)$  on the surface of the capillary was derived as follows (see Figure 4.6 graphical illustration):

$$(x_l - x_c)^2 + (y_l - y_c)^2 = \left(\frac{D}{2}\right)^2 \quad (4.4)$$

where micro-capillary is assumed to have a circular shape with an averaged diameter  $D = (D_{maj} + D_{min})/2$ . The equation was simplified by assuming the mode-split micro-capillary resonator vibrates only along the minor axis and ignoring the major axis resonance. Center position of the micro-capillary can be derived from resonance amplitude  $z_{min}(\omega)$  and the azimuth angle  $\alpha$  between the minor axis and global coordinate y-axis as follows

$$(x_c, y_c) = (-z_{min}(\omega) \cos(\alpha), z_{min}(\omega) \sin(\alpha)). \quad (4.5)$$

From equation (4.5), vertical position of the incident laser  $y_l$  is expressed as follows

$$\begin{aligned} y_l &= \sqrt{\left(\frac{D}{2}\right)^2 - (x_l - x_c)^2} + y_c \\ &= \sqrt{\left(\frac{D}{2}\right)^2 - (x_l + z_{min}(\omega) \sin(\alpha))^2} + z_{min}(\omega) \cos(\alpha) \end{aligned} \quad (4.6)$$

While being resonated along the minor axis, laser position in vertical direction ( $y_l$ ) oscillates between its maximum ( $y_{l,max}$ ) and minimum ( $y_{l,min}$ ) with an amplitude expressed as follows

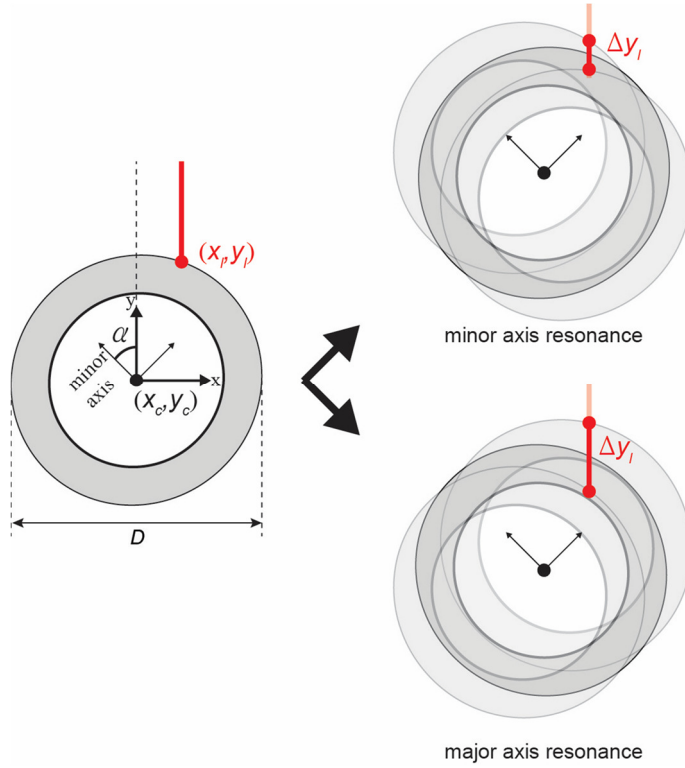


**Figure 4.6 Illustration of motion of mode-split in the elliptical cross-section resonator and incident laser spot position on the capillary surface. The two-resonance motion occurred along the major and minor axes, resulting that the vertical amplitudes of laser spot at the  $x_l$  position of the two-resonance motion showed different.**

$$\begin{aligned}
 \Delta y_l &= y_{l,\max} - y_{l,\min} & (4.7) \\
 &= 2z_{0,\min} \cos(\alpha) + \sqrt{\left(\frac{D}{2}\right)^2 - (x_l + z_{0,\min} \sin(\alpha))^2} \\
 &\quad - \sqrt{\left(\frac{D}{2}\right)^2 - (x_l - z_{0,\min} \sin(\alpha))^2}
 \end{aligned}$$

Equation (4.7) is simplified through Taylor approximation under the assumption that resonance motion amplitude  $z_{0,min}$  is negligibly small,

$$\Delta y_l \cong 2z_{0,min} \cos(\alpha) - \frac{4z_{0,min} \sin(\alpha) x_l}{\sqrt{D^2 - 4x_l^2}}, (z_{0,min} \approx 0) \quad (4.8)$$

Introducing dimensionless parameter  $\beta \equiv x_l / (\frac{D}{2})$  which divides horizontal position of the incident laser ( $x_l$ ) with the radius of the micro-capillary, equation (4.8) can be expressed as follows:

$$\Delta y_l \cong 2z_{0,min} \left( \cos(\alpha) - \sin(\alpha) \frac{\beta}{\sqrt{1 - \beta^2}} \right) \quad (4.9)$$

According to equation (4.9), oscillation along the minor axis is expressed as a function of  $z_{0,min}$ ,  $\alpha$ , and  $\beta$ . On the other hand, if the micro-capillary resonates along the major axis, oscillation amplitude in vertical direction ( $\Delta y_l$ ) is as follows

$$\Delta y_l \cong 2z_{0,maj} \left( \sin(\alpha) + \cos(\alpha) \frac{\beta}{\sqrt{1 - \beta^2}} \right) \quad (4.10)$$

It can be seen that the transformation due to azimuth angle  $\alpha$  is  $+\frac{\pi}{2}$  shifted when comparing (4.9) with (4.10). Of note, different amplitude response ( $\Delta y_l$ ) can be observed when changing the horizontal position ( $x_l$ ) of the incident laser even though the azimuth angle  $\alpha$  is consistent.

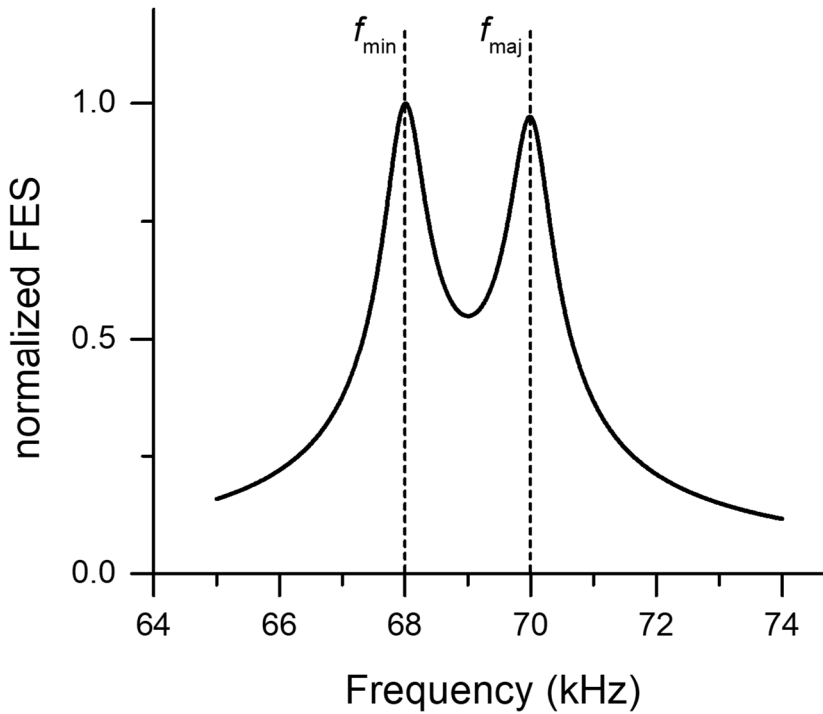


**Figure 4.7** Frequency response simulation of the mode-split resonator by measuring the astigmatic detection system. The lateral position of the incident laser spot is set to zero, and assuming the minor and major resonances have the resonance frequency of 68 and 70 kHz, respectively. the quality factor of the two resonator has 100.

Figure 4.7 shows frequency response simulation of micro-capillary resonator assuming resonance frequencies of 68 and 70 kHz for each major and minor axes, quality factor of 100, and azimuthal angle of 45 degree with the laser beam incident on the central part of the resonator ( $x_l = 0$ ).

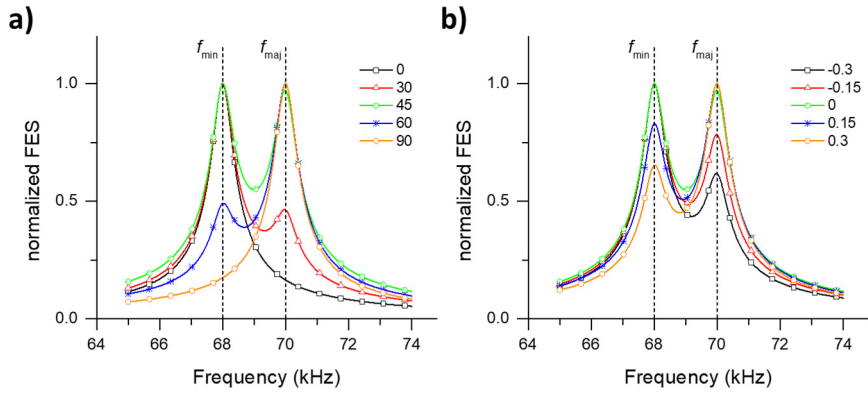


**Figure 4.8** Various frequency responses simulation of the mode-split resonator by adjusting (a) the azimuth angle  $\alpha$  and (b) the dimensionless parameter  $\beta$ . The assumption of micro-capillary resonator is same as that in Figure 4.7.

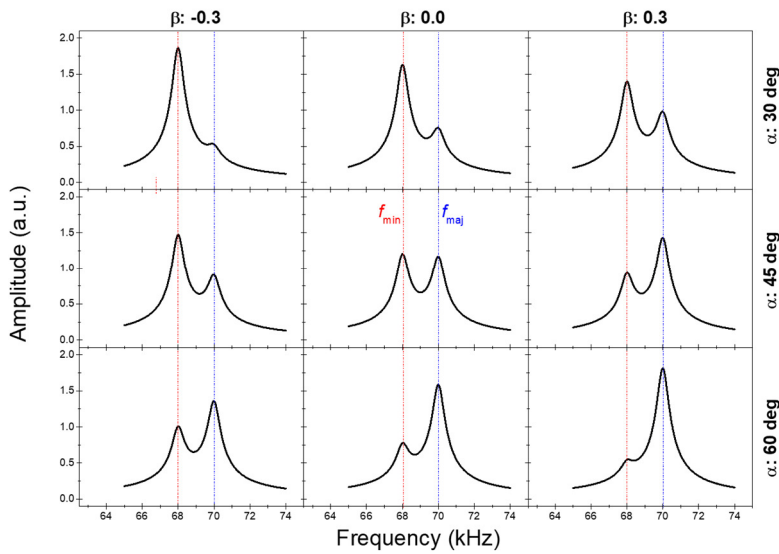


**Figure 4.9** Frequency response simulation plots for 9 combinations of azimuth angle and dimensionless lateral position of laser spot. The assumption of micro-capillary resonator is same as that in Figure 4.7.

Figure 4.8 (a) shows frequency response simulation of micro-capillary resonator when it vibrates with an azimuthal angle of  $\alpha$ . Oscillation amplitude along the major axis becomes 0 when  $\alpha = 0^\circ$ , while that along the minor axis becomes 0 when  $\alpha = 90^\circ$ . Figure 4.8 (b) shows vertical oscillatory response ( $\Delta y_l$ ) with various lateral laser position  $\beta$  when  $\alpha$  is set to be  $45^\circ$ .

Figure 4.9 shows that apparent  $|\Delta y_{l,\min}|$ ,  $|\Delta y_{l,\max}|$  measured by OPU can be changed if  $\alpha$  and  $x_l$  change even though oscillatory amplitude of micro-capillary resonator itself is consistent ( $|z_{0,\min}|$ ,  $|z_{0,\max}|$ ).

### **Digital phase locked loop (PLL)**

Multiple oscillation drivers were required for simultaneous measurements of two mode-split resonance motion of the micro-capillary resonator. FPGA (field programmable gate array) based digital PLL (phase locked loop) can be utilized for decoupling two resonance motion along the major and minor axes of the resonator since digital control system is more viable to manipulate oscillation parameters such as loop order, loop bandwidth, and gain of output amplitude in software as compared to complex and time-consuming hardware self-oscillation circuit.

The resonance signal of the resonator measured by OPU is transferred to the PLL, and response phase delay and amplitude are analyzed by phase detector and low-pass filter in the PLL. The drive output signal fed back to resonator is generated by numerically controlled oscillator (NCO) and converted to analog

sine signal by digital-to-analog converter (DAC). The digital PLL logic used in this dissertation used the code developed in [40], [41].

### **Loop bandwidth and particle speed**

Loop bandwidth of PLL device should be tuned properly for accurate tracking of resonance frequency shift during the measurement. Power spectral density (PSD) of resonance frequency of the resonator is obtained using fast Fourier transform (FFT) when particle passes through the resonator (Figure 4.10 (a), (b)) to find a frequency where cumulative PSD reaches 99%. Assuming the particle transit time of 100 ms inside the resonator, 99% PSD frequency of 17.76 Hz was set as a bandwidth for bridge-type resonator (Figure 4.10 (c)). Cantilever-type resonator under the same driving condition as that of bridge-type shows 32.52 Hz of 99% frequency, requiring higher bandwidth as compared to the bridge-type counterpart.

PLL loop filter was set to be 1<sup>st</sup>-order low-pass filter, and loop bandwidth was set to be 2 times larger than 99% PSD frequency to successfully maintain the modulated resonance frequency while particles pass through the resonator.

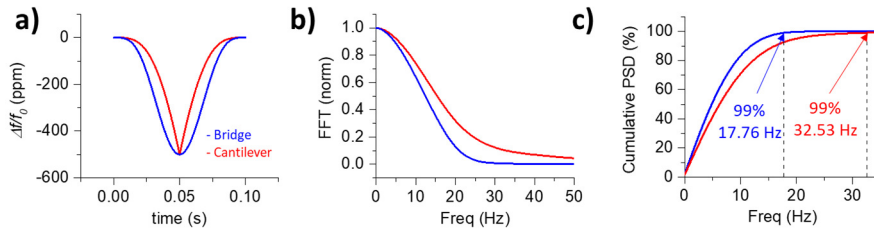


**Figure 4.10 (a) Simulation of frequency shift when a single particle passes through the bridge and cantilever type resonator. Analyzing the modulated frequency by (b) FFT and (c) cumulative power spectral density. The mass of particle is set to 0.1 % of the resonator and the transit time of particle passing through the length of the resonator is set to 100 ms.**

# **CHAPTER 5.**

## **FABRICATION AND ASSEMBLY OF MICRO-CAPILLARY RESONATOR**

### **5.1. Micro-capillary fabrication techniques**

To make microscale capillary tube, there has been a classical technique composed of a flame burner heating the glass capillary and machine-puller pulling it in opposite direction to shrink the original glass capillary. It is commercially named as a capillary puller or tapering machine that is widely used in various biological cellular probe or optical fiber research field.

Micro-capillary pulling process is composed of two steps; the first step is to heat the glass capillary, and the second is related to its pulling method. The physical properties of the glass capillary in the heat zone are shifted from the glassy state to the liquid state as the temperature rises (Figure 5.1). And the pulling process occurs when the glass capillary stays in the transition state, which exhibits the viscoelastic behaviors.

Conventionally, a flame burner has been used to heat the glass capillary. However, using flame burner has reported several problems like chemical contamination of capillary on the heating section, ambiguous heat zone boundary, and difficult heating energy control, which hinders reproducible micro-capillary fabrication [59], [70]. For this reason, electrical induction coils and CO<sub>2</sub> laser were suggested as heating devices to replace flame burners. Among them, the heating method using CO<sub>2</sub> laser was widely adopted by users

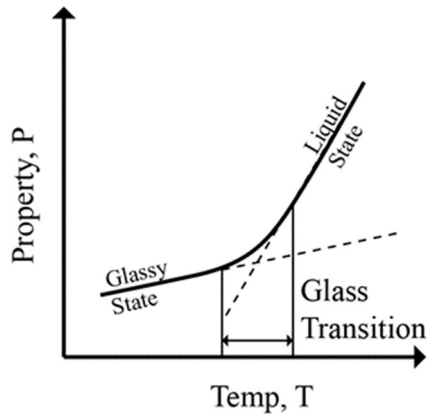


**Figure 5.1 Material properties of glass in function of the temperature. When the temperature of the glass is in glass-transition state which is between solid state and liquid state, the material properties of the glass turns into the viscoelastic property.**

since it alleviates demerits from using a flame burner and can be easily controlled by electrically.

A heated capillary in glass transition state is regarded as viscous fluid, it follows continuum fluidic mechanical principles when it is in pulling process. Mechanical pulling of the capillary is possible by pulling with constant force or pulling with constant velocity. Pulling with constant force is either using gravitational force or engaging magnetic field by setting up magnetic coil. For constant pulling velocity, a general electric motor capable of controlling the position can be used.

In this study, to fabricate a micro-capillary from a glass capillary, a commercial capillary puller (P-2000, Sutter) which consists of CO<sub>2</sub> laser heater and

magnetic coil puller is used. In addition, a custom-made capillary puller is manufactured for expanding fabrication restriction of a commercial puller. Both using a commercial and a custom-made capillary puller produced a microscale diameter of micro-capillary from 1-mm outer diameter of glass capillary.

## 5.2. Analytical modeling of taper shape of capillary

A simple mathematical model of tapering the glass fiber shape is already presented by Timothy A. Birks and Youwei W. Li in 1992 [60]. Figure 5.2 shows the nomenclature used in the model. The Timothy model assumes that the fiber in heated region is always cylindrical, has uniform temperature distribution hence the temperature relevant material properties remain equal, and ignore the complex fluid mechanics, only considers the conservation of mass (volume) during the pulling process. And the model requires the adiabatic heating process to keep the glass fiber temperature constant. Under the above constraints, the mathematical model of shape of fiber taper with constant heat zone (heated region) length, can be obtained as follows

$$r(z) = r_u e^{-\frac{z}{2L_0}} \quad (5.1)$$

where  $r_u$  is the un-tapered radius of fiber,  $L_0$  is half of a heat zone length (therefore the total heated length of fiber is  $2L_0 = 2l_w$ ). The final radius of taper waist is obtained as

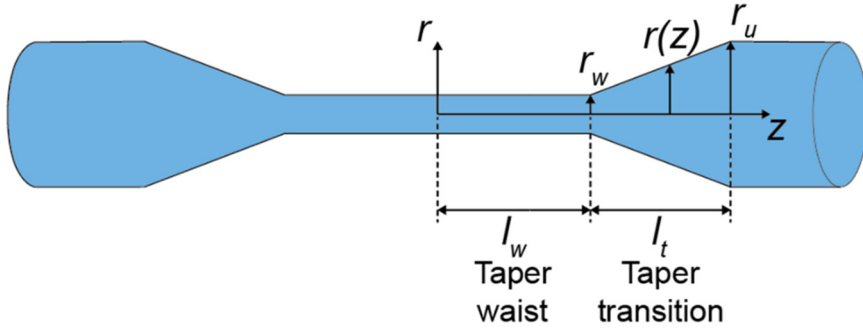


**Figure 5.2 The structure of a fiber taper and nomenclature.**

$$r_w = r_u e^{-\frac{l_t}{2L_0}} \quad (5.2)$$

where  $l_t$  is a half of total pulled length. The model can be further modified, when the heat zone length changes linearly with pulled length

$$L(x) = L_0 + \alpha x \quad (5.3)$$

where  $x$  is pulled length,  $L_0$  is the initial heat zone length,  $\alpha$  is a constant relative rate of heat zone and taper elongation length. With linear extension of heat zone during pulling process, the shape of taper fiber equation (5.1) becomes

$$r(z) = r_0 \left[ 1 + \frac{2\alpha z}{(1-\alpha)L_0} \right]^{\frac{1}{-2\alpha}} \quad (5.4)$$

The Timothy model of equation (5.1) and (5.4) can be applied to the pulling process of glass capillary, as long as the inner and outer diameter ratio is retained during the process.

A mathematical model with considering the fluid dynamics for the micro-capillary was developed by Xue *et al.* [62], [98]. This model presents the theoretical analysis on tapering micro-capillary, with taper shape, prediction of inner hole radius, and calculation the limit of fabrication time to hole collapsing. With the heat zone length  $2L_0$  and constant pulling speed  $V_0$ , assumption of properties of heated capillary as an incompressible fluid, the taper radius of pulled capillary can be obtained

$$\begin{aligned} D_o &= \chi e^{\frac{1}{2}[z-s(t)]} - \frac{s(t)}{R_0 C_a E(T_h) \dot{s}} \left( 1 - e^{\frac{1}{2}[z-s(t)]} \right) \\ D_i &= e^{\frac{1}{2}[z-s(t)]} \end{aligned} \quad (5.5)$$

where  $D_o$ ,  $D_i$  are outer and inner diameter of capillary,  $\chi$  is initial outer and inner diameter ratio,  $R_0$  is initial outer diameter,  $C_a$  is dimensionless number defined as  $\mu V_0 / \gamma$ ,  $\mu$  is viscosity of material,  $\gamma$  is surface tension coefficient.  $E(T_h)$  is dimensionless stress tensor at the pulling temperature of  $T_h$ ,  $s(t)$  is deformation length, and  $z$  is the axial distance.

The Xue model of tapering micro-capillary in equation (5.5) is more generalized than the Timothy model, as applying the fluid dynamics during the pulling process. In addition, the micro-capillary resonator requires thin wall

thickness of capillary as possible to increase the mass responsivity of the resonator, the Xue model provides an estimated limit of fabrication conditions to preventing hole collapse, regarding the pulling length and fabrication time as below

$$\begin{aligned}
 S_{limit} &= 1 + \ln \left[ 1 + \frac{\chi R_0}{s} C_\alpha E(T_h) \dot{s} \right]^2 \\
 t_{limit} &= \frac{1}{\dot{s}} \ln \left[ 1 + \frac{\chi R_0}{s} C_\alpha E(T_h) \dot{s} \right]^2
 \end{aligned} \tag{5.6}$$

The results indicate that a slow pulling velocity, the low viscosity of material (high temperature), and longer pulling distance all promote the hole collapse.

### 5.3. Custom-made capillary pulling machine

A commercial capillary puller to fabricate the micro-capillary; this machine pulled the heated capillary by electrical magnetic force coil with predefined parameters setting, pulling length and speed, is hard to adjustable. In order to fabricate the elliptical cross-section micro-capillary for achieving the mode-split resonator, a custom-made capillary pulling machine is necessary.

Figure 5.3 illustrates the fabrication process of custom-made capillary puller. The custom-made pulling machine consists of 40-W CO<sub>2</sub> laser heater and constant velocity puller by using motorized translate stage (Figure 5.3 (a)). In addition, a rotating motor was applied to the capillary to rotate the capillary to induce non-uniform temperature distribution on the cross-section of the capillary by irradiating the cyclic incident power of the laser (Figure 5.3 (b)).

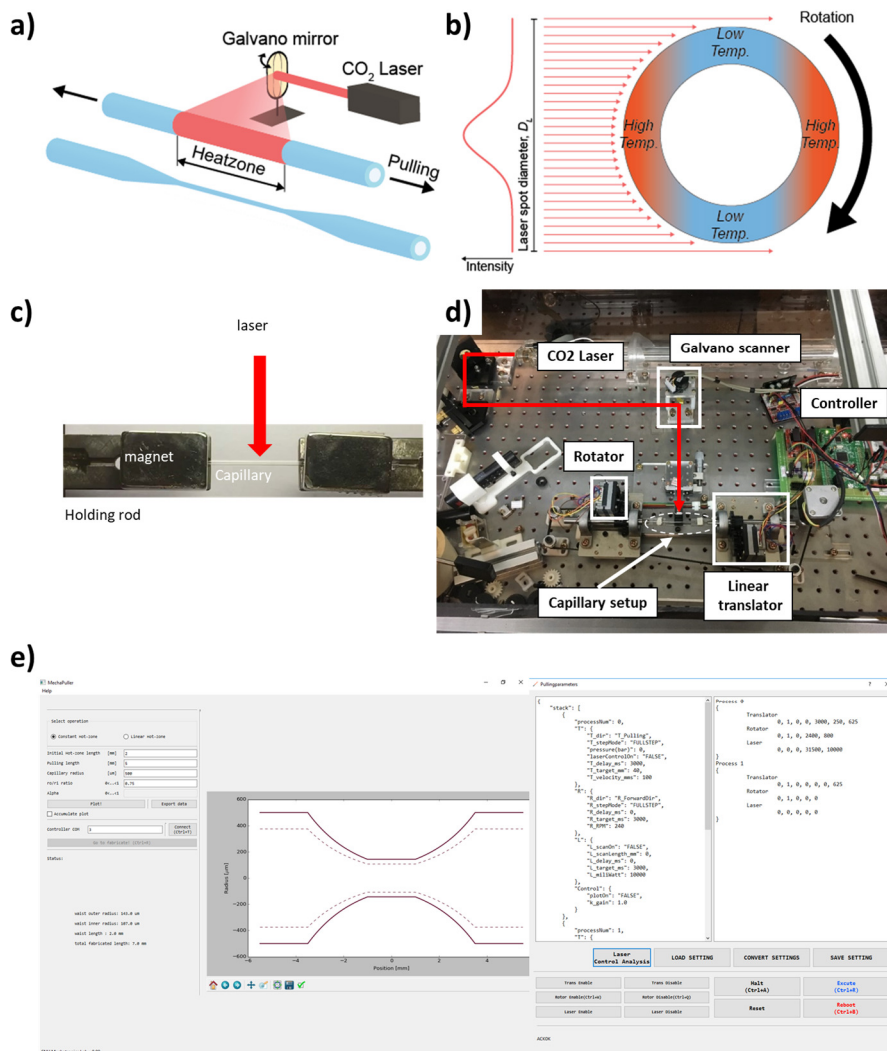


**Figure 5.3** A custom-made capillary pulling machine. (a) Illustration of the fabrication process. (b) A cyclic power of CO<sub>2</sub> laser irradiates to the capillary surface while the capillary is in the rotation to form an un-uniform temperature distribution in the cross-section of the capillary. A detail view of (c) capillary setup and (d) photograph of manufactured device. (e) GUI software to control the overall fabrication process.

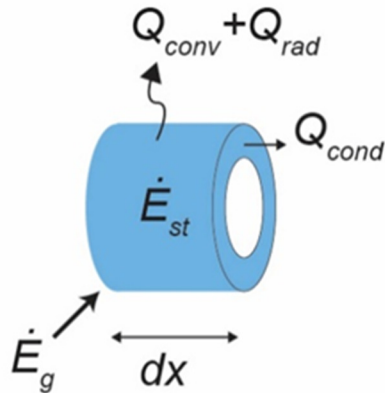


**Figure 5.4 Heat transfer modeling of glass capillary**

For manufacturing the custom-made capillary puller, two general step motors (step angle of 1.8 degree) is set to the rotator to rotate the capillary holding rod (Figure 5.3 (c) and (d)) and one step motor is set to the linear translator (Figure 5.3 (d)) for pulling the capillary with constant speed, a Galvano mirror vibrates the reflection mirror to adjust the CO<sub>2</sub> laser beam scan length horizontally to define a heat zone. A capillary was positioned to be concentric with the holding rod and fixed with a magnet (Figure 5.3 (c)). A 32bit ARM Cortex-m series micro controller (STM32F401 Evaluation board, STM) controlled the all actuator components and laser power by using a real-time operating system (FreeRTOS software, Amazon). Overall fabrication process controlled by graphical user interfaces (Figure 5.3 (e)).

For analyzing the capillary heating by CO<sub>2</sub> laser, a simple heat balance equation is employed to estimate the optimal laser power to fabricate the micro-capillary

(See Figure 5.4). A mathematical heat balance equation during the CO<sub>2</sub> laser heating process of the capillary is below

$$\dot{E}_g = \dot{E}_{st} + Q_{rad} + Q_{conv} + Q_{cond} \quad (5.7)$$

$$\dot{E}_{st} = \rho c V \frac{\partial T}{\partial t} = \rho c 2\pi r^2 (1 - \chi^2) dx \frac{\partial T}{\partial t} \text{ (Stored energy)}$$

$$Q_{rad} = \epsilon \sigma A (T^4 - T_\infty^4) = \epsilon \sigma 2\pi r dx (T^4 - T_\infty^4) \text{ (Radiation)}$$

$$Q_{conv} = HA(T - T_\infty) = H 2\pi r dx (T - T_\infty) \text{ (Convection)}$$

$$Q_{cond} = k \nabla T|_x \text{ (Conduction)}$$

where  $\dot{E}_g$  is generated energy of capillary by irradiated laser power. In the preceding equations,  $\rho$  is density,  $c$  is specific heat,  $V$  is volume,  $r$  is radius,  $\chi$  is inner and outer diameter ratio,  $\epsilon$  is radiation coefficient,  $\sigma$  is radiation constant,  $H$  is convection coefficient,  $A$  is surface area,  $k$  is conduction coefficient, and  $T$  and  $T_\infty$  are the material and ambient temperature, respectively. In practical, the conduction heat loss of heated capillary which occurs only at the boundary of the heat zone is negligible, so that the laser energy absorbed into the capillary is used to increase its internal temperature after subtracting the convection and the radiation loss only. The power distribution of the CO<sub>2</sub> laser is assumed to be Gaussian, the total absorbed power  $W_{abs}$  by the capillary can be calculated [70]

$$W_{abs} = 2rwQ_{abs} \frac{P_{laser}}{\pi w^2} \operatorname{erf}\left(\frac{2r}{\sqrt{2}w}\right) e^{-2} \quad (5.8)$$

where  $P_{laser}$  is laser output power,  $Q_{abs}$  is absorption coefficient of capillary,  $w$  is beam radius and  $r$  is capillary radius.

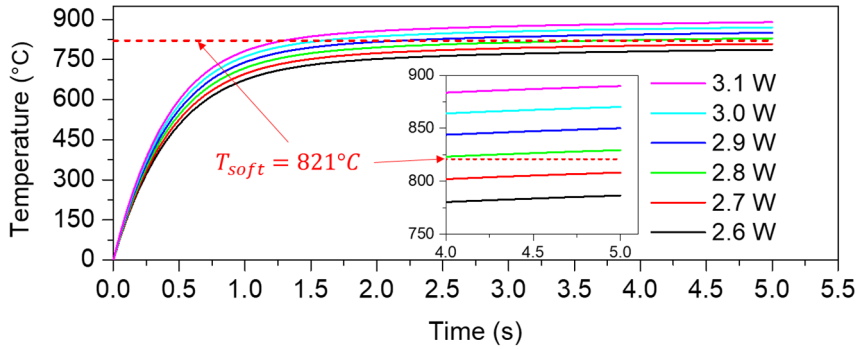


**Figure 5.5 Simulation results of temperature of glass capillary as a function of heating time. With the assumption of that the laser beam diameter is 2.5 mm, radius of the capillary is 0.5 mm, heat zone length is 2 mm.**

For acquiring the optimal laser power and heating time to make the glass capillary to be in glass-transition state, simulation of laser heating of 1-mm outer diameter of borosilicate glass capillary with an inner and outer diameter ratio of 0.7 is conducted by using SciPy and Python script. The physical parameters of the borosilicate glass are adopted from Ref [107]. In the simulation, the absorption coefficient  $Q_{abs}$  is set to 1 and the scattering power loss effect of laser beam in the capillary material is ignored [70], [108], [109]. And temperature distribution of the heated capillary in the heat zone is assumed to the uniform.

With the assumption of the laser beam diameter of 2.5 mm, the capillary diameter of 1 mm, heat zone length of 2 mm was set simulation parameters. Figure 5.5 shows the simulation results. The time required to reach the

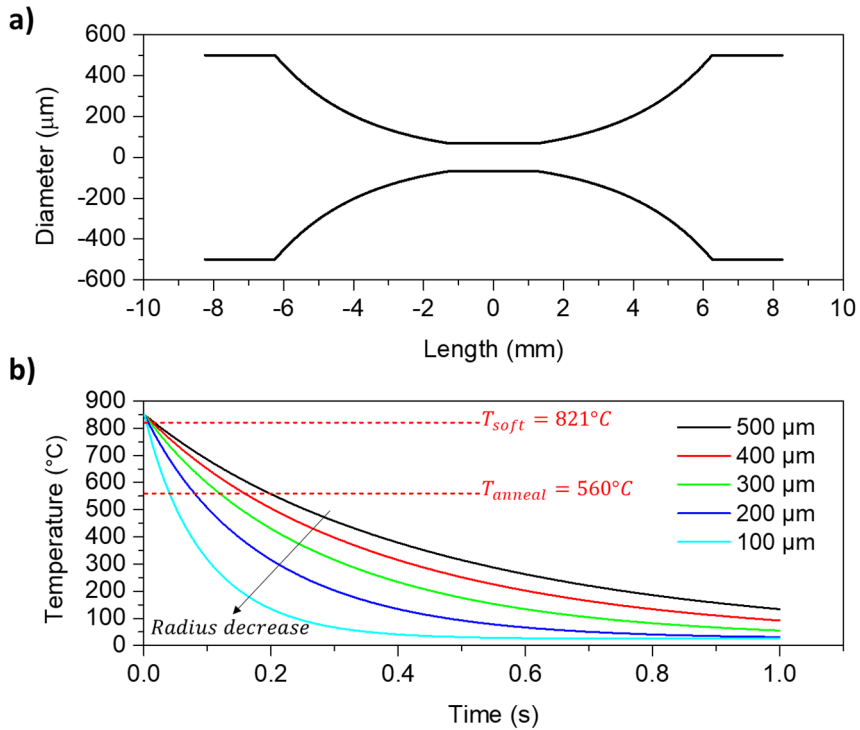


**Figure 5.6 Simulation of cooling time estimation of heated glass capillary. The capillary in the tapered region (a) shows different cooling times (b) depending on the size of the diameter.**

softening temperature  $T_{soft}$  of borosilicate glass capillary was estimated to be about 1.5 to 5 seconds when the laser power is range from 2.7 to 3.1 W.

Next, the limit of pulling process time before glass cooled down to the glassy state is conducted. In the pulling process, the laser is off powered so that the stored heat energy is continuously released to convection and radiation of capillary (See equation (5.7)). Once the glass capillary reaches the softening

point that the capillary is soft enough to deformation, it was assumed that the pulling process begins immediately. Figure 5.6 shows the cooling time curves for various diameters of the glass capillary in the tapered area. Since the convection and radiation energy losses are functions that depend on the diameter of the capillary, the available pulling time of the capillary is varied for each tapering location.

## **5.4. Fabrication results**

### **Micro-capillary fabricated by commercial puller**

To fabricate microscale diameter of capillary, a borosilicate glass capillary of which inner and outer diameters are 0.58 and 1.00 mm, respectively (1B100-F-3, World Precision Instruments) is fabricated by commercial capillary puller (P-2000, Sutter) (Figure 5.7 (i)). The laser heated capillary puller defines the micro-capillary while maintaining the cross-sectional area of both ends (Figure 5.7 (ii)). Once the glass capillary was pulled, it was flexible enough to be bent 180 degree and make a U-shaped loop (Figure 5.7 (iii)). Inner and outer diameters of the pulled section of the capillary can be varied by adjusting parameters such as laser power and pulling force of the puller machine. The smallest and largest inner diameters of the pulled section were 14 and 148  $\mu\text{m}$ , respectively, while the ratio of inner to outer diameter of the pulled section was  $\sim 0.623$  which is similar to the initial ratio of 0.58 (Figure 5.7 (iv)).

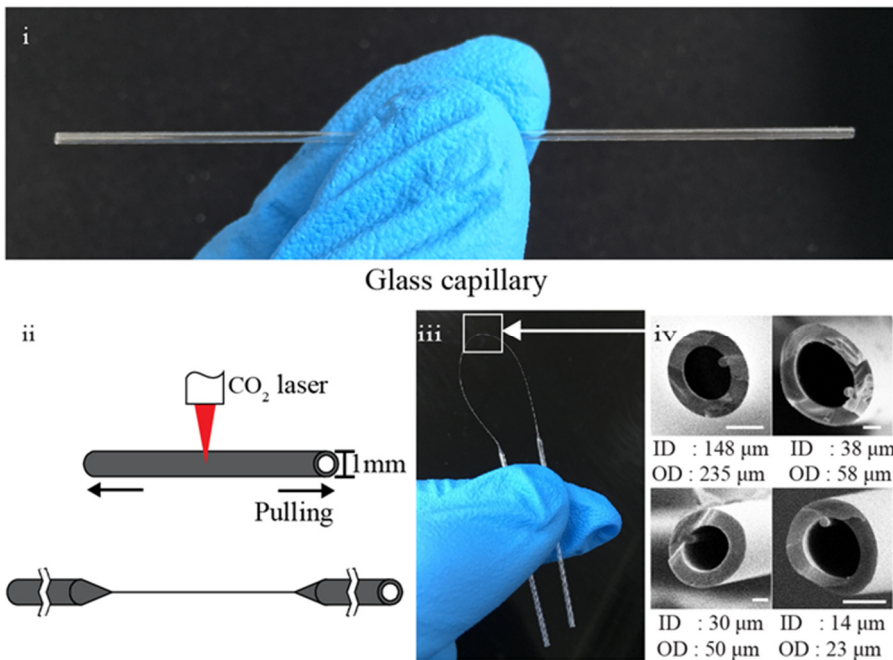


**Figure 5.7** A picture of borosilicate glass capillary (i). Schematic showing the capillary pulling to decrease the inner and outer diameters around the middle section of the capillary (ii). A pulled capillary (iii). Scanning electron microscope images of cross-section areas of pulled capillaries with various inner and outer diameters. Scale bars are 100, 10, 10, and 10  $\mu\text{m}$ , respectively (iv).

### Micro-capillary fabricated by custom-made puller

The CO<sub>2</sub> laser power is set to 3 Watt and heat the borosilicate glass capillary (TW100-6, World Precision Instruments) in 4 seconds. The laser beam diameter is focused to ~2 mm at the capillary surface by ZnSe coated objective lens. The heat zone length of capillary is set to 2 mm. the rotational speed of heated capillary is set to 180 rpm. After heating of capillary, pulling process is

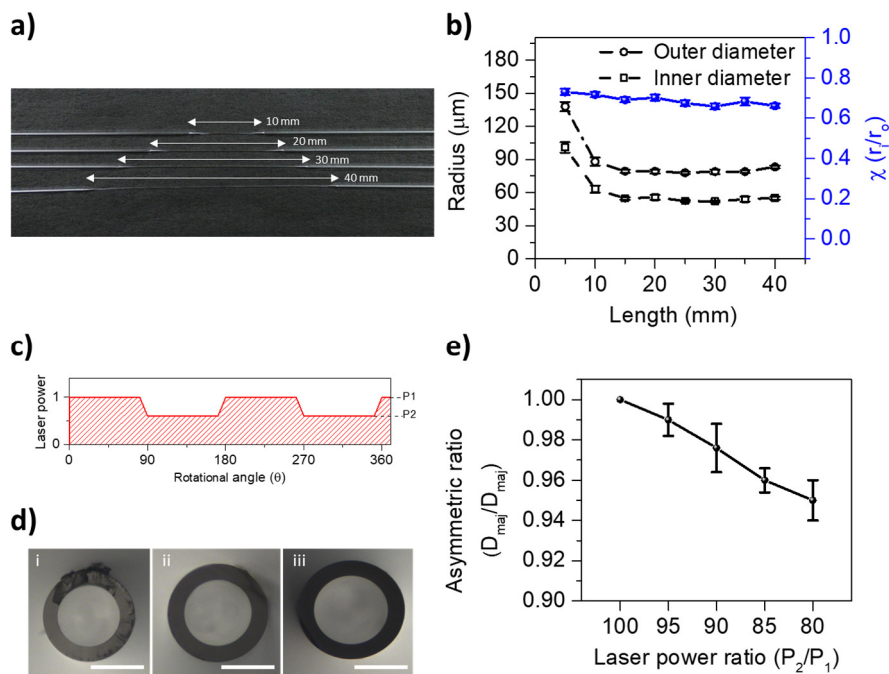


**Figure 5.8(a) Photographs of pulled micro-capillary and (b) plot of their outer diameter at the middle. (c) Laser power variation with respect to the rotational angle. (d) Several photographs of elliptical cross-section of pulled micro-capillary ((i) Perfectly symmetric, asymmetric ratio ( $D_{\text{minor}}/D_{\text{major}}$ ) of (ii) 0.97 and (iii) 0.93). Scale bars are 100  $\mu\text{m}$ . (e) Asymmetric ratios of pulled micro-capillaries as a function of rotational laser power ratio of low power of P2 divided by high power P1.**

conducted with constant pulling velocity of 100 mm/s. Various pulling distance is tested, the micro-capillary outer and inner diameter results are plotted in Figure 5.8 (a) and (b). At the middle of pulled micro-capillary range from 10 to 40 mm the diameters are hardly changed. It is analyzed that the fabrication time of pulled micro-capillary length over than 10 mm exceeds 0.1s, the diameter of

micro-capillary at the middle is already cooled down so that no more pulling process is performed. Instead, it is understood that taper transition part of capillary is still in pulling process that makes the capillary extended.

To fabricate an asymmetric cross-section micro-capillary, the laser power is adjusted according to the rotational speed to bring the un-uniform temperature distribution in the heated capillary (Figure 5.8 (c)). The laser power was adjusted according to 1/4 of the rotation period. Although the laser power is varied by the rotation period, the time averaged laser power is maintained to be 3 W. Figure 5.8 (d) shows the photographs of asymmetric cross-section of pulled micro-capillary and (e) plot of their asymmetric ratios as a function of the adjusted laser power.

### **Wall thickness tuning**

The wall thickness of the fabricated micro-capillary can be decreased to improve the mass responsivity performance for using it as a mass sensing resonator. Flexible nature of a pulled micro-capillary enables the selective etching of its exterior by dipping the pulled region into a hydrofluoric acid (HF) bath with the micro-capillary bent 180 degree. After short period dwell in HF, the micro-capillary was taken out, washed in DI water, and dried (Figure 5.9 (a)). Scanning electron micrographs show the cross-sections of the micro-capillary before and after the selective etching process. Wall thicknesses

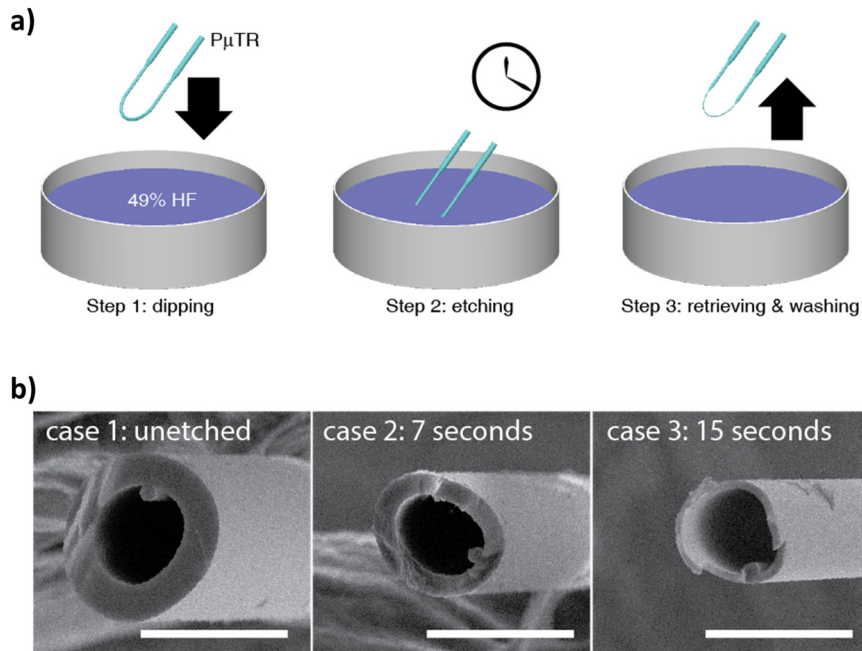


**Figure 5.9 (a) Selective etching process of the micro-capillary. (b) Scanning electron micrographs of micro-capillaries before and after the selective etching. All scale bars are 50  $\mu\text{m}$ .**

of the micro-capillary were decreased by 4 and 9  $\mu\text{m}$  after 7 and 15 second etching, respectively, while their inner diameters were maintained (Figure 5.9 (b)).

In the other way, increasing the area ratio of the inner channel to the wall of micro-capillary is possible when applying the pressure at the inner channel of the capillary during in pulling process. Inner pressure is applied to the capillary by the pressure controller (ITV-0030, SMC) connected to the one end of the capillary via typical silicon tube, while the other end of the capillary is closed by epoxy bond. Using the custom-made capillary puller, the capillary was

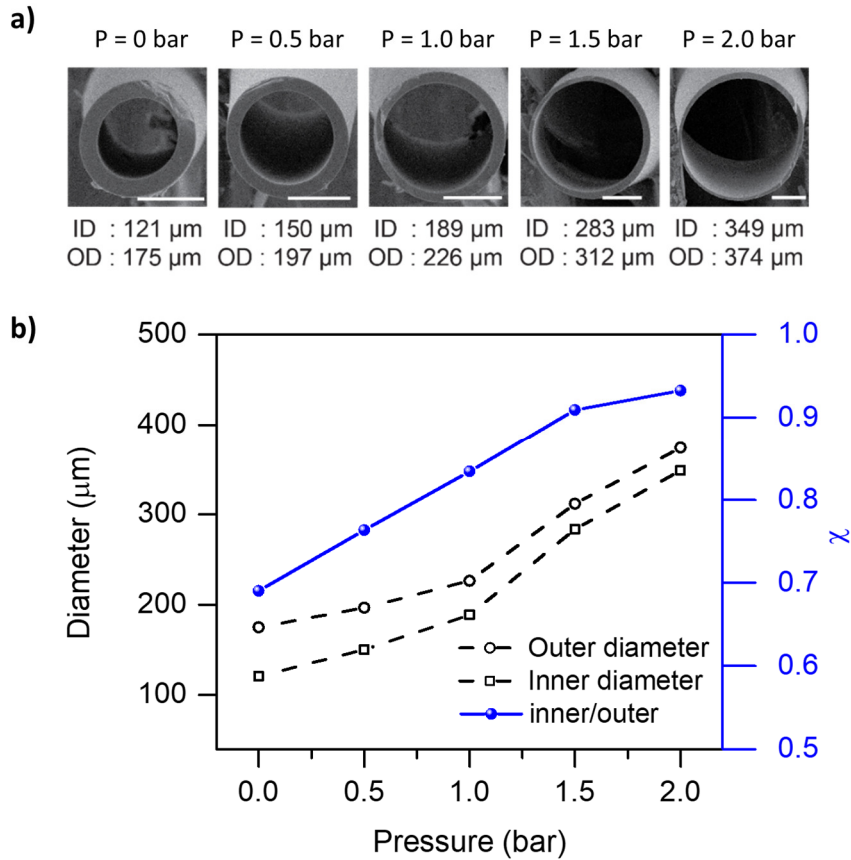


**Figure 5.10 (a) Scanning electron micrographs of micro-capillaries with various inner pressure applied during the pulling process, and (b) the plot of the inner and outer diameter of the fabricated micro-capillaries.**

heated during 6 seconds with the laser power 2.9 W. Then, the heated section of the capillary was pulled with 100 mm/s velocity, rotation speed of 240 rpm, and pulled to 30 mm. During the pulling process, inner pressure was applied.

Figure 5.10 (a) shows the result of inner pressure experiment of the cross-section of the micro-capillaries. Due to the inflation of the micro-capillary by

the inner pressure, both of inner and outer diameters of the micro-capillary were increased. The area ratio of the pulled micro-capillary was increased up to 0.93 when the inner pressure is 2.0 bar (Figure 5.10 (b)).

## **5.5. Resonator assembly**

For manufacturing micro-capillary to a resonator as a mass sensor, the two types of resonators were made; the one is string type resonator with piezoelectric readout, and the other is bridge type resonator with astigmatic detection readout. The two types of resonators were simply assembled using the pulled micro-capillary, boundary clamps made by aluminum block, and epoxy bonds only. The fabrication cost is under \$10 and the assembly time is in 2 hours maximum, which is far superior than that of MEMS which requires about \$100,000 and over a month duration with cleanroom facility.

### **String type micro-capillary resonator with QTF**

To realize the string type micro-capillary resonator, parts were assembled by following the procedures in Figure 5.11 (a). First, 0.3 *N* of axial tension was applied to a pulled micro-capillary using a tension gauge (110g, OHBA SIKI) to remove slacks and also increase the resonance frequency and amplitude of the resonator. With applied tension maintained, the pulled micro-capillary was brought over and attached to a custom-made aluminum jig with epoxy bond.

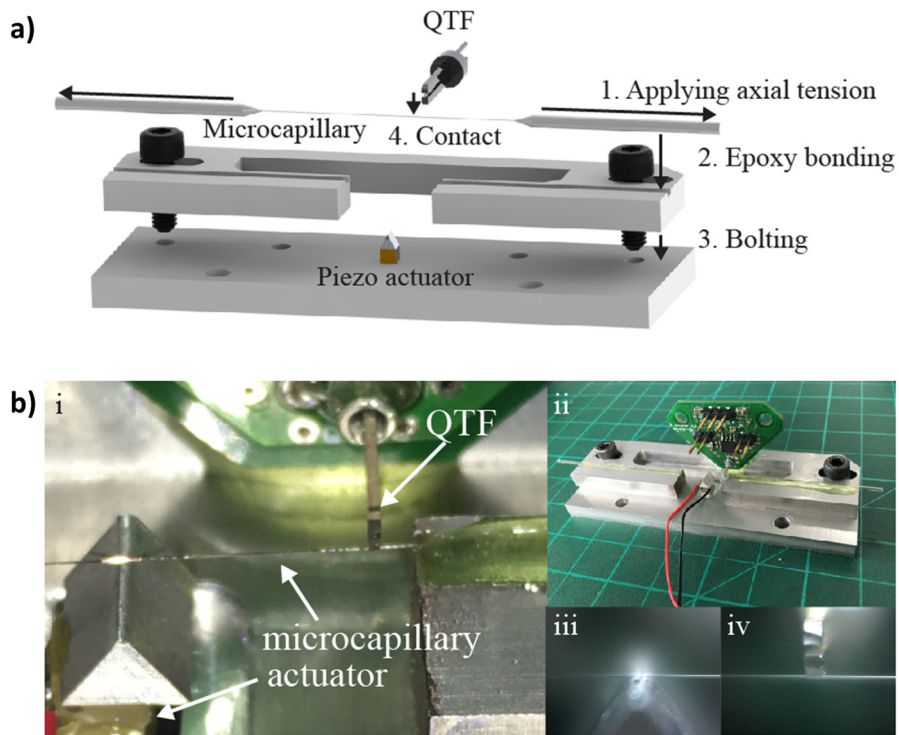


**Figure 5.11 (a) Assembly process of string type micro-capillary resonator with piezoelectric readout system. (b) Photographs of an assembled resonator system.**

Then, the jig holding the attached micro-capillary was fixed to a base block having a nodal block on piezo actuator (TA0505D024W, Thorlabs) with two standard M4 bolts. After this step, the pulled micro-capillary made a solid contact with the actuation node. Finally, using a motorized stage (MTS25-Z8, Thorlabs), the 32.768 kHz QTF (AB26T-32.768 kHz, Abracon) mounted on a transimpedance amplifier (TIA) board (Note: a detail description of functionality and hardware of QTF TIA board are in Chapter 6.2) approached precisely with a 10- $\mu$ m step towards the pulled micro-capillary and made

another solid contact which defined the sensing node. Finally, the TIA board was bonded to the jig assembly by using the epoxy bond. Figure 5.11 (b) shows several pictures of the final string type micro-capillary resonator with piezoelectric readout system. The typical settings for the length was 6.5 mm, outer and inner diameters were 50, 30  $\mu\text{m}$ , respectively, throughout in this dissertation unless otherwise stated.

### **Bridge type micro-capillary resonator with OPU**

To make bridge type micro-capillary resonator, a part of micro-pipette capillary was used (process 1-3 in Figure 5.12). The pulled micro-capillary was broken into two pipettes using a razor blade (process 3 in Figure 5.12). After, one of the micro-pipette capillaries was laid on the pre-defined trench (4 mm) as a resonance section of the aluminum block and was covered by the pair of another aluminum block (process 4 in Figure 5.12). The exposed upper surface of capillary in resonator section is gold coated using general sputter machine (process 5 in Figure 5.12). Then, for preventing air disturbance and protecting the resonator, a thin (0.1 mm) glass is covered on to the upper hole (process 6 in Figure 5.12).

After the fabrication process of bridge type micro-capillary resonator is completed, an astigmatic detection readout system using OPU was integrated. Figure 5.13 (a) shows the assembly drawing of the bridge type micro-capillary resonator with OPU readout system (Note: a detail description of the overall functionality and hardware of OPU readout system are in Chapter 6.2). The distance between the OPU and the surface of the resonator was set to the focus

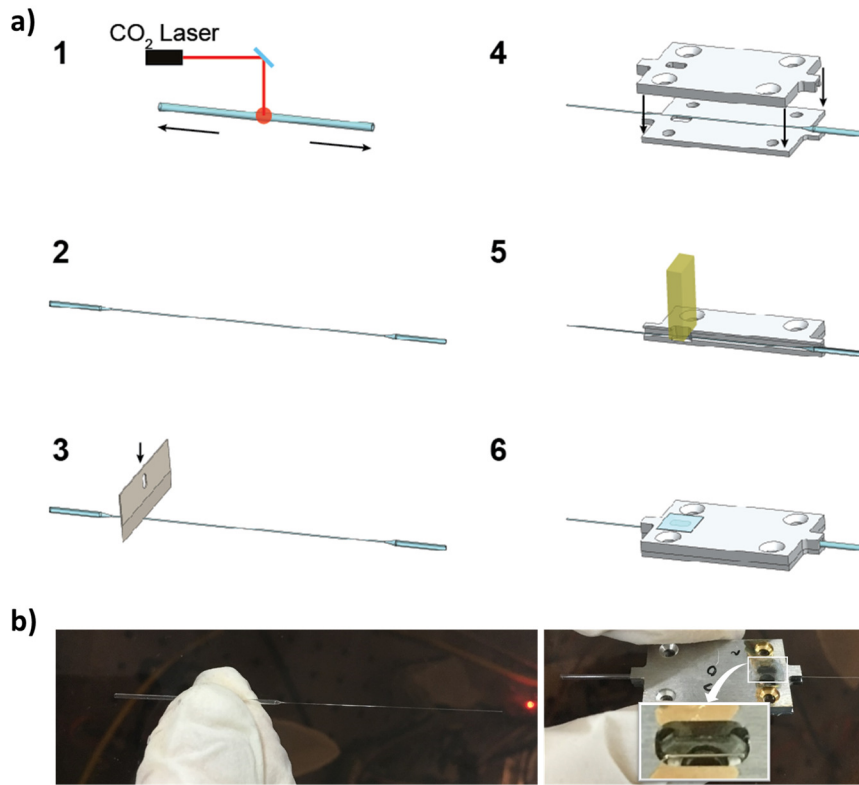


**Figure 5.12 Fabrication process of bridge type micro-capillary resonator block. (a) Laser heating and pulling process to form a microscale capillary (1 and 2). A razor blade cuts the micro-capillary section to make micro-pipette capillary (3). A 4-mm trench of aluminum block is bonded to the micro-pipette capillary and the pair of aluminum block is covering on it (4). Gold is coated on the capillary surface by general sputter machine (5). A thin (0.1 mm) glass is covered the resonator to prevent external scratch and air perturbation to the resonator (6). (b) Photographs of the actual products at the manufacturing process 3 and 6.**

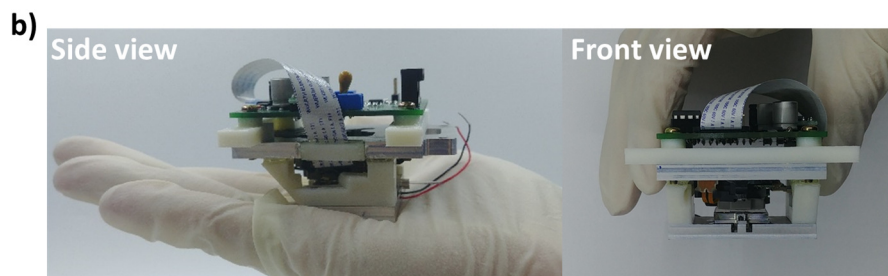
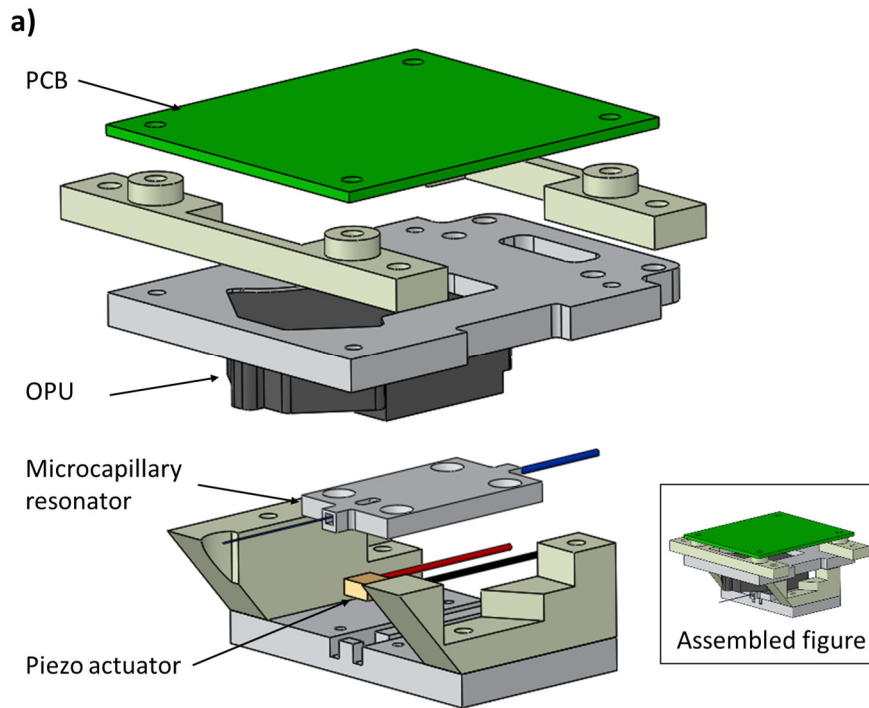


**Figure 5.13 (a) Assembly view of bridge type micro-capillary resonator with OPU readout system and (b) its assembled picture.**

distance of the astigmatic lens of the OPU by manipulating the XYZ stage during the assembly. The OPU readout system and micro-capillary resonator block were fixed by epoxy bond. Finally, a portable size of bridge type micro-

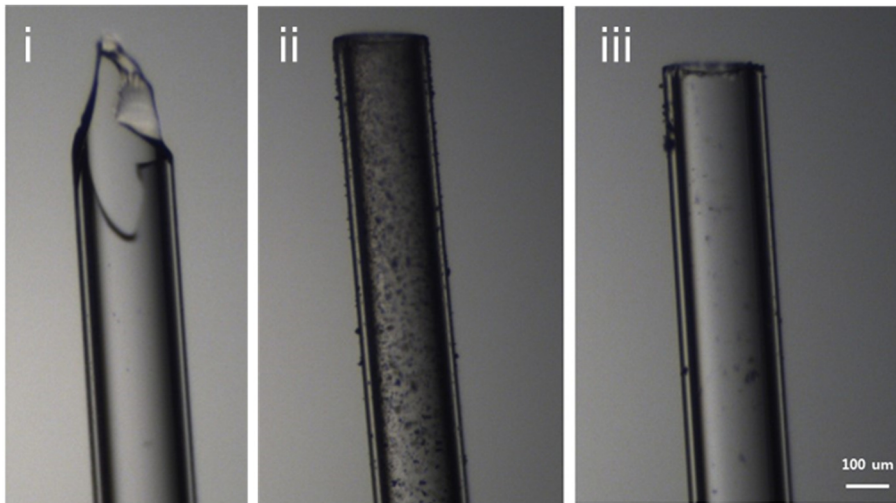


**Figure 5.14 Beveling micro-capillary tip. (i) A sharp edge at the tip of the micro-capillary is beveled by rotating sandpaper with 30 seconds with 600 rpm. After beveling, (ii) glass chips stick to the capillary surface and (iii) the tip is cleaned after ultrasonication.**

capillary resonator integrated with OPU readout system was ready (Figure 5.13 (b)). The typical settings for the length was  $\sim 4$  mm, outer and inner diameters were range from  $150 \sim 220$ ,  $90 \sim 120$   $\mu\text{m}$ , respectively, throughout in this dissertation unless otherwise stated.

An additional beveling procedure can be applied to the micro-capillary tip for smoothing its sharp edge. Figure 5.14 shows the micro-capillary tip beveling process by the 30-second scrapping at a sandpaper pasted on a disk rotating at 600 rpm.

# CHAPTER 6.

## EXPERIMENTAL SETUP

To measure a mass of sample fluid or particle using the micro-capillary resonator, target analytes should be transported to mass sensing region inside of the resonator. In this chapter, the fluid pressure control systems are prepared to deliver a sample fluid to the resonator. In addition, two electrical oscillator system configurations to drive the micro-capillary resonator and the configuration of auxiliary systems are described.

### 6.1. Fluidic control system

Fluid pressure control system can be constructed to allow mass transport to the fluid channels inside micro-capillary. In conventional MEMS resonator based on the silicon wafer, additional chemical etching process is required to connect the inside embedded channel of the resonator to an exterior wafer surface for fluidic connection [13], [15], [33]. Once the fluidic channel is exposed, Teflon tube is connected to the hole, in turns, wrapped with an O-ring to be clamped to form a fluid connection, which is overall complicated procedure.

However, in case of the proposed micro-capillary resonator, unpulled sections at both ends facilitate interfacing with standard fluidic component connection. In order to connect Teflon FEP tube with outer diameter of 1/16'' to micro-

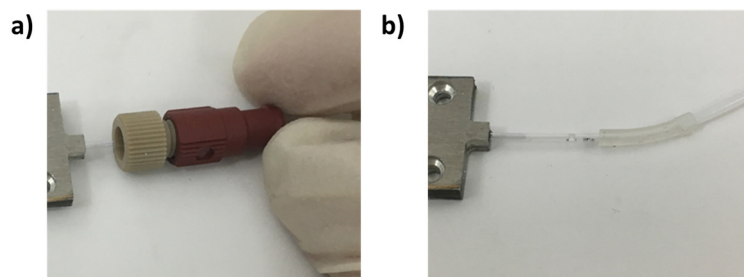


**Figure 6.1** Photographs of fitting of a FEP tube to the capillary by using (a) commercial tubing connector and (b) silicon tube.

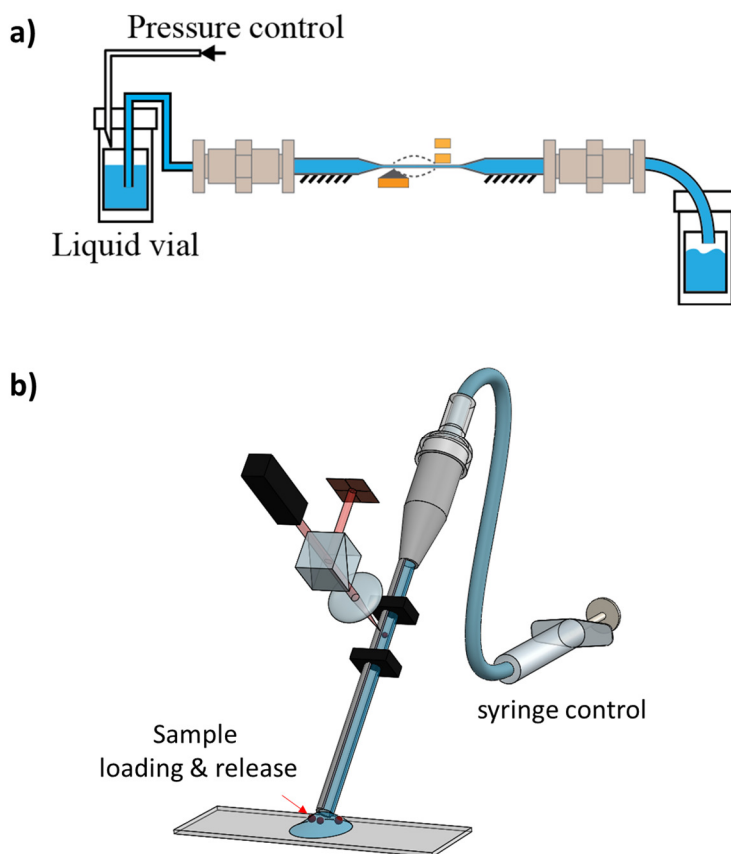


**Figure 6.2** Two types of fluidic setup to deliver liquid sample into the resonator by using (a) the pressurizable vial with pressure controller and

**(b) syringe controller.**

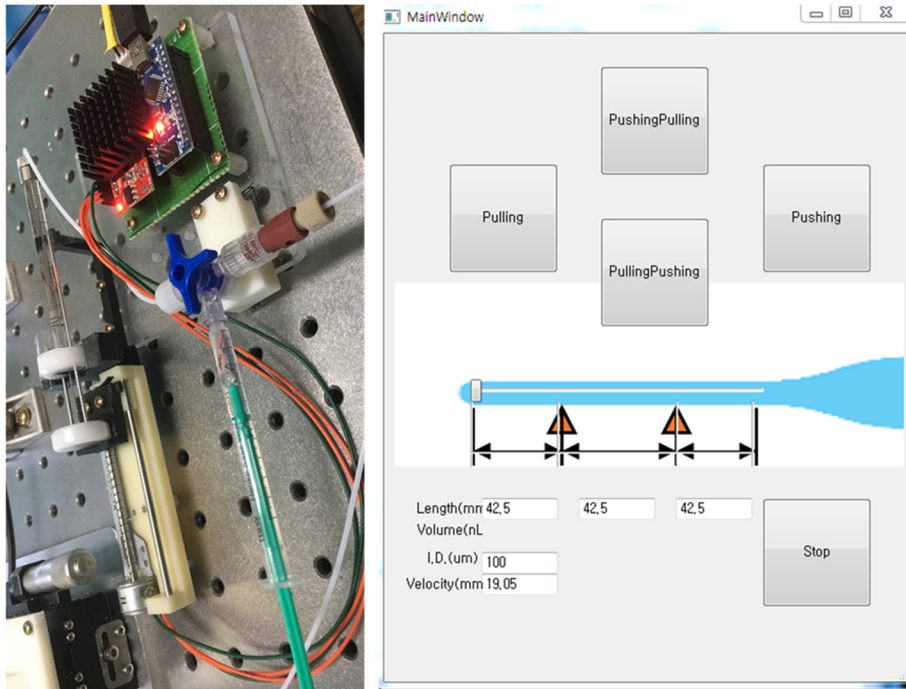


**Figure 6.3 Photograph of custom-made syringe controller using step motor and microcontroller. And the GUI software to control the syringe.**

capillary with outer diameter of 1-mm, general fluidic connector or silicon tube (O.D.: 2 mm, I.D: 0.6 mm) is used (Figure 6.1). Connected Teflon tube is then connected with pressurizable vial where pressure controller (ITV-0030, SMC) injects fluid into the resonator (Figure 6.2 (a)).

Another way to connect the fluid system to micro-capillary is presented in Figure 6.2 (b) when the shape micro-capillary resonator is a micro-pipette. In this configuration, a syringe is connected to the resonator to control loading and release of fluid and sample particles instead of a pressure vial. A microscopic

camera can be installed at the pipette tip to monitor the target particles entering the resonator. To this end, this enables selective massing detection by injecting the desired particles into the resonator. In addition, since the distance from capillary inlet to resonator section is short to minimize transport length, problems clogging of heavy particles due to the long and complex tubing setup can be prevented.

Figure 6.3 shows a syringe controller composed of a stepper motor and a microcontroller (UNO, Arduino). Syringes (1701 RN SYR series, Hamilton) with volume of 10  $\mu\text{L}$  and 100  $\mu\text{L}$  are used, and the syringe pistons are controlled using Python code on the PC.

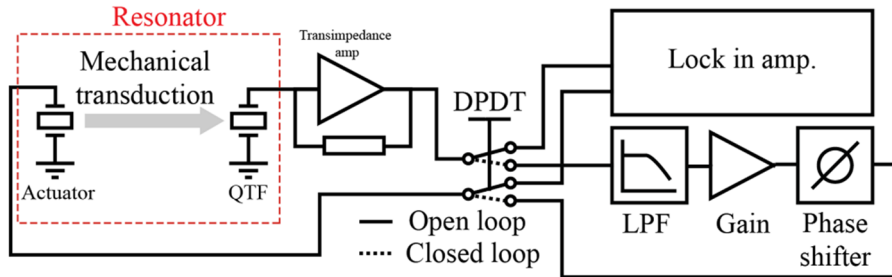
## **6.2. Readout and oscillator system implementation**

### **System 1: QTF and self-oscillation circuit**

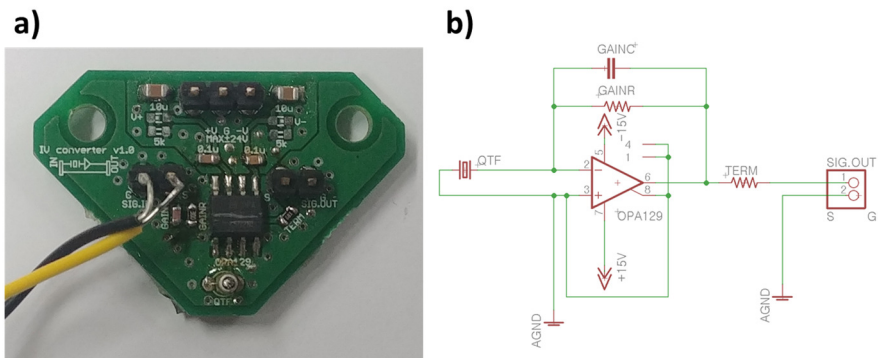
Figure 6.4 illustrates the electrical configuration of the system. The QTF and self-oscillation circuit system can be operated in either open or closed loop modes.

Figure 6.5 shows printed circuit board(PCB) of the QTF and transimpedance amplifier(TIA) circuit used in this dissertation. A transimpedance amplifier was configured using an operational amplifier (OPA129, Texas Instruments) with 1  $\text{M}\Omega$  gain resistor. It is important to set a bandwidth of TIA to ensure the signal generated from the micro-capillary motion is successfully transmitted without gain loss. The key elements of the limiting bandwidth of the TIA are the QTF

capacitance, desired transimpedance gain resistor, the GBP (gain bandwidth product) of the TIA and the feedback



**Figure 6.4** Open and closed loop drive circuits for the micro-capillary resonator system.



**Figure 6.5** (a) Printed circuit board of transimpedance amplifier and (b) its electrical schematic.

capacitance. According to the manufacturer datasheet, the GBP of the OPA129 is 1 MHz. To achieve a 2<sup>nd</sup> order Butterworth frequency response, set the feedback pole by

$$\frac{1}{2\pi R_f C_f} = \sqrt{\frac{GBP}{4\pi R_f C_q}} \quad (6.1)$$

where  $R_f$  is the feedback resistance,  $C_f$  is the feedback capacitor and  $C_q$  is the load capacitance of the QTF. Applying 12.5 pF of the load capacitance of the QTF (AB15T, Abracon) with 1- M $\Omega$  gain value, the feedback capacitance can be obtained to ~2 pF and the -3dB bandwidth of the given TIA system is ~113 kHz according to the equation below

$$f_{3dB} = \sqrt{\frac{GBP}{2\pi R_f C_q}} \quad (6.2)$$

The common-mode capacitance, differential mode capacitance and the rest of the other parasitic capacitance values are ignored to achieve above approximate results.

In the open loop mode, a function generator drives the piezo actuator at the actuation node near the resonance frequency of the resonator while the transduced vibration of the resonator at the sensing node is measured with a lock-in amplifier (Model 7265, Signal Recovery) through the transimpedance amplifier.

In the closed loop mode, Figure 6.6 (a) describes the self-oscillation circuit design and the PCB board (b) used in this dissertation. The output signal from the TIA is low-pass filtered, amplified, phase adjusted and fed back to the external actuator of the micro-capillary with amplifying the power by current buffer amplifier (LT1210, Linear Technology) for increasing the driving capability to capacitance load. The low-pass filter used is a second-order active

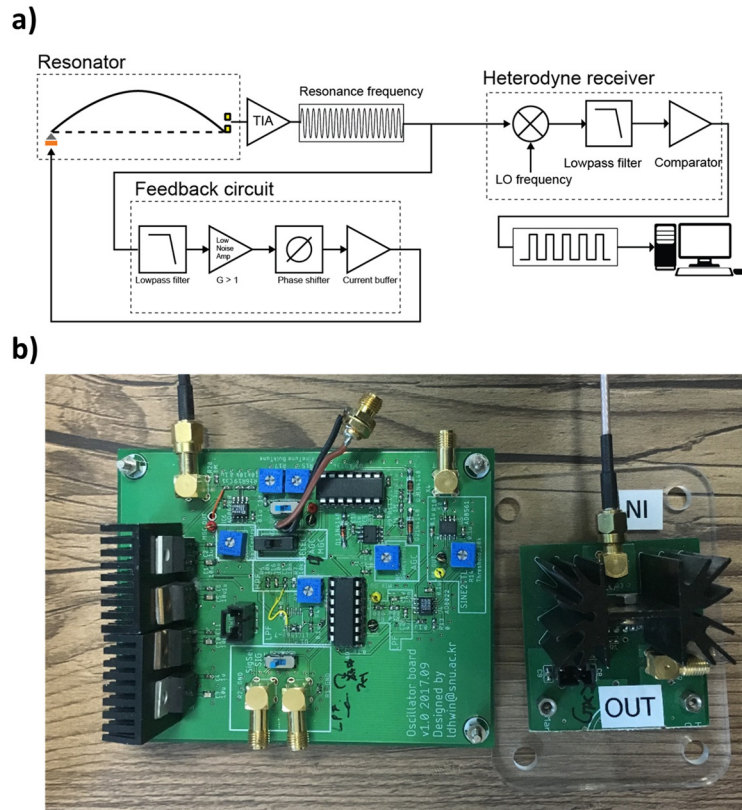


**Figure 6.6 (a) Diagram of driver unit of micro-capillary resonator and frequency measurement system and (b) its printed circuit board.**

low-pass filter (LPF) with a cutoff frequency of 30 kHz (Voltage preamplifier SR560, Stanford Research Systems). For sustaining oscillation of the micro-capillary and reducing the QTF vibration, the insertion of the LPF is crucial for the piezoelectric readout when two distinct resonance peaks with comparable amplitudes are present.

To monitor and record the resonance frequency of the micro-capillary in real-time, the readout signal is mixed down to 1 kHz by an analog multiplier (AD734,

Analog Device) with reference clock source (33120A, Agilent) used as a heterodyne receiver. And mixed down signal is converted to TTL signal using comparator (AD8561, Analog Device) with positive hysteresis feedback for increasing toggle threshold to enhancing signal to noise ratio. Converted TTL signal is send to 100-MHz frequency counter of the data acquisition board (USB6361, National Instruments) and recorded.

## **System 2: OPU and FPGA PLL device**

Commercial OPU (HD850, Sanyo) was employed as an ADS system. Automatic power control (APC) unit was designed to operate 650-nm laser diode, and current driver circuit was built to control voice-coil actuator for position control of astigmatic lens (See Appendix A.1.). Figure 6.7 shows band-pass filter circuit of OPU for acquiring pure AC signal of resonance frequency. Full differential amplifier (AD8620, Analog Device) generates FES signal  $((V_a + V_c) - (V_b - V_d))$  from output of the OPU, followed by gain adjust amplifier (AD8620, Analog Device) for signal amplification, and band-pass filters (1<sup>st</sup> order high-pass and 4<sup>th</sup> order low-pass filters (AD8620, Analog Device)) to cut-off unnecessary frequency bands, resulting in signals within frequency band of 10-200 kHz.

Figure 6.8 shows OPU controller with integrated filter circuit, APC, and voice-coil controller. OPU and OPU controller were connected by 24-pin flat cable and fixed using custom-designed aluminum block. Table 6.1 summarizes the specifications of custom-designed OPU controller.

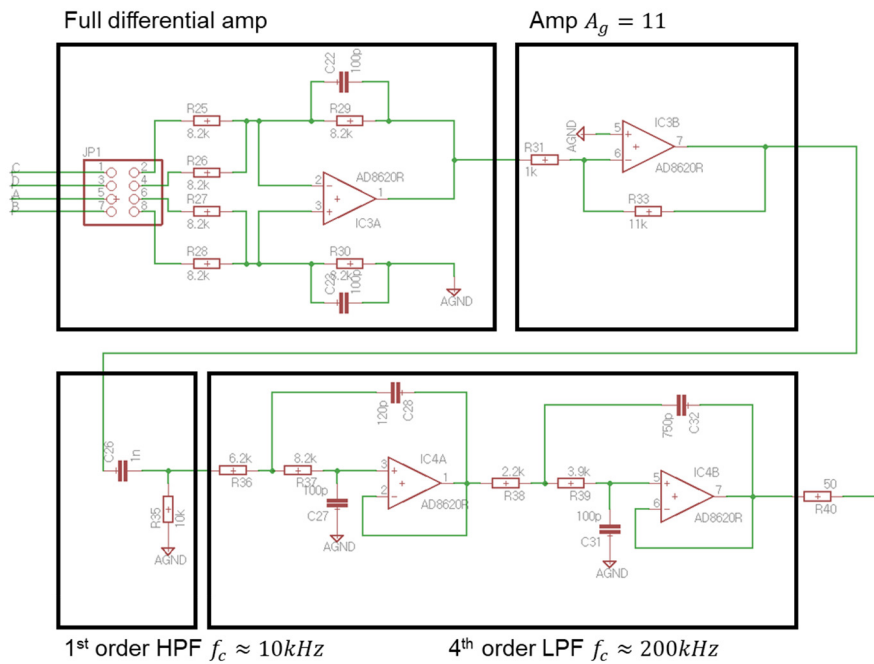


Figure 6.7 Electrical circuit of signal processing unit of OPU system.

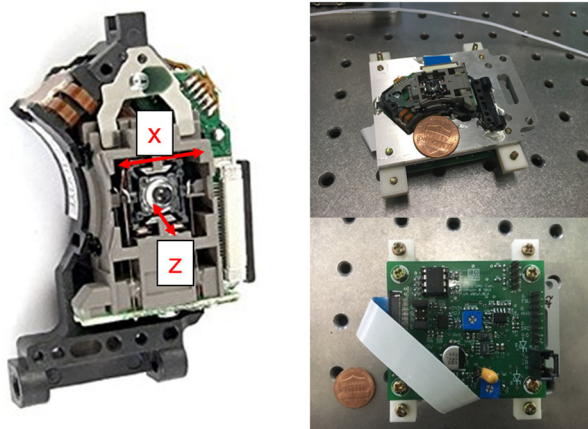
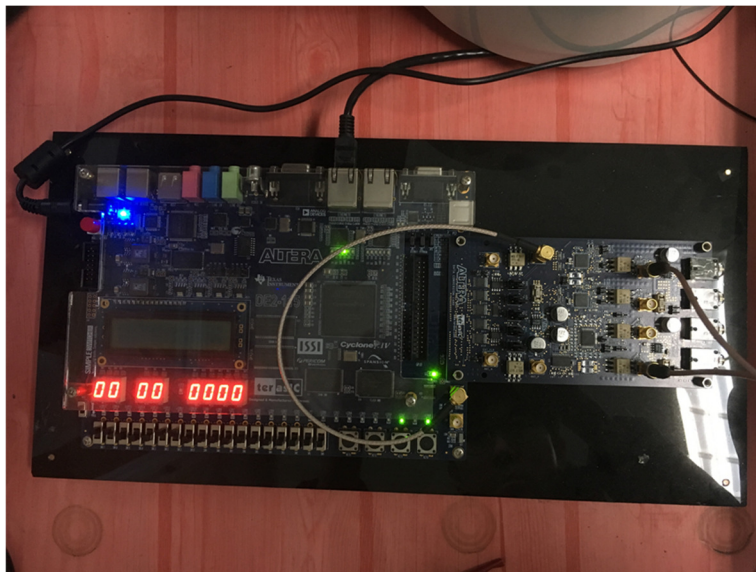


Figure 6.8 Voice coil actuators built in OPU to move the astigmatic lens along the vertical z and lateral x directions. And picture of integrated OPU controller.

**Table 6.1 Specifications of the OPU controller**

<b>Item</b>	<b>Specification</b>
<b>(Optical performance)</b>	
<b>Laser wavelength</b>	650 nm
<b>Laser power</b>	5 mW
<b>Numerical aperture of objective lens</b>	0.6
<b>Working distance</b>	1.67 mm
<b>(Focusing actuator performance)</b>	
<b>Working area</b>	-0.7 ~ 1.1 mm or more
<b>Sensitivity</b>	80 $\mu\text{m}/\text{V} \pm 3 \text{ dB}$ at 5 Hz
<b>(Tracking actuator performance)</b>	
<b>Working area</b>	$\pm 0.4$ mm or more
<b>Sensitivity</b>	60 $\mu\text{m}/\text{V} \pm 3 \text{ dB}$ at 5 Hz
<b>(Signal specification)</b>	
<b>linear area in S-curve</b>	6 $\mu\text{m}$
<b>S-curve level (without gain)</b>	0.86 mV $\pm 35 \%$
<b>Signal gain</b>	1 to 11
<b>High-pass filter cutoff frequency</b>	10 kHz, 1 <sup>st</sup> order
<b>Low-pass filter cutoff frequency</b>	200 kHz, 4 <sup>th</sup> order

The output of OPU controller contains information on mechanical behavior of the resonator, and it is transmitted to FPGA board (DE2-115, Altera showed in Figure 6.9) through analog to digital converter (ADC). Feedback signal from FPGA is amplified by current buffer amplifier (LT1210, Linear Technology) and fed back to piezoelectric actuator beneath the resonator. The voice-coil

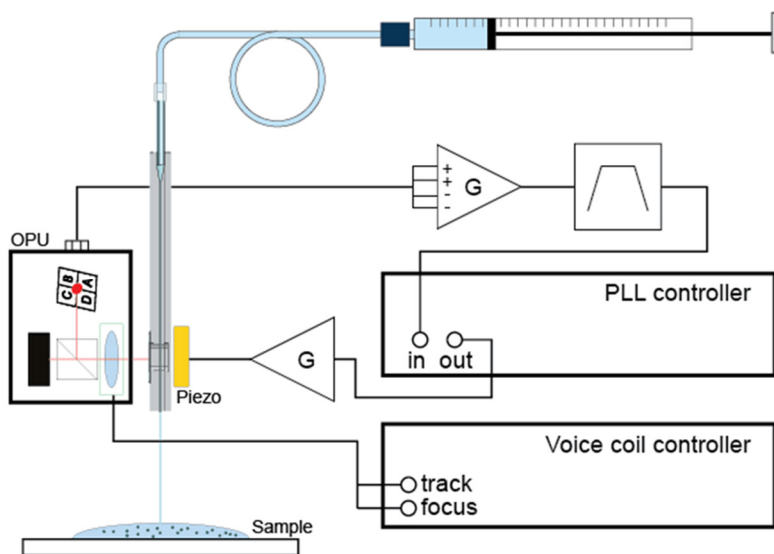


**Figure 6.9 PLL functionalized FPGA board.**

controller was controlled by the Python script code via data acquisition board (USB-6363, National Instrument).

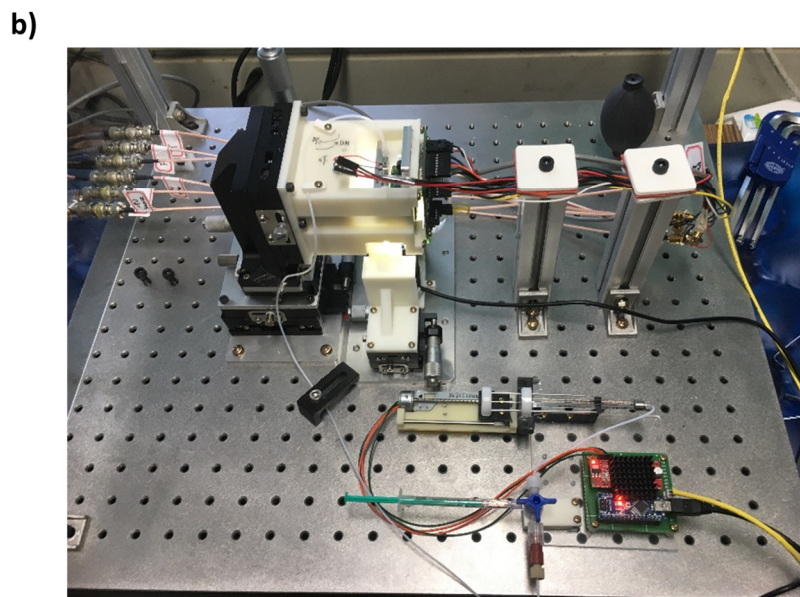
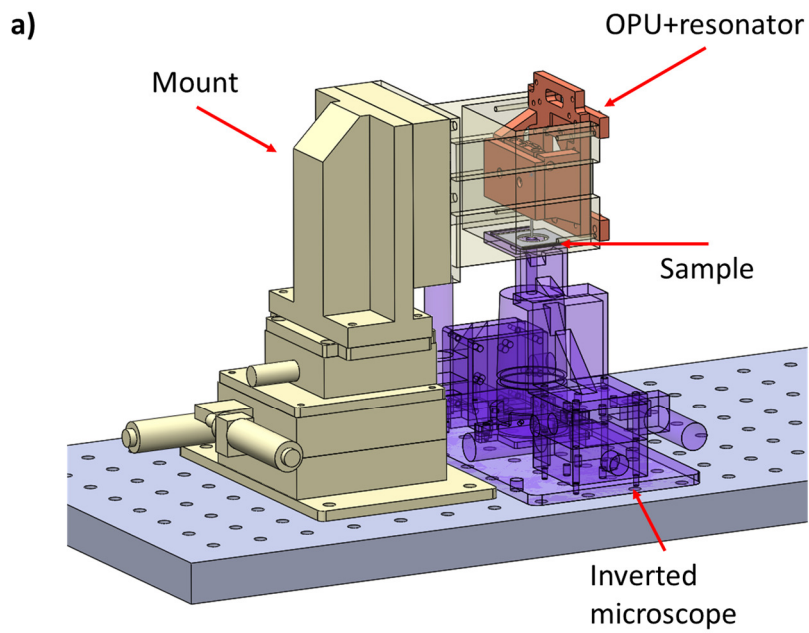
Figure 6.10 shows the overall experimental schematic. Target sample particles and liquids are placed on the slide glass, then the analytes are transported to the mass sensing region of the resonator by pressure controlling using syringe controller. At the same time, voice coil actuator built in the OPU controls the position of the astigmatic lens to settle the position of incident laser spot on the capillary surface. During the experiment, the PLL device controls the resonance of the resonator and recorded the resonance frequencies and transmit it to the PC.

Figure 6.11 shows illustration of experimental setup (a) and photograph (b) of the system which integrates inverted microscope, manual stage, OPU, and



**Figure 6.10 Experimental setup of micro-capillary resonator with OPU readout system.**

micro-capillary resonator. Target particle samples were loaded on the slide glass and injected into the resonator using syringe controller while slide glass is manipulated using XY stage and monitored by inverted microscope.



**Figure 6.11 (a) Schematic of OPU-resonator system with inverted microscope and (b) its picture.**

### **6.3. Notice**

The initial design of the self-oscillation circuits used in this dissertation was made by S.Manalis Laboratory of Massachusetts Institute of Technology. Also, the PLL FPGA logic is from the same laboratory. The author clarifies it and redesign the circuits and the PLL board for implementation and optimization to the micro-capillary resonator. The transimpedance amplifier for using piezoelectric QTF, OPU readout circuit used for astigmatic detection system and rest of the others including data logging software, automated alignment setup, etc. are made by the author.

# CHAPTER 7.

## DEVICE CHARACTERIZATION

This chapter introduces the characterization of the two types of devices; a micro-capillary string resonator integrated with QTF readout, and a micro-capillary bridge resonator integrated with OPU readout. Readout scheme of the QTF readout system was compared with conventional optical-lever detection scheme. Mode-split of the resonator was observed using OPU readout system by adjusting the incident laser spot position on the capillary surface. Finally, Frequency responses were examined with varying fabrication parameters, and frequency stabilities of fabricated devices were measured.

### 7.1. Piezoelectric readout validation

To compare the piezoelectric transduction of the vibration of micro-capillary resonator, a custom optical-lever setup is built with a 650-nm laser diode, beam splitter, focusing lens, and a two-segmented photodiode as shown in Figure 7.1 (a). Since micro-capillary resonators are transparent to the laser wavelength, a thin (~20 nm) gold deposited layer is prepared onto the upper surface of resonator by using metal sputtering machine.

For two readout schemes, signal transfers in the resonator can be understood by block diagram (Figure 7.1 (b)). Once an external excitation signal vibrates the resonator, the vibration of the resonator is transmitted to the QTF sensing probe and the response by the QTF probe reflects back to the resonator. To effectively

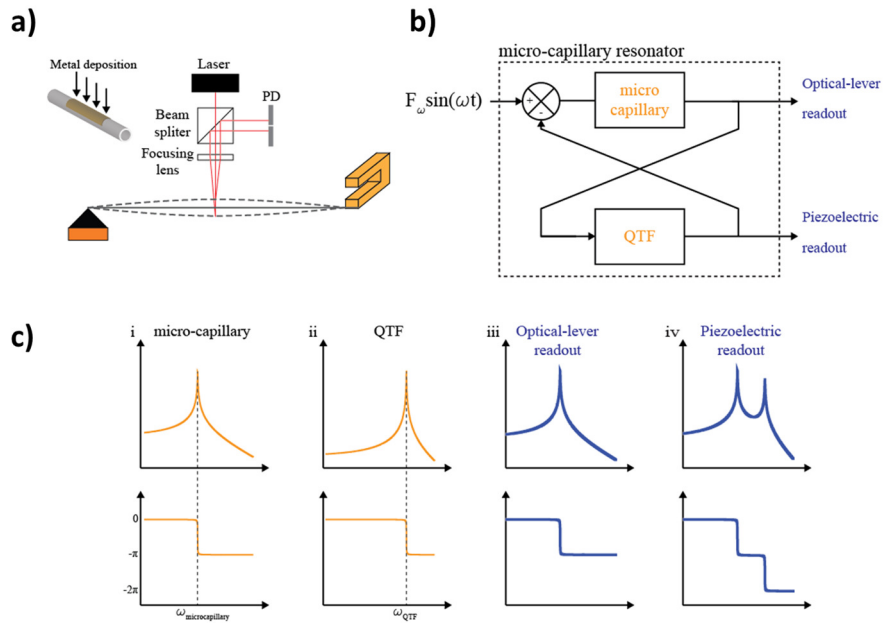


**Figure 7.1 Signal transfers in the micro-capillary resonator with QTF readout system and its resonance spectra by optical-lever and piezoelectric readouts. (a) Experimental schematic for optical-lever readout of resonator with partial gold coating. (b) Block diagram for the resonator. (c) Amplitude and phase spectra of individual components and combined resonator system obtained by optical-lever and piezoelectric readouts.**

sense the vibration of the resonator by the QTF in both open and closed loop operations, the resonance frequency of the resonator is recommended to be lower than and far from that of the QTF (Figure 7.1 (c) i and ii). When the overall response of the resonator is measured by the optical-lever readout, the resonance of the QTF is significantly attenuated by the low-pass filter behaviors of the micro-capillary resonator and the transmission loss (Figure 7.1 (c) iii). In contrast, the piezoelectric readout can easily capture two resonance behaviors,

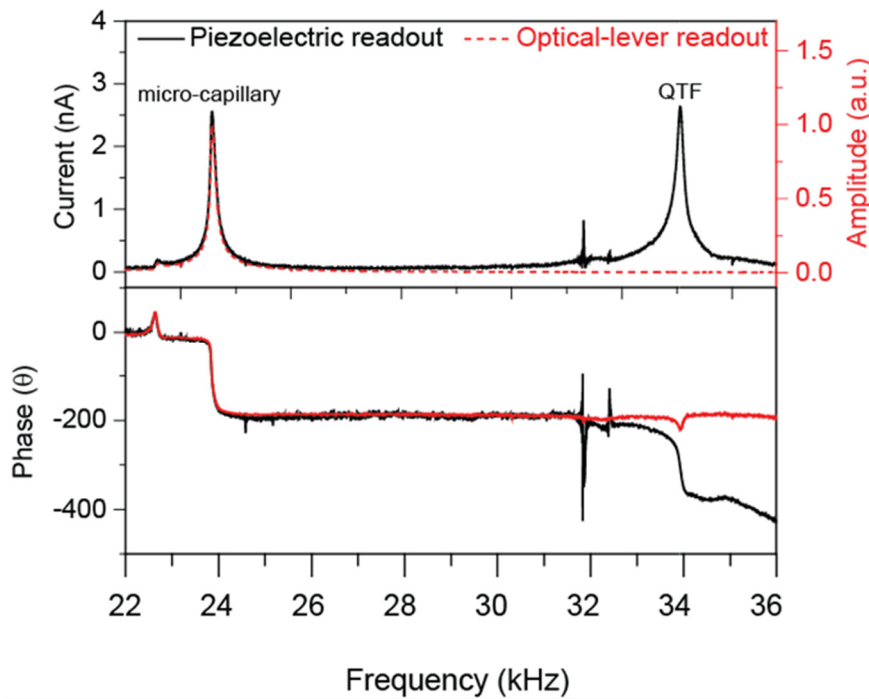


**Figure 7.2 Amplitude and phase spectra of a water-filled micro-capillary resonator measured by optical-lever and piezoelectric readouts. While the resonance peak for the micro-capillary resonator around 24.5 kHz is universally detected, the QTF resonance around 33 kHz is exclusively measured by the piezoelectric readout.**

on for the micro-capillary and the other for the QTF (Figure 7.1 (c) iv). If micro-capillary resonator with high resonance frequencies are required for specific applications, a QTF with a resonance frequency higher than those of micro-capillary resonator is recommended. Commercial QTFs with resonance frequencies up to ~153 kHz are readily available.

To validate the transfer function diagram of QTF and optical-lever readout, a 6.5-mm length, 50 and 30  $\mu\text{m}$  outer and inner diameter, 0.3  $N$  axial tension applied, and water filled inside of micro-capillary is tested. The theoretical resonance frequency of micro-capillary is estimated 23.13 kHz and commercial QTF which has 32.768 kHz of resonance frequency is used. The QTF and optical readout results via frequency sweep method are shown at Figure 7.2. While the piezoelectric readout captures two resonance peaks, one is micro-capillary near 24.5 kHz and the other is near 33.0 kHz for QTF itself, the optical-lever readout shows a single resonance peak of micro-capillary only. The results prove that the piezoelectric detection as a mechanical contact method to the resonator can examine the resonance of micro-capillary without intervention its motion, as the non-contact method of optical-lever detection show.

Another validation of piezoelectric readout scheme of micro-capillary resonator is excitation topology. One node of the resonator is used as a force detection sensor, while the other node plays a role of actuator, the proposed scheme is asymmetric vibrating strategy. To verification the motion of the micro-capillary is symmetric, a soft cantilever probe of atomic force microscopy (AFM) examined the actual vibration amplitude of the resonator when it undergoes resonance motion.

A soft AFM cantilever (Octo-1000D, Micromotive) was used with a AFM (Nx10, Park Systems). The calibrated stiffness of the soft cantilever is 0.115  $N/m$  which is three orders of magnitude smaller than that of the micro-capillary estimated by equation  $4T/d$  ( $\sim 200 N/m$ ) [110], thus contact of AFM cantilever to the resonator regarded to do not harm the resonance motion. The soft AFM

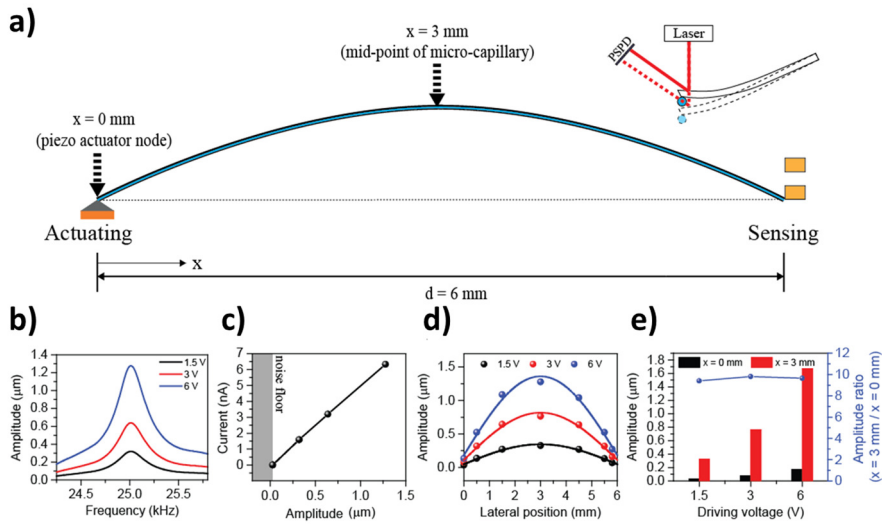


**Figure 7.3 Amplitude measurement of the micro-capillary resonator. (a) Schematic for atomic force microscope cantilever-based measurement of local vibration amplitude of the micro-capillary. (b) Amplitude spectra acquired at the mid-point ( $x = 3\text{ mm}$ ) of the micro-capillary. (c) Current versus amplitude and noise floor of the piezoelectric readout. (d) Local amplitudes of the micro-capillary measured at several lateral positions and their sinusoidal fits with various actuation voltages. (e) Amplitudes at the piezo actuation node ( $x = 0\text{ mm}$ ) and the mid-point ( $x = 3\text{ mm}$ ) of the micro-capillary and their ratios as a function of the actuation voltage.**

cantilever was brought close to and made contact with the mid-point of the micro-capillary (Figure 7.3 (a)). When the micro-capillary was actuated, electrical signals from the QTF and vibration amplitudes from the position sensitive photo detector (PSPD) in the AFM were measured and recorded simultaneously (Figure 7.3 (a)). Examination results were shown in Figure 7.3

(b) for a micro-capillary with the length of 6 mm. Next, the vibration amplitudes of the micro-capillary are measured by frequency-sweep measurement at several points along its longitudinal direction and they have seen symmetric responses (Figure 7.3 (c)). Vibration amplitude ratios between the actuation node and the mid-point of the micro-capillary were found to be  $\sim 10$  for tested drive amplitudes (Figure 7.3 (d) and (e)).

## **7.2. Mode-split resonance motion detection**

To investigate the resonance motion of mode-split micro-capillary resonator, an OPU measurement setup was used. Once capillary is aligned such that the laser gets focused on the capillary surface, laser spot is actuated in both lateral and vertical direction using voice coil actuators to measure the resonance motion of the micro-capillary resonator. The device under tested micro-capillary has 200  $\mu\text{m}$  major diameter,  $\sim 0.6$  inner and outer ratio, asymmetric factor of 0.0458 (so that the minor diameter is 190  $\mu\text{m}$ ), and the 3.8 mm length with silicon oil liquid filled inside the fluidic channel. The azimuth angle is  $30^\circ$ . The estimated resonance frequencies along the major and minor axes are calculated to 66.16 and 69.34 kHz, respectively.

Figure 7.4 (a) shows FES signal as the laser spot moves vertically by adjusting the voice coil actuator to shift the astigmatic lens. As laser spot passes through its focus on the capillary surface, S-curve is shown with its origin corresponding to the perfect focus (When the voice coil actuator moved to the height to 50  $\mu\text{m}$ ). Next, laser was moved laterally to measure contour of the capillary surface with hopping mode (Figure 7.4 (b)). The range of lateral

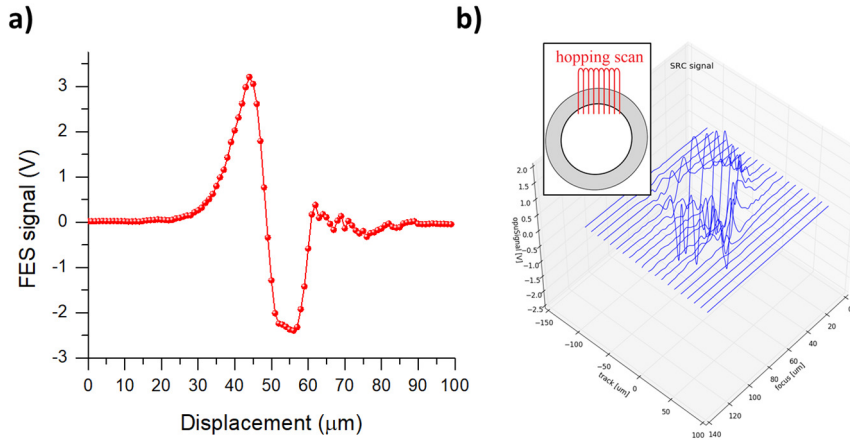


**Figure 7.4 (a) Measurement of the S-curve on a surface of micro-capillary. (b) Acquiring the contour of micro-capillary by hopping scanning mode using voice coil actuators in OPU.**

motion was restrained to be less than  $0.35 \cdot R$  from the capillary center since OPU loses the laser signal due to drastic decrease of laser intensity as reflection angle gets too large as it moves out of the range (Figure 7.5 (a)).

Based on frequency sweep method, resonance frequency of the resonator was measured to be varying in-between 63 to 71 kHz with the four different incident spot position  $\beta$  ( $= x_l/R: -0.35, -0.2, 0.0, 0.2$ ) (Figure 7.5 (a) and (b)). As predicted by theoretical resonance frequency, measured resonance frequencies along the major and minor axes were found to be 69.5 and 66 kHz, with their corresponding quality factor of 100 and 98, respectively. The estimated azimuth angle of the resonator was 30 degrees between the minor axis and global y-axis, which yields higher actuating force to the minor axis, thus peak amplitudes of

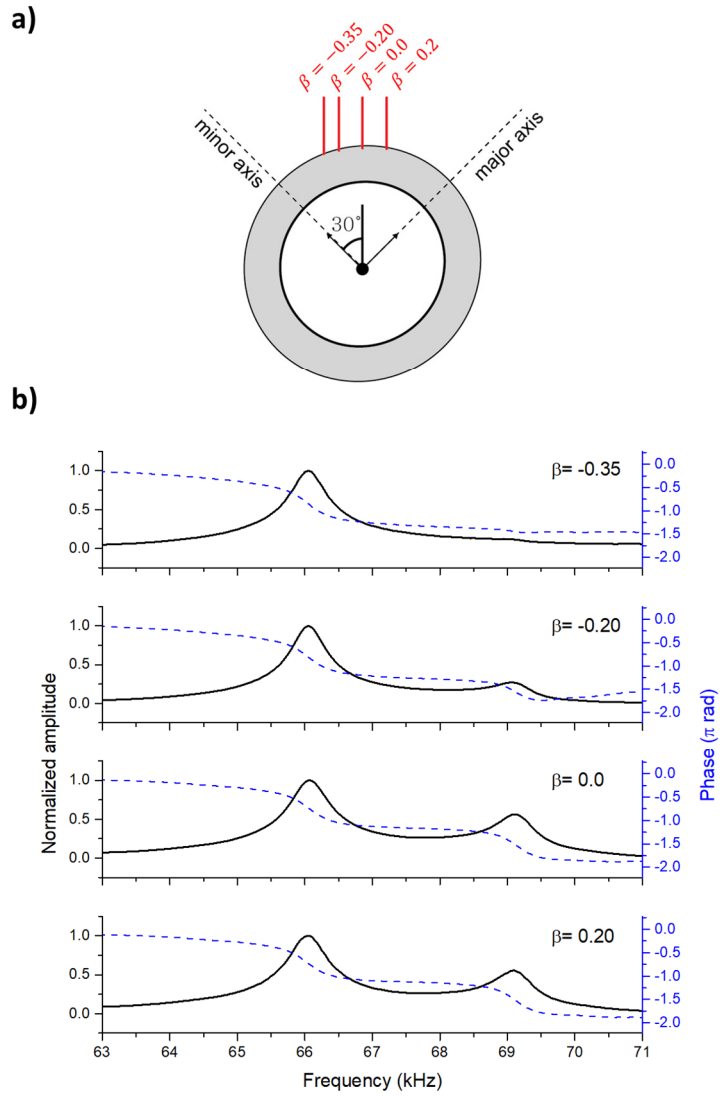


**Figure 7.5 (a) Examine the resonance amplitude using astigmatic detection system along the surface of micro-capillary and (b) frequency sweep results exhibit the distinguished major and minor axes resonance motion of micro-capillary resonator.**

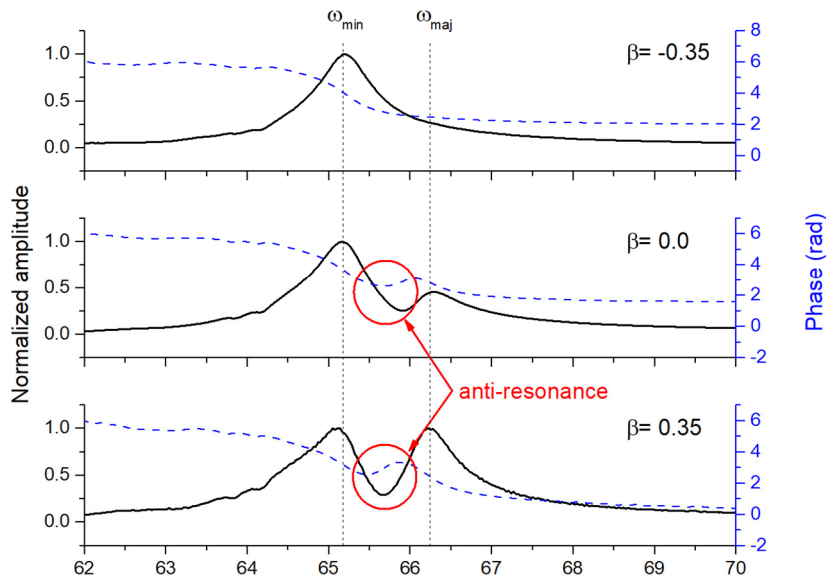


**Figure 7.6 The frequency response of the mode-split micro-capillary resonator when anti-resonance peak occurred.**

the minor axis resonance were measured to be all larger than that of the major axis.

It was also found that all four cases in Figure 7.5 (b) show phase delay at the resonance frequencies. It implies that the resonance frequencies along the major and minor axes are sufficiently discernible when they have quality factor of  $\sim 100$ , and only 3.5 kHz of difference in resonance frequency under moderate air pressure without vacuum environment.

Interestingly, one of the fabricated resonators, the anti-resonance peak was observed between two resonance frequencies as predicted by superposition of the frequency response when  $z_{min}(\omega)$  and  $z_{maj}(\omega)$  are set to be positive sign

( $z_{min}(\omega)$ ) and negative sign ( $-z_{maj}(\omega)$ ) when calculating the expected frequency response. Phase response also exhibits an increase of phase delay at anti-resonance frequency (See Figure 7.6).

### **7.3. Effects of fabrication parameters**

In this subject the change of resonance characteristic with respect to the change of fabrication parameters of micro-capillary resonator is discussed.

#### **Resonance frequencies and quality factors**

An aspect ratio (length-to-diameter ratio) of the micro-capillary resonator was fabricated to be greater than 80 to be modeled as a string type resonator. Length of micro-capillary resonator was tuned to be ranging from 4 to 10 mm. the resonators are filled with water inside the channel with applied tension of 0.3 N, and outer and inner diameter of 50 and 30  $\mu\text{m}$ , respectively (Figure 7.7 (a)). Resonance frequencies of the fabricated resonators were calculated using the Young's modulus of glass capillary of 62 GPa. Frequency sweep method is applied to measure the resonance peak via QTF readout method. Difference between calculated and measured resonance frequencies are within 6 %, showing good agreement with each other (Figure 7.7 (b)). Quality factors were extracted by applying a simple harmonic oscillator model (Figure 7.7 (c)) to be ranging from 120 to 270 as shown in Figure 7.7 (d).

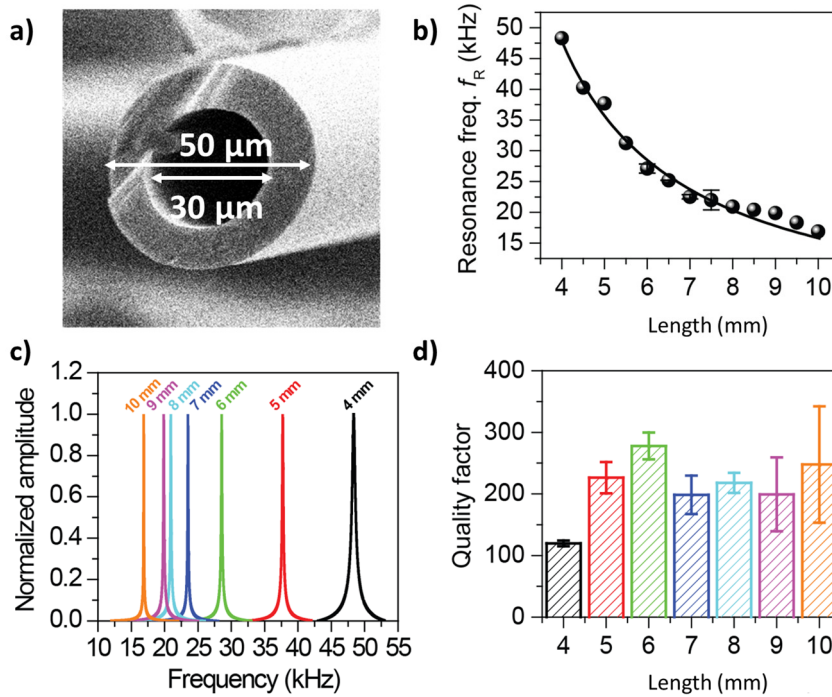


**Figure 7.7 (a) Scanning electron micrograph of cross-section area of micro-capillary used for a string type resonator. (b) Resonance frequency as a function of length of the micro-capillary resonator filled with water. Resonant characteristic of fabricated micro-capillary resonator about (c) amplitude spectra and (d) quality factors of which lengths range from 4 to 10 mm.**

Next, the bridge-type resonators are fabricated by tuning the aspect ratio to be less than 80 with its length lower than 4 mm. The resonators are filled with water, outer and inner diameter are 190 and 135 μm, respectively and rest of conditions are equal to the previous experiment showed in Figure 7.7. Figure 7.8 (a) shows the resonance frequencies and quality factors for the tested

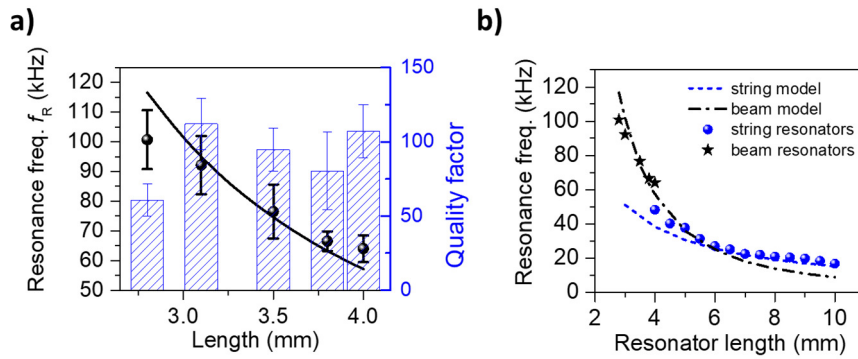


**Figure 7.8 (a) Resonant characteristics of fabricated bridge type micro-capillary resonators about resonance frequency and quality factor. (b) resonance frequencies of fabricated bridge and string type micro-capillary resonators plotted together.**

resonators. The trend of resonance frequencies follows that of the theoretical beam model, while the quality factors were derived to  $\sim 100$  that is similar to those of the string type resonators with considering the both of resonators operated in air condition. Figure 7.8 (b) shows resonance frequencies of both string and beam type resonators with changing lengths.

### **Applied tension effect on string type resonator**

For piezoelectric readout scheme that employs QTF for resonance frequency measurement, it was shown that detected amplitude of the micro-capillary resonator is proportional to the tension applied. Resonance frequencies and the corresponding peak amplitudes were measured while changing the applied

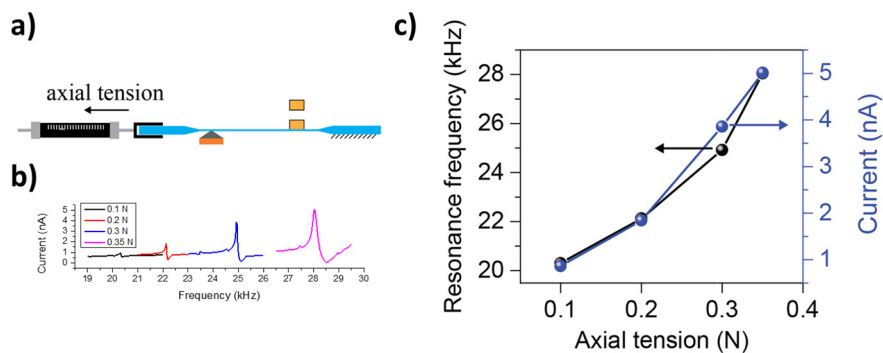


**Figure 7.9** Effect of the applied tension on the amplitude and resonance frequency signal coupling. (a) Schematic showing how to apply the axial tension before the permanent fixation with epoxy bond. (b) Frequency response plot and (c) resonance frequency and amplitude at resonance as a function of the axial tension.

tension using tension gauge as the resonators were fabricated (Figure 7.9 (a) and (b)). As the tension increases, the amplitude and resonance frequency of the resonator measured by QTF also increases (Figure 7.9 (c)) as expected theoretically (See equation (4.1)).

### **Boundary clamping effect on bridge type resonator**

A resonance frequency of the micro-capillary resonator can be varied depending on its boundary condition since it is manufactured with bottom-up assembly scheme, which might yield the different boundary clamp conditions that do not happen to monolithic MEMS resonators fabricated by a top-down

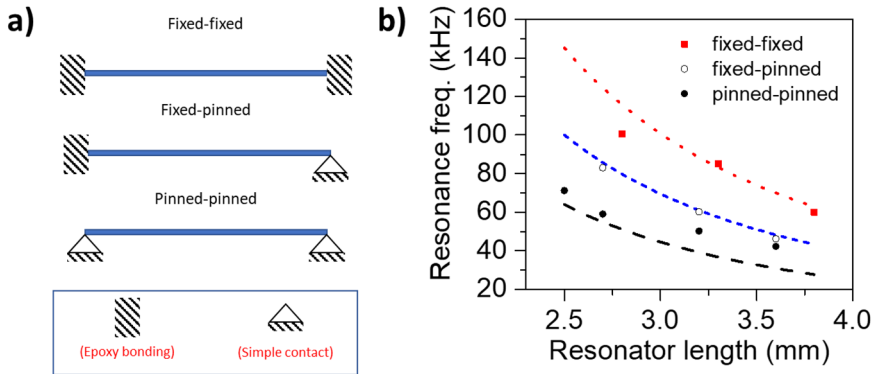


**Figure 7.10 (a) Illustration of three-types of boundary fixation of bridge type resonator. (b) Resonance frequencies plot of the bridge type resonator with different boundary conditions. The dashed lines represent theoretically estimated resonance frequency with respect to the resonator length and its color corresponds the boundary configuration of experimental data.**

process. For bridge-type resonator, effective stiffness term is strongly dependent on the boundary condition of the resonator. As its boundary gets more restrained in bending motion of the resonator, the effective stiffness increases due to it produces the higher wavenumber in the equations in Table 2.3, eventually increasing its resonance frequency, assuming any other conditions are kept consistent.

Two triangular aluminum nodes were prepared to confirm the change of resonance frequency with different boundary conditions of beam type micro-capillary resonator (Figure 7.10 (a)). First, pinned-pinned boundary condition

was applied by contacting the capillary to two nodes and frequency sweep measurement is conducted using lock-in amplifier. Second, one of the node was bonded in with epoxy to apply fixed-pinned boundary condition and the same procedure performed to acquire a resonance frequency of the resonator. Lastly, all two nodes were bonded in with epoxy to apply fixed-fixed boundary condition and measured its resonance frequency. Capillary with an inner and outer diameter of 190 and 135  $\mu\text{m}$  was used for all experiments while it was filled with liquid water.

Figure 7.10 (b) shows comparison between measured and theoretically predicted resonance frequencies for three different boundary conditions. The resonance frequencies get increased as the boundary condition change from pinned (weak constraint) to fixed (hard constraint) condition.

### **Asymmetry factor of micro-capillary**

For elliptical shaped micro-capillary resonator, mode-split of the resonance frequencies along the major and minor axes can be observed in two different resonance frequencies. A micro-capillary resonator which has asymmetric factor of 0 when the cross-section is shaped to be perfect circle, exhibits a single resonance frequency for all direction to an arbitrary azimuthal angle. As asymmetric factor gets increased (as the shape gets more elliptical) with high Quality factor, two discernable mode-split resonance peaks become more easily observed. If either the Quality factor or difference between two resonance frequencies are small (low asymmetric factor), two major and minor resonance

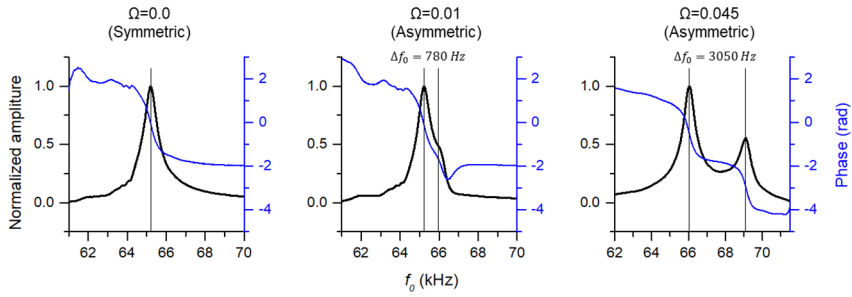


**Figure 7.11 Three experimental results of frequency spectra of micro-capillary resonators. Each resonator has different asymmetric factor.**

peaks in frequency sweep response get superposed to show a single apparent resonance peak.

Figure 7.11 shows a frequency response of several micro-capillary resonators with different asymmetric factors. When Asymmetric factor is 0.01, mode-split phenomena is observed but two peaks cannot be clearly discernible. In general,  $\pi$  radian of phase delay is observed for general 2<sup>nd</sup> order mechanical system of simple harmonic oscillator, however, the phase response of the mode-split resonator ( $\varphi^*$ ) can exhibit phase delay between  $\pi \sim 2\pi$ , which is derived from sum of two resonance frequencies along major and minor axes depending on their frequency difference and amplitude (equation (7.1)).

$$\begin{aligned}
A^* \cos(\omega t + \varphi^*) &= A_{min} \cos(\omega t + \varphi_{min}) \\
&\quad + A_{maj} \cos(\omega t + \varphi_{maj}) \tag{7.1} \\
A^* &= \sqrt{(A_{min} \cos(\varphi_{min}) + A_{maj} \cos(\varphi_{maj}))^2 \\
&\quad + (A_{min} \sin(\varphi_{min}) + A_{maj} \sin(\varphi_{maj}))^2} \\
\varphi^* &= \arctan\left(\frac{A_{min} \sin(\varphi_{min}) + A_{maj} \sin(\varphi_{maj})}{A_{min} \cos(\varphi_{min}) + A_{maj} \cos(\varphi_{maj})}\right) + n\pi
\end{aligned}$$

## 7.4. Frequency stability

Frequency stability of the micro-capillary resonator is a good indicator to find a noise level of the system, represented to index of Allan deviation. As the frequency noise of the resonator is reduced, Allan deviation decreases since average root mean square of measured frequency difference by time interval  $\tau$  gets reduced.

Figure 7.12 (c) and (d) show the normalized resonance frequency of Allan deviation  $\sigma_A$  of the string and bridge type resonators filled with water, extracted from the recorded frequency data showed in Figure 7.12 (a) and (b) as a function of the gate time  $\tau$ . Two mode-split resonance frequencies along the major and minor axes were measured for bridge-type resonator (Figure 7.12 (d)) based on astigmatic detection system. The minimum Allan deviation for string type resonator was measured to be 1.66 ppm for a gate time of 0.01 s, while that of bridge-type resonator was measured to be 0.6 of minor axis resonance and 1.1 ppm of major axis resonance for a gate time of 0.1 s.

The resonator system noise can be measured to be the smallest when the frequency of the resonator is measured under the specific gate time  $\tau_{\min}$  where Allan deviation becomes minimum to maximize the precision of its mass sensing performance. For gate time under  $\tau_{\min}$ , the resonance frequency is dominated by white noise, increasing overall Allan deviation due to intrinsic noise characteristic of the resonator materials and measurement systems (Figure 7.12. (c) and (d)). On the other hand, the long-term drift of the resonator system is a significant contributor to the noise of the system for the right-hand side.

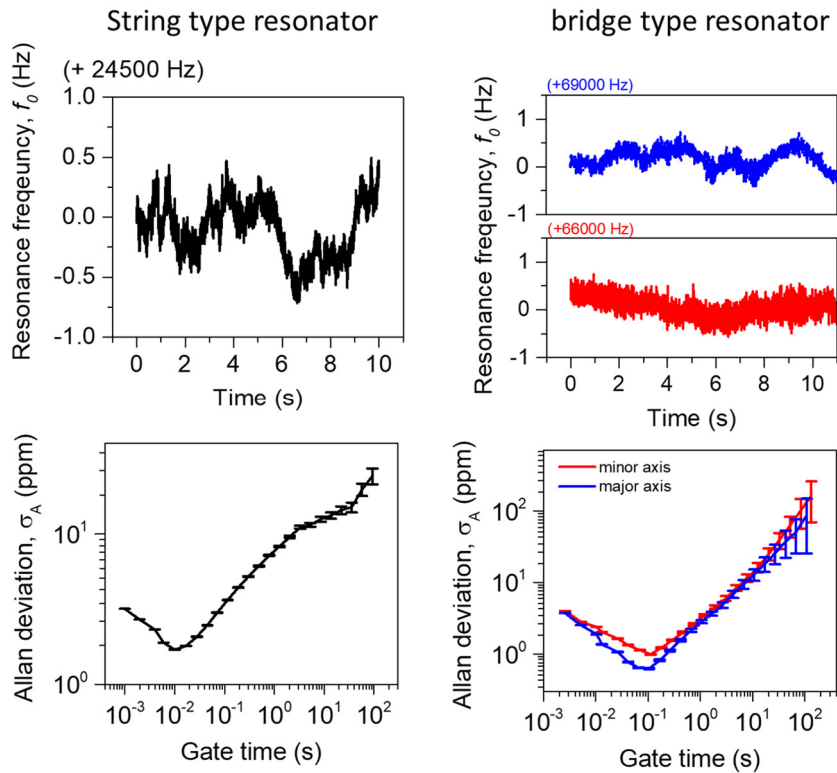


**Figure 7.12 Frequency stability of the string and bridge type resonators and their Allan deviation plot. The bridged type resonator has mode-split resonance; thus the two resonance frequencies are plotted together.**

The Allan deviation of the resonator was measured to be 1-2 order of magnitude higher than the reported hollow microtube MEMS resonator operated in vacuum [15], [36], [40]. Since the air damping is a main contributing factor for low quality factor, further performance improvement is expected for the micro-capillary resonator once vacuum packaging is incorporated.

# CHAPTER 8.

## MASS SENSING APPLICATIONS

After characterization of fabricated micro-capillary resonator is conducted, this dissertation demonstrated the several mass sensing applications including liquid density measurement, production monitoring of micro oil droplets, weighing soda-lime glass microparticles immersed in silicon oil fluid, and weighing the unicellular organism. The detail results are described in each subheading.

### 8.1. Liquid density measurement

Several liquid samples were introduced sequentially into the embedded fluidic channel for measuring frequency shift of the micro-capillary resonator. Sample liquids, the water, ethanol, and glycerol-water mixture were prepared. Resonance frequency of the resonator was measured by frequency sweep using lock-in amplifier (Figure 8.1). The theoretical normalized density responsivity can be calculated by the equation

$$\frac{1}{f_0} \mathfrak{R}_\rho \equiv \frac{1}{f_0} \left| \frac{df}{d\rho} \right| = \frac{1}{2(\rho_f + \frac{A_{wall}}{A_{fluid}} \rho_{wall})} \quad (8.1)$$

where the  $f_0$  is the reference resonance frequency of the resonator,  $\rho_f$  is the liquid density,  $A_{wall}$ ,  $A_{fluid}$  are cross-section area of the resonator wall and

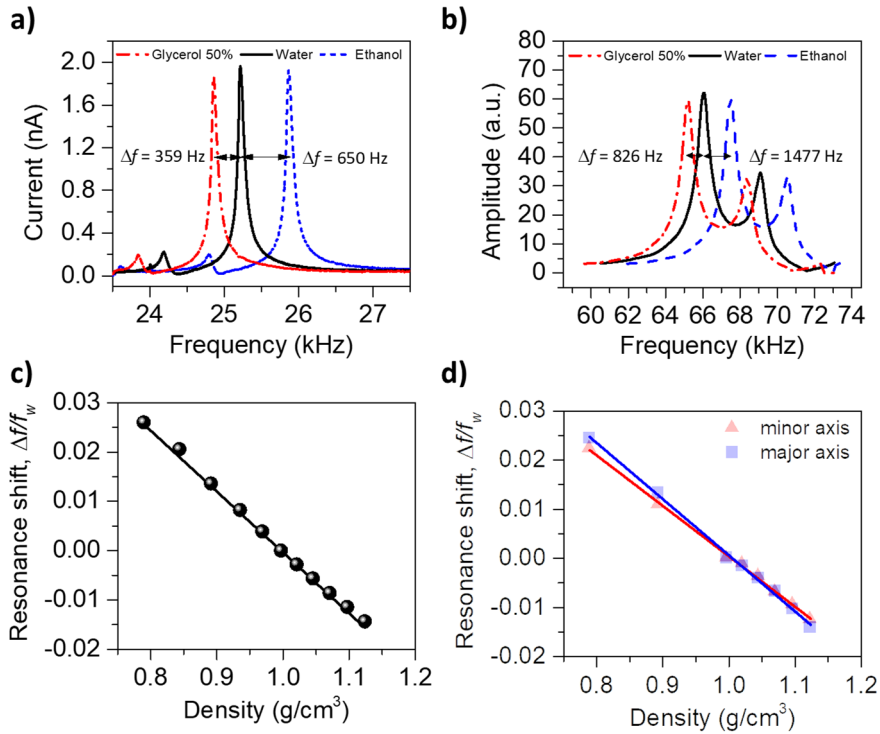


**Figure 8.1 Resonant spectra of the (a) string and (b) bridge type microcapillary resonators filled with various liquid samples. Resonance frequency shift of the (c) string and (d) bridge type resonators measured while water, ethanol-water mixtures, and glycerol-water mixtures are sequentially introduced. The bridge type resonator has mode-split, thus the shift plot of the two resonances are plotted together.**

channel, and the  $\rho_{wall}$  is resonator density. In this experiment, the reference resonance frequency  $f_0$  is set to the case of water filled resonator.

The density responsivity of the string type resonator shown to be  $-3,088$  Hz/ $\text{g-cm}^3$ , while the mode-split bridge type resonator shown to be  $-6,781$  and  $-7,894$

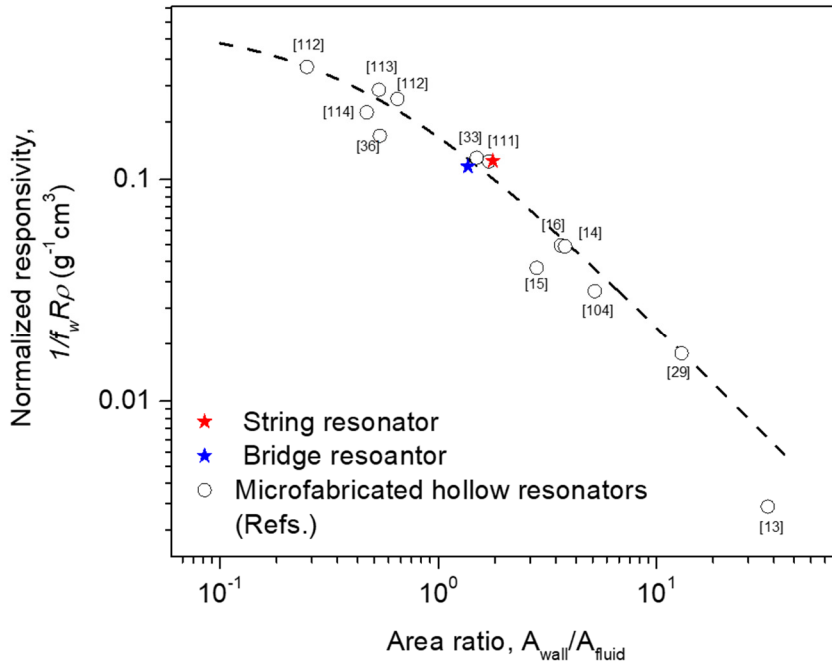


**Figure 8.2 Normalized density responsivity of the string and bridge type micro-capillary resonators in comparison with those of other micro fabricated density sensors found from literatures plotted as a function of area ratio (density of wall,  $\rho_{\text{wall}}$ , is set to be  $2.25 \text{ g/cm}^3$ ). The dashed line shows the theoretically estimated responsivity.**

Hz/g-cm<sup>3</sup> along the minor and major axes resonances, respectively. The bridge type resonator had mode-split resonance, thus two resonance frequency shifts were measured during liquid density experiment, resulting they have same normalized density responsivity. Because the density responsivity relies on the cross-sectional area ratio between the wall and fluid, not the area shape. Therefore, reducing wall thickness helps to increase the normalized density

responsivity of the resonator, but the miniaturization does not necessarily to improve it.

Normalized density responsivity of the micro-capillary resonators was plotted as a function of the ratio of resonator wall cross-sectional area to channel cross-sectional area (area ratio) and compared with those of other MEMS density sensors [13], [14], [16], [29], [33], [36], [104], [111]–[114] and showing comparable ability (Figure 8.2). Once a thinning process of the resonator wall such as selective exterior etching is fully developed, the density responsivity can be further improved.

## **8.2. Quality monitoring of production of micro oil droplets**

For monitoring the production of the micro oil droplets, a T-junction droplet generator was configured at one entrance of the resonator as shown in Figure 8.3. The string type resonator with piezoelectric readout system is used in this experiment, the resonator has inner diameter of 30  $\mu\text{m}$ . The interior of the droplet generator was hydrophilic, so mineral oil was used as a disperse phase and water was used as a continuous phase (i.e. mineral oil droplets in water). In the water, a surfactant (Tween20, Sigma Aldrich) was mixed at a volume fraction of 0.5%. Pressure settings for the droplet generator were set to produce oil droplets of which mean radii are approximately 28  $\mu\text{m}$ . When an oil droplet passes through the resonator, it was squeezed to form a plug since its diameter is larger than the inner diameter of the resonator as shown in Figure 8.3 (3).

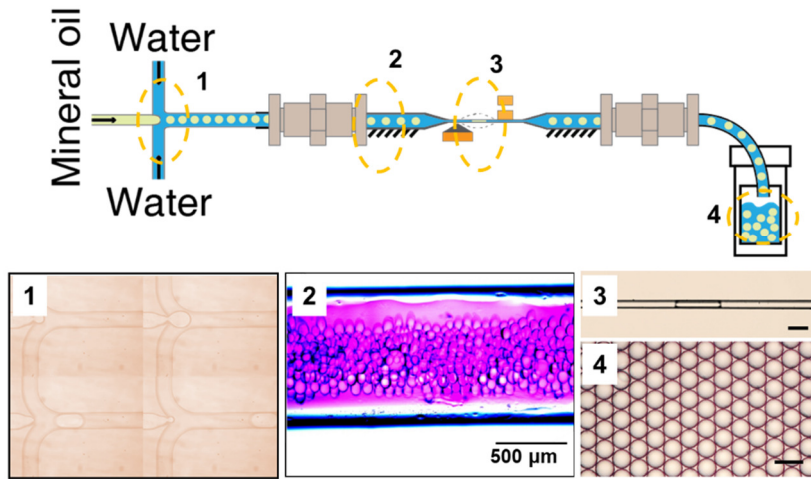


**Figure 8.3** A micro droplet generator configured at the inlet of the microcapillary resonator for real-time monitoring of droplet mass. The inset figures 1, 2, 3, and 4 show snapshots at each section.

Once they came out of the microchannel of the resonator, their shapes restored back to spheres and collected in the outlet vial (Figure 8.3 (4)). Since the length of squeezed plug are in general much shorter than the length of the resonator (6.5-mm in this case), the assumption of a point mass traveling through the long string resonator is valid. Figure 8.4 (a) shows resonance frequency shifts of the resonator recorded when oil plugs with three different radii pass through the resonator. The post-processing of finding resonance shift peaks from the raw-data is described in Appendix A.2. The sign of buoyant mass of oil plug is negative in water phase, the resonance shift increases. To quantify equivalent radii of oil plugs, buoyant mass of each plug was first calculated from fitting measured resonance shift data with the equation

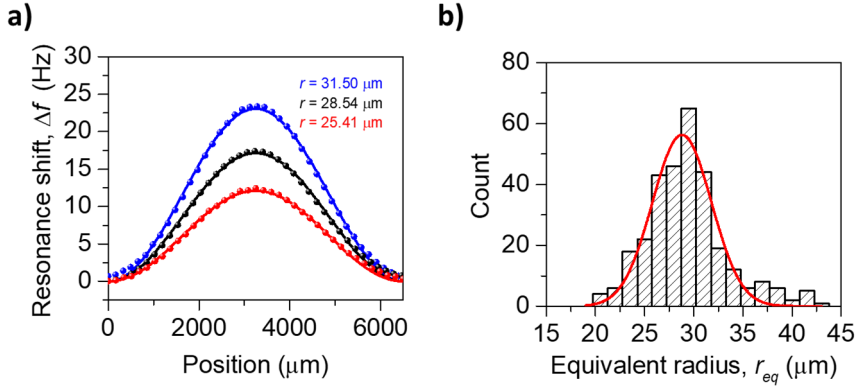


**Figure 8.4 (a) Resonance frequency shifts fitting upon a transit of mineral oil plugs of which equivalent radii are 25.4, 28.5 and 31.5  $\mu\text{m}$ , respectively. (b) Histogram for the equivalent radius of oil droplets (cumulative counts are 310).**

$$\frac{\Delta f}{f_w} = \frac{1}{\sqrt{1 + \frac{m_p}{m_r} 2 \sin^2\left(\frac{\pi x}{L}\right)}} \quad (8.2)$$

where  $\Delta f$  is the resonance frequency shift due to an oil plug transiting the resonator,  $f_w$  is the water-filled resonance frequency of the resonator,  $m_p$  is buoyant mass of oil plug,  $m_r$  is the entire mass of the resonator, and  $x$  and  $L$  are lateral position of the plug and length of the resonator, respectively. Then, an equivalent spherical radius,  $r_{eq}$ , can be given by

$$r_{eq} = \left( \frac{3}{4\pi} \frac{m_p}{\rho_w - \rho_o} \right)^{\frac{1}{3}} \quad (8.3)$$

where  $\rho_w$  and  $\rho_o$  are densities of water and mineral oil, respectively. Measurements were continued for several hundreds of oil plugs and a histogram of the equivalent radius was acquired with the average of 28.47  $\mu\text{m}$  and standard deviation of 4.03  $\mu\text{m}$  (Figure 8.4 (b)).

Unless a higher magnification is employed, small difference in the droplet size cannot be easily observed, even with a higher magnification lens, conventional far-field optical measurements are diffraction limited. The proposed mass sensing-based resonator system truly offers more precise quantitative measurements for droplet sizing than general optical microscopy. Additionally, the resonator system exclusively provides density and mass of droplets.

The detection resolution of the difference in equivalent radii of oil plugs ( $\Delta r_{eq} \equiv \sigma_A/R_r$ ) is obtained by dividing the Allan deviation ( $\sigma_A$ ) of the resonator from the radius responsivity ( $R_r = df/dr$ ). The chain rule is applied to the radius responsivity to include the buoyant mass of oil plugs ( $m_p$ ) as follows

$$\Delta r_{eq} = \frac{\sigma_A}{\frac{df}{dr}} = \frac{\sigma_A}{\frac{df}{dm_p} \frac{dm_p}{dr}} \quad (8.4)$$

The derivative of  $\frac{dm_p}{dr}$  derived by spherical mass-volume relationship ( $m_p = \frac{4\pi}{3}r^3(\rho_w - \rho_o)$ ) is given by

$$\frac{dm_p}{dr} = 4\pi r^2(\rho_w - \rho_o) \quad (8.5)$$

Finally, by employing equation (8.4) and (8.5), the relationship between the mass and radius resolution is obtained as

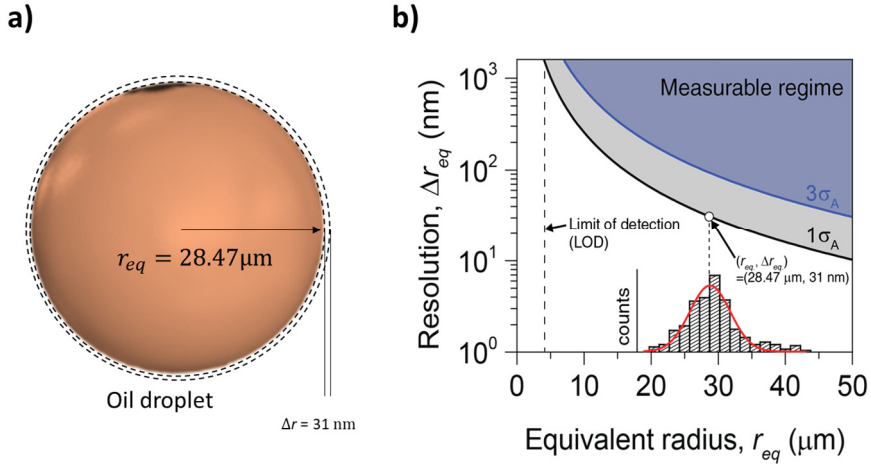


**Figure 8.5 (a)** The illustration of oil droplet shows the 31 nm radius resolution of the micro-capillary resonator when the radius of droplet is set to 28.47  $\mu\text{m}$ . **(b)** Detection resolution of the difference in mineral oil droplet radius as a function of the equivalent oil droplet radius (calculated from frequency stabilities, 1 and 3  $\sigma_A$  of string type resonator showed in the Figure 7.12). The limit of detection (LOD) for the smallest droplet radius is 4.25  $\mu\text{m}$ .

$$\Delta r_{eq} = \frac{\Delta m}{4\pi r^2(\rho_w - \rho_o)}, \Delta m \equiv \frac{\sigma_A}{R_m} \quad (8.6)$$

The mass responsivity ( $R_m = \frac{df}{dm}$ ) is acquired by the equation (8.2). Equation (8.6) indicates that the radius resolution is inversely proportional to the square of its own radius.

Figure 8.5 shows the detection resolution of the difference in mineral oil droplet radius,  $\Delta r_{eq}$ , plotted as a function of the equivalent oil droplet radius. The Allan

deviation  $\sigma_A$  used in here is 1.66 ppm (See Figure 7.12 (c)). For the average droplet radius of 28.47  $\mu\text{m}$ , measured oil droplets can be differentiated if their radius differs by approximately 31.66 and 94.99 nm based on the 1 and  $3\sigma_A$  criteria, respectively. This resolution is far superior to the diffraction limit of general optical microscopy-based techniques. As the droplet gets smaller, the resolution of  $\Delta r_{eq}$  becomes negatively affected. The colored area above each solid line represents the “measurable regime” based on each criterion. The limit of detection in the equivalent oil droplet radius is 4.25  $\mu\text{m}$ .

### **8.3. Mass sensing of glass microparticles and unicellular organism**

Weighing the glass microparticles and unicellular organism are conducted by elliptical cross-section resonator with astigmatic detection system. The elliptical resonator has two resonance motion, thus the frequency tracking the resonance shift during the target particle passes through the resonator is applied to the two resonances. This dual frequency tracking scheme is measuring the single particle simultaneously, so that the mass sensing accuracy can be improved than an only single resonance frequency measurement system.

Monodisperse NIST traceable soda-lime glass microparticles (MS00XX series, Whitehouse Scientific) were placed on the slide glass, with immersed in silicon oil (KF-96L-1.5CS, ShinEtsu) to prevent hydrophilic adhesion of the particle to slide glass or capillary (Figure 8.6 (a) and (b)).

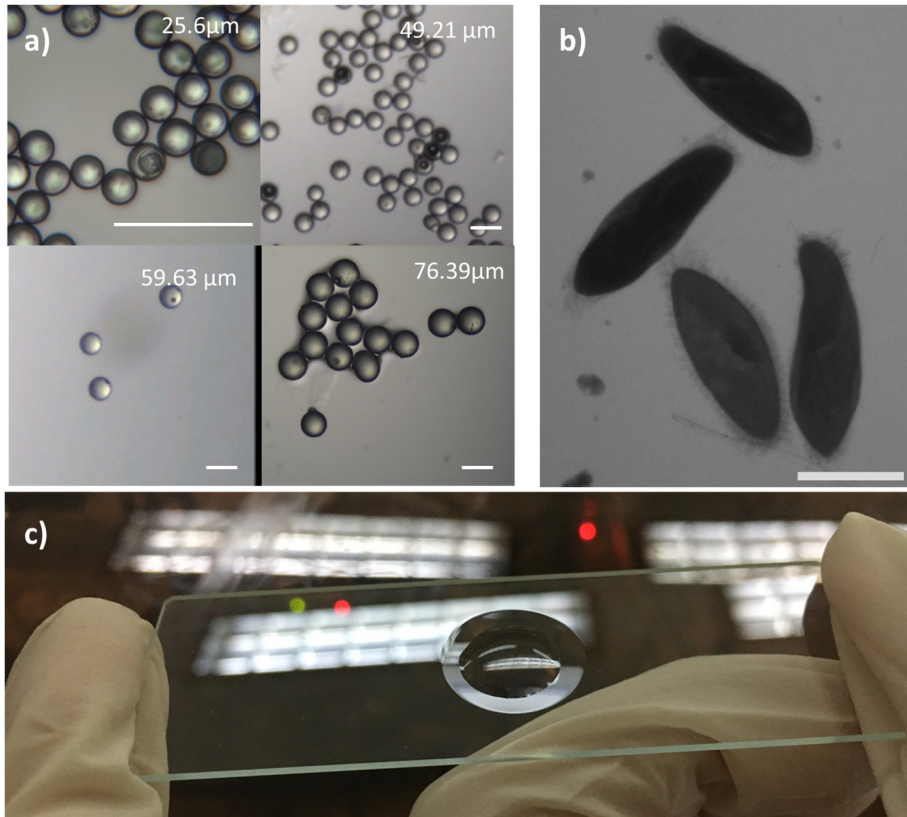


**Figure 8.6 Sample particles and unicellular organism. Microscope image of (a) soda-lime glass microparticles of four different diameters and (b) *Paramecium Aurelia*. All scale bars are 100 μm. (c) Target particles placed on the slide glass for experiment preparation.**

*Paramecium Aurelia*, one of the representative unicellular organism, was prepared suspension in culture medium (manufacturer supplied, Biozoa, in South Korea). The density of culture medium was measured to 0.998 g/cm<sup>3</sup>. As in the case of microparticles, mixture of *Paramecium Aurelia* and culture medium were placed on the glass capillary (Figure 8.6 (b) and (d)).

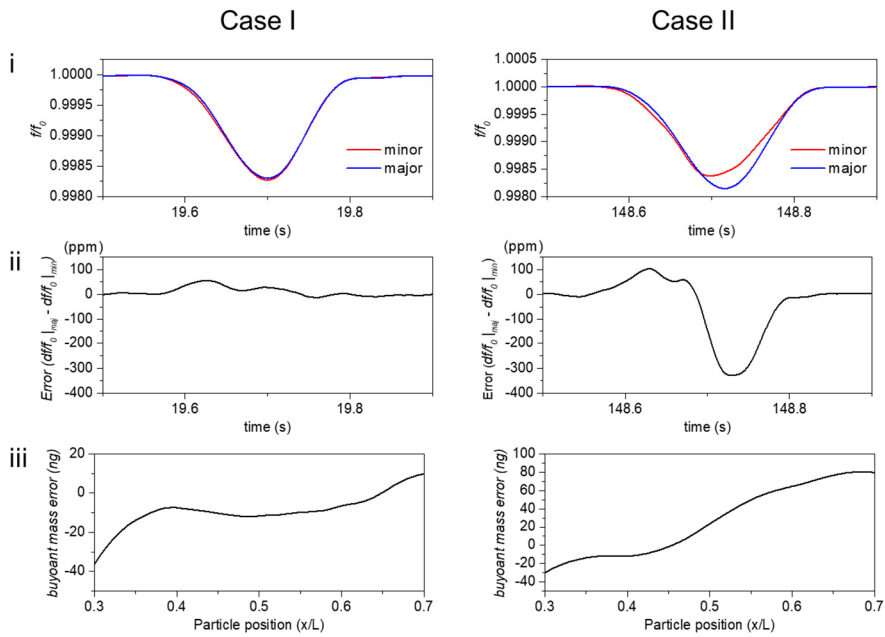


**Figure 8.7 Two frequency shift cases of 76.39  $\mu\text{m}$  diameter soda-lime glass microparticle passes through the mode-split micro-capillary resonator. In the case 1, the normalized two resonant shifts along the major and minor axes resonance almost have a similar response. On the other hand, in the case 2, the error of normalized resonant shifts is evidently observed which is estimated by the perturbation of the particle in the resonator. In case 2, maximum buoyant mass error calculated from the two-resonance motions of the resonator showed 80 ng (the total buoyant mass of particle is estimated to 368 ng) where the normalized particle position range from 0.3 to 0.7 in the resonator.**

Prepared samples were suctioned at the inlet of the micro-capillary to transport to the resonance region by control the syringe actuator. While the astigmatic

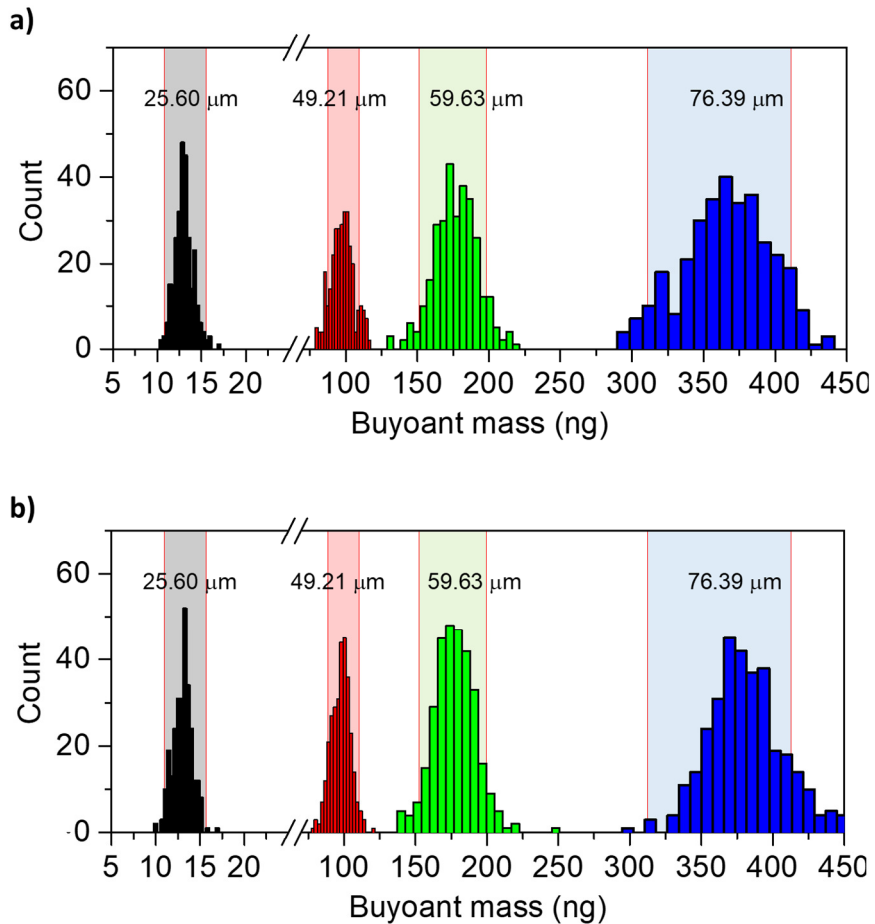
detection system and PLL device recorded the two-resonance frequencies simultaneously. Glass microparticles are examined in order by size. After experiment, ethanol and dry air injected to resonator for cleaning. After cleaning, *Paramecium Aurelia* was measured in the same procedure.

Figure 8.7 shows the two experiment cases of frequency shift of soda-lime glass microparticles which has average diameter of 76.39  $\mu\text{m}$ . In case 1, the normalized frequency shifts of major and minor axes resonator were close to each other. According to the frequency shift due to added mass theory, rewritten as below

$$\frac{\Delta f}{f_0} = 1 - \frac{1}{\sqrt{1 + \frac{m_p}{m_{eff}} \phi^2 \left(\frac{x}{L}\right)}} \quad (8.7)$$

where  $f_0$  is reference resonance frequency,  $m_p$  is buoyant mass of particle,  $m_{eff}$  is the effective mass of resonator (in the bridge type resonator, it becomes  $0.3965m_0$ ,  $m_0$  is the total mass of the resonator),  $\phi$  is normalized mode shape function, and  $x$  and  $L$  are the lateral position of particle and the resonator length, respectively.

As the particle mass, resonator mass, and the relative position of the particle inside the resonator are equal to the two-resonance motion, analytical frequency shift expectations of the two resonators should have the same quantity. However, in the case 2 in Figure 8.7, the resonance frequency shifts of the two resonators showed different, which implies the additional factor occurred that affects the frequency variation during the particle transit. In case 2, the mass error of particle calculated from two resonant shifts showed up to 80 ng between



**Figure 8.8** Histogram plot of buoyant mass of different four diameters of soda-lime glass microparticles measured by (a) minor and (b) major axes resonances of mode-split micro-capillary resonator. Each colored area represents the buoyant mass of the particles calculated from the diameter range provided by the manufacturer. Cumulative counts of each monodisperse particles are 277, 311, 309, and 324 from the smallest diameter to the largest diameter, respectively.

0.3 and 0.7 relative position of the particle in the resonator, while the estimated entire buoyant mass of particle is 368 ng. The histogram of measured mass of particles by the two-resonance motion are plotted in Figure 8.8. All the measured samples were showing the normal distribution histogram.

Substituting relative resonance frequency shifts of major and minor axes  $(\frac{\Delta f}{f_0}|_{\text{minor}} - \frac{\Delta f}{f_0}|_{\text{major}})$  can provide relative inertial difference between along the geometrically orthogonal arranged axes direction of resonator at the cross-section. From the equation (3.9), normalized relative resonance frequency shifts can be expressed as below

$$\begin{aligned} \frac{\Delta f}{f_0}|_{\text{minor}} - \frac{\Delta f}{f_0}|_{\text{major}} &\cong \frac{1}{2} \left( \frac{\Delta I}{I_r}|_{\text{minor}} - \frac{\Delta I}{I_r}|_{\text{major}} \right) & (8.8) \\ &\cong \frac{L_{\Delta} U''(x_{\Delta m})^2}{\int_0^L U''(x)^2 dx} \frac{1}{I_r} (I_{\Delta, \text{min}} - I_{\Delta, \text{maj}}) \\ &\cong \frac{L_{\Delta} U''(x_{\Delta m})^2}{\int_0^L U''(x)^2 dx} \frac{m_p^2}{I_r (m_r + m_p)^2} (e_{\text{maj}}^2 - e_{\text{min}}^2) \\ &\cong \alpha (e_{\text{maj}}^2 - e_{\text{min}}^2) \end{aligned}$$

where  $L_p$  and  $D_p$  are length and diameter of particle, respectively.  $e_{\text{maj}}$  and  $e_{\text{min}}$  represent the center position of particle's offset with respect to resonator's major and minor axes. Denotes  $\Delta$ ,  $r$  are referred to particle and resonator, respectively.

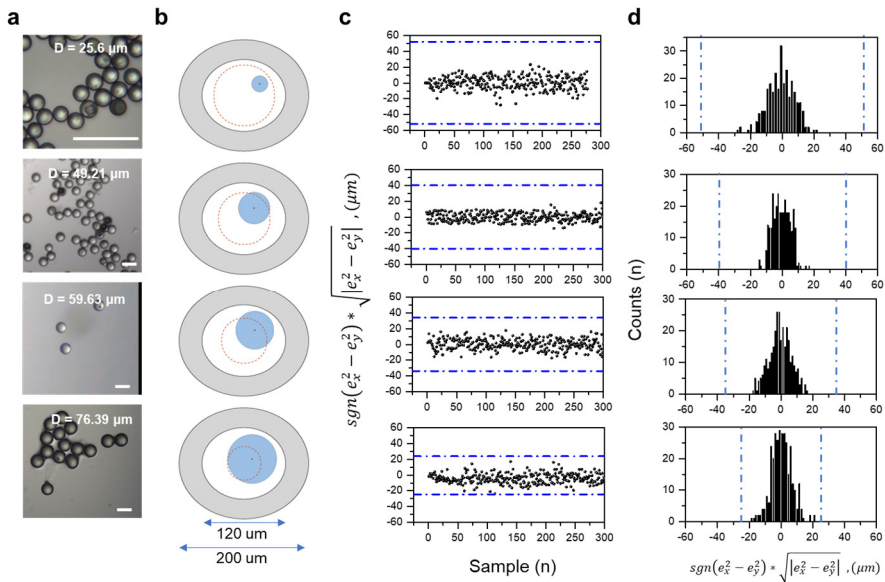


**Figure 8.9** Center position offset of particles when passing through the resonator cross-section. (a) Measured particles image. (b) Illustration of particle positioning in the resonator's inner channel. The red dash circles represent the area where the particle center can pose. (c) Relative position offset of measured particle samples of particles. Blue dash dot lines represent the maximum distance that particle offset can be located. (d) Histograms of relative position offset of measured particles.

Analysis of relative cross-sectional position offset of particles when passing through the resonator is plotted in Figure 8.9. Offset position of particle can increase inertia of resonator, thus increase the resonance frequency. Which produces error to estimate the buoyant mass of particle. For examples, if 76.39  $\mu\text{m}$  diameter of soda-lime glass microparticle is located at a maximum distance along the major or minor axis direction, the measured mass error reaches to

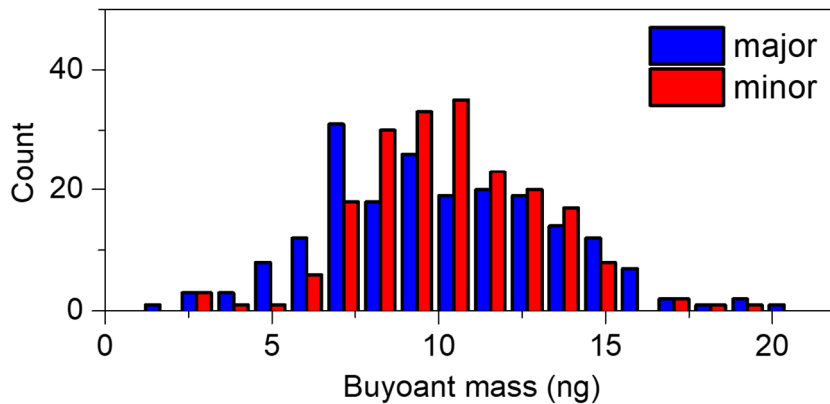


**Figure 8.10 Histogram plot of buoyant mass of *Paramecium Aurelia* measured by the major and minor axes resonances of mode-split micro-capillary resonator. Cumulative counts are 199.**

approximately 20.1%. For eliminating the inertial variation due to particle offset positioning, fitting the fabrication of inner diameter of the resonator to the diameter of target particle is required.

Next, the weighing experiment was conducted to measure the *Paramecium Aurelia*, results showed in Figure 8.10, figured out the average mass of measured cells were 10.26 and 10.09 ng calculated from the two-resonance shifts. Note that, the buoyant mass of *Paramecium Aurelia* which is regarded as a spheroid shape and has semi-axis diameter of 50  $\mu\text{m}$ , a longitudinal length of 180  $\mu\text{m}$ , an average density is between 1.06 ~1.1 g/ml, is calculated as 11.68 to 19.22 ng.

The results of measured glass particles and *Paramecium Aurelia* are tabulated in Table 8.1. Naturally, the total mean of the weighed target samples is more accurate than the mass measured from each resonant shift. Estimating the mass of the particles can be more accurate, once modeling the appropriate frequency shift equation that reflects the physical perturbation error of the particle and employing the proper estimator.

**Table 8.1 Summarized the mean and deviation results of weighed glass microparticles and unicellular organism.**

<b>Particle</b>	<b>Mean buoyant mass (ng) /deviation</b>	<b>Calculated from minor axis resonance</b>	<b>Calculated from major axis resonance</b>	<b>Total</b>
<b>Glass particle (D=25.60 <math>\mu\text{m}</math>)</b>	$\mu$	12.8560 (N=277)	12.8596 (N=277)	12.8578 (N=554)
	$\sigma$	1.0506	1.0738	1.0613
<b>Glass particle (D=49.21 <math>\mu\text{m}</math>)</b>	$\mu$	96.6752 (N=311)	96.6010 (N=311)	96.6381 (N=622)
	$\sigma$	8.0322	5.8897	7.0487
<b>Glass particle (D=59.63 <math>\mu\text{m}</math>)</b>	$\mu$	174.5532 (N=309)	174.4926 (N=309)	174.5230 (N=618)
	$\sigma$	15.1409	14.7738	14.9706
<b>Glass particle (D=76.39 <math>\mu\text{m}</math>)</b>	$\mu$	368.6679 (N=324)	378.3730 (N=324)	374.7927 (N=648)
	$\sigma$	29.7547	21.9216	24.4983
<b><i>Paramecium Aurelia</i></b>	$\mu$	10.2601 (N=199)	10.0971 (N=199)	10.1786 (N=398)
	$\sigma$	2.6775	3.4734	3.0982

# CHAPTER 9.

## CONCLUSION

This dissertation introduced the mass sensing resonators implemented in micro-capillary platform and demonstration of their applications. The micro-capillary structure which embeds an inner fluidic channel is the identical topology of SMR. Readout principles of resonance frequency modulation of SMR allow detect the mass of analytes floating inside the resonator with high resolution while the exterior of the resonator is exposed in vacuum or moderate air pressure. However, the complicated, expensive and slow fabrication process of MEMS resonators prohibit their mass resolution specialty from being widely used in research field. The micro-capillary platform can be facilely manufactured and enhance the high mass resolution capability of the SMR by mimicking their operation schemes.

This dissertation presents the details on how to migrate the working principles of MEMS resonators to the micro-capillary platform and provides the theoretical analysis of its resonance motion. The two possible resonance motions of bridge and string type of micro-capillary are examined. Also, a slightly asymmetric cross-section of micro-capillary is studied to show mode-split resonance behavior which is the unique difference from that of conventional MEMS resonators with a perfectly asymmetric diving board shape. The mass responsivity of the micro-capillary resonators is investigated considering frequency noise and dimensional size.

To operate the micro-capillary resonators, two strategies are introduced; one is self-oscillating with piezoelectric force sensing probe and the other is digital multiple phase lock loop with optical astigmatic out-of-plane displacement sensor. To prove their examination, the theoretical and experimental validation of the proposed two oscillation strategies is conducted. The overall size of the piezoelectric and astigmatic detection sensors is handheld, so that a miniaturized micro-capillary resonator can be suitable for *in vitro* biological experiments.

One of the major difference between the MEMS resonators and the micro-capillary resonators is dimensional tunability. A simple pulling process for downsizing the glass capillary to microscale resonator offers a great flexibility compared to the wafer-based microfabrication process. In this dissertation, various size of resonators from ~10 to 200  $\mu\text{m}$  diameter using a laser pulling process are demonstrated. The flexibility of laser pulling process to fabricate various dimension of micro-capillary can make the micro-capillary resonator size to fit the target analytes size for maximizing the mass responsivity of resonator.

The fact that the fabricated micro-capillary can form a micropipette shape enables integrating pipetting functionality to the mass sensing resonators. This dissertation demonstrates the weighing the microparticles and *Paramecium* cells floating in liquid using pipetting target transport strategy *in vitro* by micropipette shape of micro-capillary resonator. With vision camera, the proposed pipetting target transport method is useful when selective mass sensing of the individual cells in the population is required.

Fluid density and micro-oil droplet mass sensing applications are also exhibited. Mass-sensing micro-capillary resonator shows the size estimation of produced micro-oil droplets with 31 nm resolution when their radius is  $\sim 28 \mu\text{m}$ , which makes sensing resolution of micro-capillary resonator is far superior to that of general optical-based radius estimation technique.

Lastly, the advantage of the mode-split micro-capillary resonator is dual mass sensing. Oscillating the major and minor axes resonance motion simultaneously indicates the resonator can measure the mass of a single particle by the two sensors. This dissertation demonstrates that the resonant shifts of the two resonances show a different response in some experiment cases while weighing a single particle. This uncertainty of resonant shift can be minimized by averaging the two resonances shifts and be further reduced once a proper particle perturbation modeling is set.

The mass responsivity of the proposed micro-capillary resonator could be improved by employing a vacuum packaging. More works for integrating the other measuring tools like Whispering gallery mode (WGM), impedance analyzer, and patch clamp are possible to make the micro-capillary resonator as a total analysis system (TAS) of biological sensing platform.

## REFERENCES

- [1] A. Boisen, S. Dohn, S. S. Keller, S. Schmid, and M. Tenje, “Cantilever-like micromechanical sensors,” *Reports Prog. Phys.*, vol. 74, no. 3, p. 36101, Mar. 2011.
- [2] J. Moser *et al.*, “Ultrasensitive force detection with a nanotube mechanical resonator,” *Nat. Nanotechnol.*, vol. 8, no. 7, pp. 493–496, Jul. 2013.
- [3] X. C. Zhang, E. B. Myers, J. E. Sader, and M. L. Roukes, “Nanomechanical Torsional Resonators for Frequency-Shift Infrared Thermal Sensing,” *Nano Lett.*, vol. 13, no. 4, pp. 1528–1534, Apr. 2013.
- [4] S. Husale, H. H. J. Persson, and O. Sahin, “DNA nanomechanics allows direct digital detection of complementary DNA and microRNA targets,” *Nature*, vol. 462, no. 7276, pp. 1075–1078, Dec. 2009.
- [5] M. Dong and O. Sahin, “A nanomechanical interface to rapid single-molecule interactions,” *Nat. Commun.*, vol. 2, p. 247, Mar. 2011.
- [6] † Y. T. Yang, ‡ C. Callegari, X. L. Feng, § and K. L. Ekinci, and M. L. Roukes\*, “Zeptogram-Scale Nanomechanical Mass Sensing,” 2006.
- [7] J. Chaste, A. Eichler, J. Moser, G. Ceballos, R. Rurali, and A. Bachtold, “A nanomechanical mass sensor with yoctogram resolution,” *Nat. Nanotechnol.*, vol. 7, no. 5, pp. 301–304, May 2012.
- [8] J. L. Arlett, E. B. Myers, and M. L. Roukes, “Comparative advantages of mechanical biosensors,” *Nat. Nanotechnol.*, vol. 6, no. 4, pp. 203–215, Apr. 2011.
- [9] J. Park, S. Nishida, P. Lambert, H. Kawakatsu, and H. Fujita, “High-resolution cantilever biosensor resonating at air–liquid in a microchannel,” *Lab Chip*, vol. 11, no. 24, p. 4187, Nov. 2011.
- [10] K. Jensen, K. Kim, and A. Zettl, “An atomic-resolution nanomechanical mass sensor.,” *Nat. Nanotechnol.*, vol. 3, no. 9, pp. 533–7, 2008.
- [11] M. S. Hanay, “Single-protein nanomechanical mass spectrometry in real time,” *Nat. Nanotechnol.*, vol. 7, pp. 602–608, 2012.
- [12] J. Tamayo, P. M. Kosaka, J. J. Ruz, Á. San Paulo, and M. Calleja, “Biosensors based on nanomechanical systems.,” *Chem. Soc. Rev.*, vol. 42, no. 3, pp. 1287–311, 2013.
- [13] V. Agache, G. Blanco-Gomez, F. Baleras, and P. Caillat, “An embedded microchannel in a MEMS plate resonator for ultrasensitive mass sensing in liquid,” *Lab Chip*, vol. 11, no. 15, p. 2598, Jul. 2011.

- [14] T. P. Burg *et al.*, “Weighing of biomolecules, single cells and single nanoparticles in fluid.,” *Nature*, vol. 446, no. 7139, pp. 1066–1069, 2007.
- [15] T. P. Burg *et al.*, “Vacuum-packaged suspended microchannel resonant mass sensor for biomolecular detection,” *J. Microelectromechanical Syst.*, vol. 15, no. 6, pp. 1466–1476, 2006.
- [16] J. Lee, W. Shen, K. Payer, T. P. Burg, and S. R. Manalis, “Toward attogram mass measurements in solution with suspended nanochannel resonators,” *Nano Lett.*, vol. 10, no. 7, pp. 2537–2542, 2010.
- [17] Y. Weng, F. F. Delgado, S. Son, T. P. Burg, S. C. Wasserman, and S. R. Manalis, “Mass sensors with mechanical traps for weighing single cells in different fluids,” *Lab Chip*, vol. 11, no. 24, p. 4174, 2011.
- [18] W. H. Grover, A. K. Bryan, M. Diez-Silva, S. Suresh, J. M. Higgins, and S. R. Manalis, “Measuring single-cell density,” *Proc. Natl. Acad. Sci.*, vol. 108, no. 27, pp. 10992–10996, 2011.
- [19] M. Godin, A. K. Bryan, T. P. Burg, K. Babcock, and S. R. Manalis, “Measuring the mass, density, and size of particles and cells using a suspended microchannel resonator,” *Appl. Phys. Lett.*, vol. 91, no. 12, pp. 17–19, 2007.
- [20] S. Son *et al.*, “Cooperative nutrient accumulation sustains growth of mammalian cells.,” *Sci. Rep.*, vol. 5, p. 17401, 2015.
- [21] M. Godin *et al.*, “Using buoyant mass to measure the growth of single cells,” *Nat. Methods*, vol. 7, no. 5, pp. 387–390, May 2010.
- [22] F. Feijó Delgado *et al.*, “Intracellular Water Exchange for Measuring the Dry Mass, Water Mass and Changes in Chemical Composition of Living Cells,” *PLoS One*, vol. 8, no. 7, 2013.
- [23] A. K. Bryan, V. C. Hecht, W. Shen, K. Payer, W. H. Grover, and S. R. Manalis, “Measuring single cell mass, volume, and density with dual suspended microchannel resonators.,” *Lab Chip*, vol. 14, no. 3, pp. 569–76, 2014.
- [24] P. Dextras, T. P. Burg, and S. R. Manalis, “Integrated measurement of the mass and surface charge of discrete microparticles using a suspended microchannel resonator,” *Anal. Chem.*, vol. 81, no. 11, pp. 4517–4523, 2009.
- [25] S. Byun *et al.*, “Characterizing deformability and surface friction of cancer cells,” *Proc. Natl. Acad. Sci.*, vol. 110, no. 19, pp. 7580–7585, May 2013.
- [26] J. Shaw Bagnall *et al.*, “Deformability of Tumor Cells versus Blood Cells.,” *Sci. Rep.*, vol. 5, no. November, p. 18542, 2015.

- [27] T. M. Squires, R. J. Messinger, and S. R. Manalis, "Making it stick: convection, reaction and diffusion in surface-based biosensors," *Nat. Biotechnol.*, vol. 26, no. 4, pp. 417–426, 2008.
- [28] M. G. Von Muhlen, N. D. Brault, S. M. Knudsen, S. Jiang, and S. R. Manalis, "Label-free biomarker sensing in undiluted serum with suspended microchannel resonators," *Anal. Chem.*, vol. 82, no. 5, pp. 1905–1910, 2010.
- [29] R. A. Barton, "Fabrication of a nanomechanical mass sensor containing a nanofluidic channel," *Nano Lett.*, vol. 10, pp. 2058–2063, 2010.
- [30] M. F. Khan, S. Schmid, Z. J. Davis, S. Dohn, and A. Boisen, "Fabrication of resonant micro cantilevers with integrated transparent fluidic channel," *Microelectron. Eng.*, vol. 88, no. 8, pp. 2300–2303, Aug. 2011.
- [31] S. S. Verbridge *et al.*, "Suspended glass nanochannels coupled with microstructures for single molecule detection," *J. Appl. Phys.*, vol. 97, no. 12, 2005.
- [32] P. Enoksson, G. Stemme, and E. Stemme, "Fluid density sensor based on resonance vibration," *Sensors Actuators A Phys.*, vol. 47, no. 1–3, pp. 327–331, Mar. 1995.
- [33] M. F. Khan *et al.*, "Sensors and Actuators B : Chemical Online measurement of mass density and viscosity of pL fluid samples with suspended microchannel resonator," *Sensors Actuators B. Chem.*, vol. 185, pp. 456–461, 2013.
- [34] G. Vidal-Álvarez, E. Marigó, F. Torres, and N. Barniol, "Fabrication and Measurement of a Suspended Nanochannel Microbridge Resonator Monolithically Integrated with CMOS Readout Circuitry," *Micromachines*, vol. 7, no. 3, p. 40, Mar. 2016.
- [35] C. Accoto *et al.*, "Two-Photon Polymerization Lithography and Laser Doppler Vibrometry of a SU-8-Based Suspended Microchannel Resonator," *J. Microelectromechanical Syst.*, vol. 24, no. 4, pp. 1038–1042, 2015.
- [36] J. Kim *et al.*, "Hollow Microtube Resonators via Silicon Self-Assembly toward Subattogram Mass Sensing Applications," *Nano Lett.*, vol. 16, no. 3, pp. 1537–1545, Mar. 2016.
- [37] S. M. Oskui, H. C. Bhakta, G. Diamante, H. Liu, D. Schlenk, and W. H. Grover, "Measuring the mass, volume, and density of microgram-sized objects in fluid," *PLoS One*, vol. 12, no. 4, pp. 1–17, 2017.
- [38] J. Lee *et al.*, "Suspended microchannel resonators with piezoresistive sensors," *Lab Chip*, vol. 11, no. 4, pp. 645–651, 2011.

- [39] J. Lee, A. K. Bryan, and S. R. Manalis, “High precision particle mass sensing using microchannel resonators in the second vibration mode,” *Rev. Sci. Instrum.*, vol. 82, no. 2, pp. 1–4, 2011.
- [40] S. Olcum *et al.*, “Weighing nanoparticles in solution at the attogram scale,” *Proc. Natl. Acad. Sci.*, vol. 111, no. 4, pp. 1310–1315, Jan. 2014.
- [41] S. Olcum, N. Cermak, S. C. Wasserman, and S. R. Manalis, “High-speed multiple-mode mass-sensing resolves dynamic nanoscale mass distributions,” *Nat. Commun.*, vol. 6, no. May, p. 7070, 2015.
- [42] N. Cermak *et al.*, “High-throughput measurement of single-cell growth rates using serial microfluidic mass sensor arrays,” *Nat. Biotechnol.*, vol. 34, no. 10, pp. 1052–1059, Sep. 2016.
- [43] M. H. T. Roberts, “Advanced Micropipette Techniques For Cell Physiology,” *Journal of Anatomy*, vol. 153. pp. 260–261, Aug-1987.
- [44] K. Han *et al.*, “Fabrication and Testing of Microfluidic Optomechanical Oscillators,” *J. Vis. Exp.*, no. 87, p. e51497, May 2014.
- [45] P. Wang, L. Bo, Y. Semenova, G. Farrell, and G. Brambilla, “Optical microfibre based photonic components and their applications in label-free biosensing,” *Biosensors*, vol. 5, no. 3, pp. 471–499, 2015.
- [46] J. M. Ward, N. Dhasmana, and S. Nic Chormaic, “Hollow core, whispering gallery resonator sensors,” *Eur. Phys. J. Spec. Top.*, vol. 223, no. 10, pp. 1917–1935, Sep. 2014.
- [47] M. L. Plenert and J. B. Shear, “Microsecond electrophoresis,” *Proc. Natl. Acad. Sci.*, vol. 100, no. 7, pp. 3853–3857, Apr. 2003.
- [48] J. N. Stuart and J. V Sweedler, “Ultrafast capillary electrophoresis and bioanalytical applications,” *Proc. Natl. Acad. Sci.*, vol. 100, no. 7, pp. 3545–3546, Apr. 2003.
- [49] V. Kašička, “Recent developments in capillary electrophoresis and capillary electrochromatography of peptides,” *Electrophoresis*, vol. 27, no. 1, pp. 142–175, 2006.
- [50] P. Vaiano *et al.*, “Lab on Fiber Technology for biological sensing applications,” *Laser Photonics Rev.*, vol. 10, no. 6, pp. 922–961, 2016.
- [51] J. Liu, J. Wen, Z. Zhang, H. Liu, and Y. Sun, “Voyage inside the cell: Microsystems and nanoengineering for intracellular measurement and manipulation,” *Microsystems Nanoeng.*, vol. 1, no. June, p. 15020, 2015.
- [52] A. Brüggemann, S. Stoelzle, M. George, J. C. Behrends, and N. Fertig, “Microchip Technology for Automated and Parallel Patch-Clamp Recording,” *Small*, vol. 2, no. 7, pp. 840–846, Jul. 2006.

- [53] A. Schulte and W. Schuhmann, "Single-Cell Microelectrochemistry," *Angew. Chemie Int. Ed.*, vol. 46, no. 46, pp. 8760–8777, Nov. 2007.
- [54] Z. Környei *et al.*, "Cell sorting in a Petri dish controlled by computer vision," *Sci. Rep.*, vol. 3, no. 1, p. 1088, Dec. 2013.
- [55] R. Salánki *et al.*, "Single cell adhesion assay using computer controlled micropipette," *PLoS One*, vol. 9, no. 10, p. e111450, 2014.
- [56] R. Salánki *et al.*, "Automated single cell sorting and deposition in submicroliter drops," *Appl. Phys. Lett.*, vol. 105, no. 8, p. 83703, Aug. 2014.
- [57] K. D. Piatkevich *et al.*, "A robotic multidimensional directed evolution approach applied to fluorescent voltage reporters," *Nat. Chem. Biol.*, vol. 14, no. 4, p. 352, Feb. 2018.
- [58] J. Dewynne, "ON A MATHEMATICAL MODEL FOR FIBER TAPERING," *Soc. Ind. Appl. Math.*, vol. 49, no. 4, pp. 983–990, 1989.
- [59] T. A. Birks and Y. W. Li, "The Shape of Fiber Tapers," *J. Light. Technol.*, vol. 10, no. 4, pp. 432–438, 1992.
- [60] S. Xue, M. A. Van Eijkelenborg, and G. Barton, "Theoretical Analysis on Tapering Micro-Capillary Fibres," vol. 2, no. 4, pp. 4–6, 2006.
- [61] S. Xue, G. Barton, S. Fleming, and A. Argyros, "Heat Transfer Modeling of the Capillary Fiber Drawing Process," *J. Heat Transfer*, vol. 139, no. 7, p. 72001, 2017.
- [62] S. C. Xue, M. Van Eijkelenborg, and G. W. Barton, "Role of material properties and pulling conditions in tapering micro-capillary fibres," in *Proc. 15th Int. Plastic Opt. Fibre Conf*, 2006, pp. 11–14.
- [63] S. C. Xue, M. C. J. Large, G. W. Barton, R. I. Tanner, L. Poladian, and R. Lwin, "Role of material properties and drawing conditions in the fabrication of microstructured optical fibers," *J. Light. Technol.*, vol. 24, no. 2, pp. 853–860, 2006.
- [64] A. D. Fitt, K. Furusawa, T. M. Monroe, C. P. Please, and D. J. Richardson, "The mathematical modelling of capillary drawing for holey fibre manufacture," *J. Eng. Math.*, vol. 43, no. 2–4, pp. 201–227, 2002.
- [65] R. Kosteki, H. Ebandorff-Heidepriem, S. C. Warren-Smith, and T. M. Monroe, "Predicting the drawing conditions for Microstructured Optical Fiber fabrication," *Opt. Mater. Express*, vol. 4, no. 1, p. 29, 2014.
- [66] A. D. Fitt, K. Furusawa, T. M. Monroe, and C. P. Please, "Modeling the fabrication of hollow fibers: Capillary drawing," *J. Light. Technol.*, vol. 19, no. 12, pp. 1924–1931, 2001.

- [67] A. Jain and A. Y. Yi, "Numerical modeling of viscoelastic stress relaxation during glass lens forming process," *J. Am. Ceram. Soc.*, vol. 88, no. 3, pp. 530–535, 2005.
- [68] O. S. NARAYANASWAMY, "A Model of Structural Relaxation in Glass," *J. Am. Ceram. Soc.*, vol. 54, no. 10, pp. 491–498, Oct. 1971.
- [69] S. Xue, M. A. van Eijkelenborg, G. W. Barton, and P. Hambley, "Theoretical, numerical, and experimental analysis of optical fiber tapering," *J. Light. Technol.*, vol. 25, no. 5, pp. 1169–1176, 2007.
- [70] C. E. Chryssou, "Theoretical analysis of tapering fused silica optical fibers using a carbon dioxide laser," *Opt. Eng.*, vol. 38, no. 10, p. 1645, 1999.
- [71] A. J. C. Grellier, N. K. Zayer, and C. N. Pannell, "Heat transfer modelling in CO<sub>2</sub> laser processing of optical fibres," *Opt. Commun.*, vol. 152, no. 4–6, pp. 324–328, Jul. 1998.
- [72] Y. C. Maya, N. G. Cardona, and P. I. Torres Trujillo, "Low cost heat-and-pull rig for manufacturing adiabatic optical fiber tapers," *Rev. Fac. Ing.*, no. 70, pp. 167–172, 2014.
- [73] T. A. Birks, G. Kakarantzas, and P. S. Russell, "All-fibre devices based on tapered fibres," in *Optical Fiber Communication Conference, 2004. OFC 2004*, 2004, vol. 2, p. 3 pp. vol.2-pp.
- [74] T. E. Dimmick, G. Kakarantzas, T. a Birks, and P. S. Russell, "Carbon dioxide laser fabrication of fused-fiber couplers and tapers.," *Appl. Opt.*, vol. 38, no. 33, pp. 6845–6848, 1999.
- [75] J. M. Ward, A. Maimaiti, V. H. Le, and S. N. Chormaic, "Contributed review: Optical micro- and nanofiber pulling rig," *Rev. Sci. Instrum.*, vol. 85, no. 11, 2014.
- [76] L. J. Steinbock, J. F. Steinbock, and A. Radenovic, "Controllable shrinking and shaping of glass nanocapillaries under electron irradiation," *Nano Lett.*, vol. 13, no. 4, pp. 1717–1723, 2013.
- [77] F. Bayle and J.-P. Meunier, "Efficient fabrication of fused-fiber biconical taper structures by a scanned CO<sub>2</sub> laser beam technique," *Appl. Opt.*, vol. 44, no. 30, p. 6402, Oct. 2005.
- [78] J.-M. Friedt and É. Carry, "Introduction to the quartz tuning fork," *Am. J. Phys.*, vol. 75, no. 5, pp. 415–422, 2007.
- [79] H. Edwards, L. Taylor, W. Duncan, and A. J. Melmed, "Fast, high-resolution atomic force microscopy using a quartz tuning fork as actuator and sensor," *J Appl Phys*, vol. 82, no. 3, pp. 980–984, 1997.
- [80] J. Falter *et al.*, "Calibration of quartz tuning fork spring constants for non-contact atomic force microscopy: Direct mechanical

- measurements and simulations,” *Beilstein J. Nanotechnol.*, vol. 5, no. 1, pp. 507–516, 2014.
- [81] A. Castellanos-Gomez, N. Agrat, and G. Rubio-Bollinger, “Dynamics of quartz tuning fork force sensors used in scanning probe microscopy,” *Nanotechnology*, vol. 20, no. 21, pp. 1–16, 2009.
- [82] P. Sandoz, J. M. Friedt, and É. Carry, “Vibration amplitude of a tip-loaded quartz tuning fork during shear force microscopy scanning,” *Rev. Sci. Instrum.*, vol. 79, no. 8, 2008.
- [83] D. V. Serebryakov, A. P. Cherkun, B. A. Loginov, and V. S. Letokhov, “Tuning-fork-based fast highly sensitive surface-contact sensor for atomic force microscopy/near-field scanning optical microscopy,” *Rev. Sci. Instrum.*, vol. 73, no. 4, p. 1795, 2002.
- [84] M. Yun, E. Lee, K. Cho, and S. Jeon, “Enhanced sensitivity of a microfabricated resonator using a graphene-polystyrene bilayer membrane,” *Appl. Phys. Lett.*, vol. 105, no. 7, 2014.
- [85] D. O. Clubb, O. V. L. Buu, R. M. Bowley, R. Nyman, and J. R. Owers-Bradley, “Quartz tuning fork viscometers for helium liquids,” *J. Low Temp. Phys.*, vol. 136, no. 1–2, pp. 1–13, 2004.
- [86] P. Patimisco, G. Scamarcio, F. K. Tittel, and V. Spagnolo, “Quartz-enhanced photoacoustic spectroscopy: A review,” *Sensors (Switzerland)*, vol. 14, no. 4, pp. 6165–6206, 2014.
- [87] A. M. C. Valkering, A. I. Mares, C. Untiedt, K. B. Gavan, T. H. Oosterkamp, and J. M. Van Ruitenbeek, “A force sensor for atomic point contacts,” *Rev. Sci. Instrum.*, vol. 76, no. 10, pp. 1–5, 2005.
- [88] S. An *et al.*, “Nanopipette combined with quartz tuning fork-atomic force microscope for force spectroscopy/microscopy and liquid delivery-based nanofabrication,” *Rev. Sci. Instrum.*, vol. 85, no. 3, 2014.
- [89] H. S. Liao *et al.*, “High-speed atomic force microscope based on an astigmatic detection system,” *Rev. Sci. Instrum.*, vol. 85, no. 10, 2014.
- [90] H.-S. Liao *et al.*, “Operation of astigmatic-detection atomic force microscopy in liquid environments,” *Rev. Sci. Instrum.*, vol. 84, no. 10, p. 103709, Oct. 2013.
- [91] K. C. Fan, C. Y. Lin, and L. H. Shyu, “The development of a low-cost focusing probe for profile measurement,” *Meas. Sci. Technol.*, vol. 11, no. 1, pp. N1–N7, Jan. 2000.
- [92] H.-S. Liao, B.-J. Juang, K.-Y. Huang, E.-T. Hwu, and C.-S. Chang, “Spring Constant Calibration of Microcantilever by Astigmatic Detection System,” *Jpn. J. Appl. Phys.*, vol. 51, no. 8S3, p. 08KB13, Aug. 2012.

- [93] W.-M. Wang, K.-Y. Huang, H.-F. Huang, I.-S. Hwang, and E.-T. Hwu, "Low-voltage and high-performance buzzer-scanner based streamlined atomic force microscope system," *Nanotechnology*, vol. 24, no. 45, p. 455503, Nov. 2013.
- [94] A. C. Ceccacci *et al.*, "Blu-Ray-based micromechanical characterization platform for biopolymer degradation assessment," *Sensors Actuators, B Chem.*, vol. 241, pp. 1303–1309, 2016.
- [95] C. Riesch, A. Jachimowicz, F. Keplinger, E. K. Reichel, and B. Jakoby, "A Novel Sensor System for Liquid Properties Based on a Micromachined Beam and a Low-Cost Optical Readout," in *2007 IEEE Sensors*, 2007, pp. 872–875.
- [96] N. Scuor, P. Gallina, O. Sbaizero, H. V Panchawagh, and R. L. Mahajan, "Dynamic characterization of MEMS cantilevers in liquid environment using a low-cost optical system," *Meas. Sci. Technol.*, vol. 17, no. 1, pp. 173–180, Jan. 2006.
- [97] S. Kostner and M. J. Vellekoop, "DVD pickup heads for optical measurement applications," *e i Elektrotechnik und Informationstechnik*, vol. 125, no. 3, pp. 98–101, Mar. 2008.
- [98] E. Gil-Santos *et al.*, "Nanomechanical mass sensing and stiffness spectrometry based on two-dimensional vibrations of resonant nanowires.," *Nat. Nanotechnol.*, vol. 5, no. 9, pp. 641–645, 2010.
- [99] S. Schmid, L. G. Villanueva, and M. L. Roukes, *Fundamentals of nanomechanical resonators*, no. EPFL-BOOK-220923. Springer, 2016.
- [100] A. N. Cleland, *Foundations of nanomechanics: from solid-state theory to device applications*. Springer Science & Business Media, 2013.
- [101] K. L. Ekinici and M. L. Roukes, "Nanoelectromechanical systems," *Rev. Sci. Instrum.*, vol. 76, no. 6, p. 61101, Jun. 2005.
- [102] K. Yum, Z. Wang, A. P. Suryavanshi, and M.-F. Yu, "Experimental measurement and model analysis of damping effect in nanoscale mechanical beam resonators in air," *J. Appl. Phys.*, vol. 96, no. 7, pp. 3933–3938, Oct. 2004.
- [103] Wenjing Ye, Xin Wang, W. Hemmert, D. Freeman, and J. White, "Air damping in laterally oscillating microresonators: A numerical and experimental study," *J. Microelectromechanical Syst.*, vol. 12, no. 5, pp. 557–566, Oct. 2003.
- [104] O. Malvar, D. Ramos, C. Martínez, P. Kosaka, J. Tamayo, and M. Calleja, "Highly Sensitive Measurement of Liquid Density in Air Using Suspended Microcapillary Resonators," *Sensors*, vol. 15, no. 4, pp. 7650–7657, Mar. 2015.

- [105] A. Arnau Vives, “Piezoelectric transducers and applications Sec. Edition,” Springer Berlin Heidelberg, 2008, p. 79.
- [106] G. Tagata, “Harmonically forced, finite amplitude vibration of a string,” *J. Sound Vib.*, vol. 51, no. 4, pp. 483–492, Apr. 1977.
- [107] “Corning Pyrex® 7740 Borosilicate Glass.” [Online]. Available: <http://matweb.com/search/DataSheet.aspx?MatGUID=5bb651ca58524e79a503011b2cd8083d>. [Accessed: 22-Apr-2018].
- [108] C. F. Bohren and D. R. Huffman, *Absorption and scattering by a sphere*. Wiley Online Library, 1983.
- [109] A. D. McLachlan and F. P. Meyer, “Temperature dependence of the extinction coefficient of fused silica for CO<sub>2</sub> laser wavelengths,” *Appl. Opt.*, vol. 26, no. 9, p. 1728, May 1987.
- [110] L. Gunther, *The physics of music and color*. Springer Science & Business Media, 2011.
- [111] I. Lee, K. Park, and J. Lee, “Precision density and volume contraction measurements of ethanol–water binary mixtures using suspended microchannel resonators,” *Sens. Actuators, A*, vol. 194, pp. 62–66, 2013.
- [112] P. Enoksson, G. Stemme, and E. Stemme, “Silicon tube structures for a fluid-density sensor,” *Sens. Actuators, A*, vol. 54, pp. 558–562, 1996.
- [113] M. Najmzadeh, S. Haasl, and P. Enoksson, “A silicon straight tube fluid density sensor,” *J. Micromech. Microeng.*, vol. 17, pp. 1657–1663, 2007.
- [114] T. Corman, “A low-pressure encapsulated resonant fluid density sensor with feedback control electronics,” *Meas. Sci. Technol.*, vol. 11, pp. 205–211, 2000.

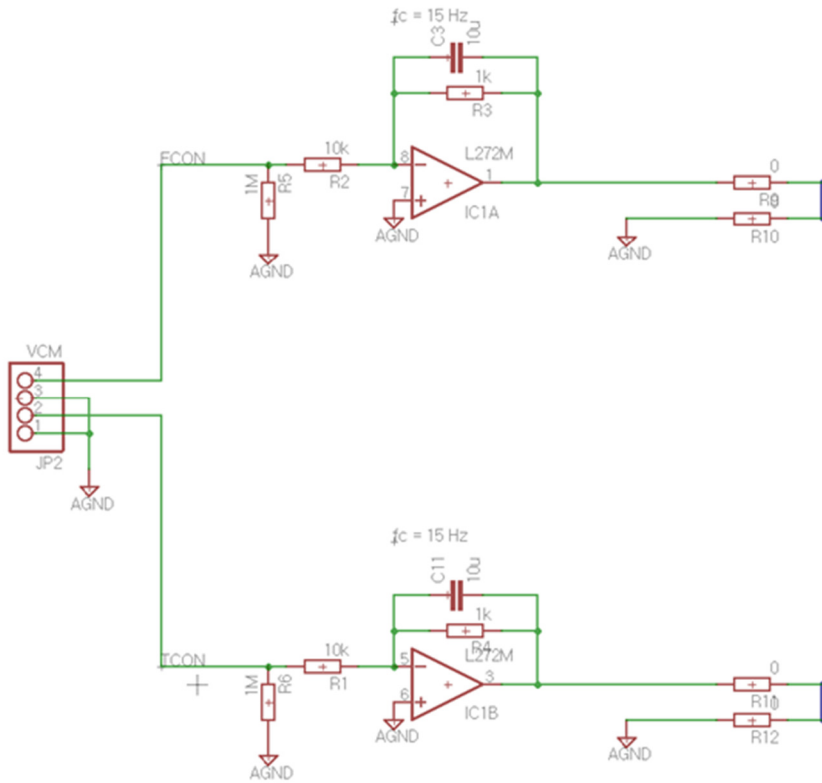
# APPENDIX

## **A.1. Automatic power control and voice coil actuator**

A power regulator for supplying current to laser diode in OPU is implemented. A short duration of current spike can damage to the laser diode, a constant current source with feedback circuit should be required to stable and operating OPU for a long time. Automatic power controller for laser diode is designed by PNP transistor and op-amp to configure the current feedback circuit (See Appendix figure 1).

To control the voice coil actuators built in OPU, L272M op-amp is used (Appendix figure 2). L272M op-amp has two current amplifiers, each amplifier drives a focusing and tracking voice coil actuator independently. Control signal range from -10 to 10 V generated from data acquisition board (USB-6363, National Instruments) is loaded to voice coil controller.

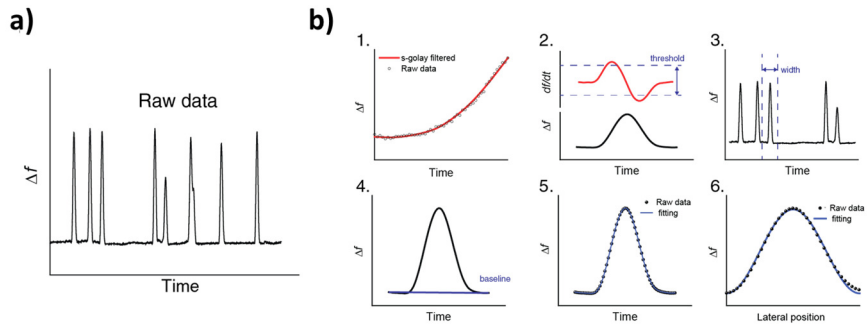




**Appendix figure 2. Voice coil controller circuit.**

## **A.2. Particle frequency peak finding and fitting**

Frequency change data due to traveling particles recorded in time were processed to extract mass of particles as illustrated in Appendix figure 3. First, recorded rawdata were Savitzky-Golay filtered (window of 50 and polynomial order of 3). Then, first time derivatives of the frequency change were compared with a pre-configured threshold to locate each peak resulting from a particle. For each selected peak, a small window was masked to get a baseline to be



**Appendix figure 3. Data fitting processing for particles to extract buoyant mass. (a) Frequency change vs. time raw data. (b) Step-by-step data processing procedure.**

compensated. Filtered and baseline compensated frequency change data were fitted by frequency-mass shift equation (3.3) to obtain buoyant mass of particle.

## 요약

마이크로 구조물을 갖는 기계적 공진 센서 플랫폼은 미세입자의 질량 및 검출에 널리 사용되어 왔다. 이 센서는 센서의 구조적 형상에 의거한 공진주파수 발생을 이용해 입자가 구조물에 로딩되었을 때 변화된 센서의 질량을 공진주파수 쉬프트 방법으로 검출할 수 있다. 이와 같은 주파수-쉬프트 방식의 센서 구동 플랫폼은 발달된 전자공학 기술로 인해 실시간 계측이 가능하여 빠르게 변화하는 미세환경 하에서도 정확한 입자의 질량을 확인할 수 있다는 장점이 있다.

이 센서 플랫폼에 속하는 마이크로튜브 레조네이터는 특히 유체에 부유하는 살아있는 세포나 마이크로 입자들의 질량을 실시간으로 계측할 수 있다는 점에서 특특한 센서 플랫폼으로 주목되었다. 마이크로튜브 레조네이터는 구조물 내부에 내장된 유체 채널을 이용해 계측 입자를 센서 내부로 자유롭게 이송할 수 있게 하고 유체 및 입자를 센서 본체 내부에 위치시킴으로써 센서가 공진을 일으킬 때 유체와 구조물 간의 댐핑 효과를 줄여 높은 공진 품질을 유지할 수 있다는 장점을 가지고 있다.

이러한 특성을 바탕으로, 그동안 마이크로튜브 레조네이터는 다양한 유체기반 질량계측 연구를 수행해 왔다. 그러나, 반도체 미세공정을 기반으로 제작되는 이 센서는 고가의 비용과 복잡한 개발 공정으로 인해 낮은 수율을 수반하고 숙련된 오퍼레이터의 필요, 그리고 개발이

느리다는 문제점 때문에 뛰어난 성능에도 불구하고 다양한 연구분야에 널리 활용되기 어려웠다.

본 연구에서는, 기존의 미세공정 과정을 대체할 수 있는 유리모세관 인장 가공 방식을 새롭게 도입하였다. 1-mm 직경을 갖는 유리 모세관을 레이저 풀링 기법을 이용하여 3 초 이내에 임의의 마이크로 수준 (10-200  $\mu\text{m}$ )의 직경을 갖는 마이크로튜브로 가공할 수 있고, 이를 이용해 제작된 마이크로튜브 레조네이터는 기존 반도체 공정으로 제조된 디바이스의 질량 민감도에 상응하는 수준을 보여주었다. 본 연구에서 제시하는 새로운 제조법은 마이크로튜브의 크기를 자유롭게 설정할 수 있어 다양한 크기의 입자 계측 연구에 빠르게 활용될 수 있는 장점이 있다.

본 연구에서는 유리모세관으로 제작된 마이크로튜브 레조네이터의 특성을 분석하였다. 단면이 타원 형상을 가질 때 발생하는 모드 스플릿 현상에 대해 이론 및 실험을 통해 검증하였고, 센서를 파이펫 형태의 플랫폼으로 구현하여 사용성이 높도록 개선하였다. 또한 제작된 센서 플랫폼을 이용해 원생생물 및 다양한 미세입자 질량 계측을 시연하였다.

본 연구에서 제안한 유리모세관 마이크로튜브 레조네이터 플랫폼은 바이오, 미세입자 및 미세유체 등의 다양한 연구분야 활용될 수 있을 것으로 기대된다.

**주요어 : 레조네이터, 마이크로 캐필러리, 마이크로 입자, 질량 센서**

**학 번 : 2012-30925**